

Search for the Flavor Changing Neutral Current Decay

$t \rightarrow Zq$ at $\sqrt{s} = 1.96$ TeV

by

Jennifer Lindsay Gimmell

Submitted in Partial Fulfillment

of the

Requirements for the Degree

Doctor of Philosophy

Supervised by

Professor Paul Tipton

and

Professor Kevin McFarland

Department of Physics and Astronomy

The College

Arts and Sciences

University of Rochester

Rochester, New York

2009

“What are we going to play today, Gram?”

I dedicate this thesis to the most intelligent and beautiful woman I know: my grandmother, Eleanor Simek. Throughout the years, she has taught me how to find humor in life and how to be strong when the going gets tough, and all you want to do is give up. Above all, she taught me to believe in myself—a trait that I will possess for the rest of my life.

Without you, I would not be the person that I am today.

I love you, Gramma. I dedicate this thesis to you.

All the love in the World,

Dolly xoxo

Curriculum Vitae

The author attended Hiram College in the fall of 1999. After spending the summer of 2001 with the Materials Research Science and Engineering Center at the James Frank Institute at the University of Chicago with Professor Steven Sibener, and the summer of 2002 at the Princeton Plasma Physics Laboratory enrolled in the Department of Energy's sponsored Energy Research for Undergraduates Laboratory Fellowship (ERULF) under the guidance of Dr. Andrew Post-Zwicker, she graduated with bachelors degrees in mathematics and physics in the spring of 2003. She came to the University of Rochester in the fall of 2003 to begin graduate study in physics. Entering graduate school on a teaching fellowship, she was honored for her excellence in teaching with the physics department's Graduate Teaching Award in the fall of 2004 along with certification in teaching college level physics. The following year in the fall of 2005 she was awarded the American Association of Physics Teachers Prize for her excellence as a teaching assistant. After passing her qualifying examinations in the winter of 2005, she received her Master's of Arts degree from the University of Rochester. The author moved to Fermi National Accelerator Laboratory in June of 2005 to begin research in experimental high energy particle physics under the guidance of Professors Paul Tipton and Kevin McFarland.

Acknowledgments

There are many people throughout the past years of my graduate education who have helped shape me into the physicist that I have become.

Professionally, I would like to extend great thanks to my adviser, Professor Paul Tipton, for his guidance, graciousness and sense of humor throughout the past few years. He gave me a tremendous opportunity as his graduate student, and none of this work is possible without him. I also thank Professor Kevin McFarland for his assistance with my graduate career. I also extend my great thanks and am indebted to “my dear post-doc” Ulrich Husemann for his help, C++ mastery, patience, and friendly conversations over coffee. Ulrich contributed a lot to my work, and without him my code would have never compiled in a timely fashion, and I would never have learned about the magic that is Keynote. I also thank Charles Plager for his wonderful plotting scripts and his statistics mastery that made this thesis possible.

I would like to thank the University of Rochester, especially Barbara Warren and the staff in the high energy physics group. Their support throughout the years has been invaluable. I am thankful for my professors in my graduate courses, and to Professor Hagen for believing in my abilities as a student. I thank him greatly for his witty lectures and his assistance with my studies for my preliminary examination.

I am very grateful to the CDF Collaboration and to everyone who has helped to make this fantastic experiment run smoothly. Special thanks to the top physics working group at CDF, for welcoming me with open arms, asking me challenging questions, and enjoying my cookies during my analysis blessing. I thank the godparent committee for my analysis, Jason Nielsen, Ben Kilminster, and Koji Sato, for their helpful comments and suggestions to aid in the publication of this analysis.

Personally, I have many people to thank for standing by me as I completed this work. I give special thanks to my oldest and dearest friend Claire Goodfriend, who has stuck with me through thick and thin. To Dipendra and Emily Shrestha for warm holiday visits and encouragement to “...hurry up, get done, and move back to us!” Thanks to my little sister Christie Stemplinski for giving me opportunities to escape reality with our crazy parties at home and allowing me to visit and enjoy the sun in Southern California. My dear friends at Rochester, Julie Langenbrunner (my Pookie!) and Jesse Chvojka: you both made each day easier and full of humor and episodes Family Guy. A big part of my happiness at Rochester is contributed to you two. Many thanks to my dear Su-Jung Park, whose retail therapy and pancakes always made everything better and to Meghan Anzelc and Kendall Mahn, whose Starbucks retreats and Sweet Tomatoes lunches made life sweet. I also extend incredible thanks to the second smartest blonde I know, April Cook: “A, we are one in the same, and I don’t know how I got along without you. You’re the best! xoxo, Lil’ J”. I also thank all of the many friends and acquaintances that I’ve made along the way in graduate school and in Illinois, especailly Nick and Christina Melville and all of the members of “The Quabob”.

Many thanks to my very good friend, now more, Daniel McCarron. You have shown me so many wonderful things in life, including our Friday night Lou Malnati’s pizza dates, and introducing me to my love of powerlifting and picking up

heavy stuff. I hope that we can always share that and our lives together, and that I can be there for you as you finish your Ph.D. as you were there with your support for me.

Above all, I would like to thank the most important people in my life for their constant love and support: my family, especially my parents and my grandmother. Thank you for supporting me in my trials and tribulations in my education and for believing in me each and every step of the way.

Abstract

This thesis reports the results of a search for the flavor changing neutral current decay of the top quark, $t \rightarrow Zq$, in decays of $t\bar{t}$ pairs produced in $p\bar{p}$ collisions at a center-of-mass energy of 1.96 TeV. This search is performed on a data sample recorded by the Collider Detector at Fermilab (CDF), corresponding to an integrated luminosity of 1.9 fb^{-1} .

This search follows a previous CDF analysis that resulted in an upper limit for the branching fraction $\mathcal{B}(t \rightarrow Zq)$ of 10.4% at 95% C.L. using a dataset equivalent to 1.1 fb^{-1} of integrated luminosity. This thesis extends to 1.9 fb^{-1} of data, and has improved sensitivity to the small signal with the introduction of a template fit technique that includes systematic uncertainties by a linear interpolation between templates. Using a Feldman-Cousins construction, an upper limit at 95% C.L. is set on $\mathcal{B}(t \rightarrow Zq)$ of 3.7%, with the expected upper limit in absence of a signal is $5.0 \pm 2.2\%$ for a top mass of $175 \text{ GeV}/c^2$.

Contents

Curriculum Vitae	ii
Acknowledgments	iii
Abstract	vi
1 Introduction	1
2 Relevant Theory	3
2.1 The Standard Model of Particle Physics	3
2.1.1 Weak Interactions in the Standard Model	5
2.2 Flavor Changing Neutral Currents in the Standard Model	7
2.3 Experimental Limits to Date	8
2.3.1 Previous Search from CDF Run-I	8
2.3.2 Previous Search from LEP	9
2.3.3 Previous Search from CDF Run-II	9
3 The Experiment	12
3.1 Fermi National Accelerator Laboratory	12
3.2 The Collider Detector at Fermilab	16
3.2.1 The Detector Apparatus	17

3.2.2	Data Acquisition	27
3.2.3	Triggers Used for This Thesis	29
4	Object Identification and Event Reconstruction	31
4.1	Object Identification	32
4.1.1	Electron Identification	32
4.1.2	Muon Identification	35
4.1.3	Track Lepton Identification	36
4.1.4	Jet Reconstruction	37
4.2	Event Reconstruction	37
4.3	The Mass χ^2 Discriminant	38
4.4	Optimization of Analysis Variables	39
4.5	Signal and Control Regions	41
4.6	Data Sample	41
5	Acceptance for the Top FCNC Decay	44
5.1	Signal Monte Carlo Simulation	45
5.2	Scaling of the Monte Carlo Simulations	46
5.2.1	Scaling for Luminosity	46
5.2.2	Scaling for Trigger and Reconstruction Efficiencies	47
5.2.3	Scaling for b -quark Jet Efficiencies	47
5.2.4	Scaling for the Redefined $t \rightarrow Wd$ Vertex	50
5.3	Normalization to a Reinterpreted Top Pair Production Cross Section	50
5.4	Acceptance Definition and Calculation	52
5.4.1	Acceptance Definition	52
5.4.2	Acceptance Calculation	54
5.5	Monte Carlo Simulation of Background Processes	56

5.5.1	Comparison of Data to Monte Carlo Simulation	58
6	Determination of Sources of Systematic Uncertainty	62
6.1	Signal Rate Systematic Uncertainties	62
6.2	Background Rate Systematic Uncertainties	68
6.3	Systematic Rate Uncertainties Due to Normalization	69
6.4	Mass χ^2 Shape Systematic Uncertainties	71
6.4.1	Associated with Jet Energy Scale	72
6.4.2	Associated with ALPGEN Parameters	75
7	Calculation of an Upper Limit on $\mathcal{B}(t \rightarrow Zq)$	76
7.1	The Maximum Likelihood Fitter	76
7.1.1	Templates Used in the Likelihood Fitter	77
7.1.2	Using the Control Region to Constrain the Signal Regions	78
7.2	The Feldman-Cousins Limit Calculation	79
7.2.1	Pseudo-Experiments Used in the Limit Calculation	81
7.2.2	Template Morphing	82
7.2.3	The Feldman-Cousins Construction	83
7.2.4	The Expected Limit Calculation	86
8	Result and Conclusions	88
8.1	Result: An Upper Limit on $\mathcal{B}(t \rightarrow Zq)$	88
8.2	Implications for Future Work	91
	Bibliography	93
A	Control Plots	96
A.1	Jet Multiplicity	97
A.2	Kinematic Distributions	100

A.2.1	The Mass χ^2 Distribution	100
A.2.2	The Transverse Mass Distribution	101
A.2.3	The Leading Jet E_T Distribution	102
A.2.4	The Second Jet E_T distribution	103
A.2.5	The Third Jet E_T Distribution	104
A.2.6	The Fourth Jet E_T Distribution	105
A.2.7	The Z Mass Distribution	106
A.2.8	The G_T Distribution	107
A.2.9	The Missing Transverse Energy Distribution	108
A.3	Kinematic Distributions, JES shift -1σ	109
A.3.1	The Mass χ^2 Distribution, JES shift -1σ	109
A.3.2	The Transverse Mass Distribution, JES shift -1σ	110
A.3.3	The Leading Jet E_T Distribution, JES shift -1σ	111
A.3.4	The Second Jet E_T Distribution, JES shift -1σ	112
A.3.5	The Third Jet E_T Distribution, JES shift -1σ	113
A.3.6	The Fourth Jet E_T Distribution, JES shift -1σ	114
A.3.7	The G_T Distribution, JES shift -1σ	115
A.3.8	The Missing Transverse Energy Distribution, JES shift -1σ	116
A.3.9	The Z Mass Distribution, JES shift -1σ	117
A.4	Kinematic Distributions, JES shift $+1\sigma$	118
A.4.1	The Mass χ^2 Distribution, JES shift $+1\sigma$	118
A.4.2	The Transverse Mass Distribution, JES shift $+1\sigma$	119
A.4.3	The Leading Jet E_T Distribution, JES shift $+1\sigma$	120
A.4.4	The Second Jet E_T Distribution, JES shift $+1\sigma$	121
A.4.5	The Third Jet E_T Distribution, JES shift $+1\sigma$	122
A.4.6	The Fourth Jet E_T Distribution, JES shift $+1\sigma$	123
A.4.7	The G_T Distribution, JES shift $+1\sigma$	124

A.4.8	The Missing Transverse Energy Distribution, JES shift $+1\sigma$	125
A.4.9	The Z Mass Distribution, JES shift $+1\sigma$	126
B	Effects of Luminosity Scaling	127
B.1	Overlaid Interactions and Instantaneous Luminosity	127
B.2	Luminosity Study: Kinematic Variables	129
B.2.1	Z Mass	129
B.2.2	The Z s Leptons	130
B.2.3	The Leading Jet E_T	132
B.2.4	The Second Jet E_T	133
B.2.5	Transverse Mass, m_T	134
B.2.6	Scalar Energy Sum, G_T	135

List of Tables

2.1	The Quarks and Leptons	4
4.1	Optimized Event Selection Criteria	40
4.2	Datasets and Corresponding Luminosities.	42
4.3	Triggers Paths and Corresponding Data Run Ranges	43
5.1	Signal Monte Carlo Simulation Samples	45
5.2	Scale Factors and Trigger Efficiencies	48
5.3	The “Lepton + Jets” Selection Criteria	51
5.4	Background Contributions of the “Lepton+Jets” Selection	52
5.5	Monte Carlo Simulation: Z+jets	60
5.6	Monte Carlo Simulation: Smaller Background Contributions	61
6.1	Rate Systematic Uncertainties Associated with Helicity Corrections.	65
6.2	Rate Systematic Uncertainties Associated with ISR and FSR	67
6.3	Summary of Rate Systematic Uncertainties for the Signal	69
6.4	Summary of Rate Systematic Uncertainties for the Background	70
6.5	Summary of Shape Systematic Uncertainties	73
8.1	Parameters of Best Fit to Data	89

List of Figures

2.1	Feynman Diagrams for Top FCNCs	7
2.2	The Mass χ^2 Distribution Using 1.12 fb ⁻¹ of Data.	10
3.1	The Fermilab Accelerator Complex	13
3.2	Aerial View: Fermilab Tevatron and the Accelerator Complex.	16
3.3	The CDF detector: Longitudinal View	17
3.4	The CDF Tracking System	20
3.5	The CDF Silicon Detector	21
3.6	CDF Silicon Detector: Layer-00	22
6.1	Mass χ^2 Distributions for Variations in the Jet Energy Scale.	74
7.1	Templates for the FCNC Signal	79
7.2	Dependence of $\mathcal{R}_{\text{sig}}(\sigma_{\text{JES}})$ on the Shift in JES.	80
7.3	Compound Horizontal Template Morphing	83
7.4	An Example of the Feldman-Cousins Construction.	85
7.5	Feldman-Cousins Bands and the Expected Limit Distribution	87
8.1	The Mass χ^2 Distribution for 1.9 fb ⁻¹ of Data	90
8.2	Sensitivity of the ATLAS Experiment to Top FCNCs	92
A.1	N-jet distribution for events containing a Z	97

A.2	N-jet distribution for pre- b -tagged events containing a Z	98
A.3	N-jet distribution for $Z \rightarrow \mu^+ \mu^-$ events	99
A.4	Kinematic distribution for $\sqrt{\chi^2}$	100
A.5	Kinematic distribution for the transverse mass, m_T	101
A.6	Leading jet E_T distribution	102
A.7	Second jet E_T distribution	103
A.8	Third jet E_T distribution	104
A.9	Fourth jet E_T distribution	105
A.10	Z mass distribution	106
A.11	G_T distribution	107
A.12	Missing E_T distribution	108
A.13	The mass χ^2 distribution, JES shift -1σ	109
A.14	The transverse mass distribution, JES shift -1σ	110
A.15	The leading jet E_T distribution, JES shift -1σ	111
A.16	The second jet E_T distribution, JES shift -1σ	112
A.17	The third jet E_T distribution, JES shift -1σ	113
A.18	The fourth jet E_T distribution, JES shift -1σ	114
A.19	The G_T distribution, JES shift -1σ	115
A.20	The missing E_T distribution, JES shift -1σ	116
A.21	The Z mass distribution, JES shift -1σ	117
A.22	The mass χ^2 distribution, JES shift $+1\sigma$	118
A.23	The transverse mass distribution, JES shift $+1\sigma$	119
A.24	The leading jet E_T distribution, JES shift $+1\sigma$	120
A.25	The second jet E_T distribution, JES shift $+1\sigma$	121
A.26	The third jet E_T distribution, JES shift $+1\sigma$	122
A.27	The fourth jet E_T distribution, JES shift $+1\sigma$	123
A.28	The G_T distribution, JES shift $+1\sigma$	124

A.29	The missing E_T distribution, JES shift $+1\sigma$	125
A.30	The Z mass distribution, JES shift $+1\sigma$	126
B.1	Luminosity dependence study: Z mass.	129
B.2	Luminosity dependence study: Z lepton with higher p_T	130
B.3	Luminosity dependence study: Z lepton with lesser p_T	131
B.4	Luminosity dependence study: Leading Jet E_T	132
B.5	Luminosity dependence study: Second Jet E_T	133
B.6	Luminosity dependence study: Transverse Mass, m_T	134
B.7	Luminosity dependence study: Scalar Energy Sum, G_T	135

Chapter 1

Introduction

“What is the universe made of?” The ambition of the field of particle physics is the determination of the fundamental constituents of the universe and the nature of their interactions. In the last half of the 20th Century, the field as a whole has made incredible progress in uncovering these constituent particles and understanding the forces that govern their interactions. Through this progress, the standard model (SM) of particle physics was developed to attempt to categorize the fundamental particles and explain their properties.

Nearly all particles predicted by the standard model have been directly observed, with only the elusive Higgs boson awaiting detection. Despite the great success of the theory in describing the particles observed until now, there is good theoretical motivation to believe that additional features become evident at the TeV energy scale, including additional particles and interactions not yet observed. Probing physics at these energy levels is the project of modern experimental particle physics, including developing a good understanding of the top quark and its properties.

This thesis focuses its attention on a rare decay of the top quark, its flavor

changing neutral current (FCNC) decay. This decay is highly suppressed in the standard model and to this date, has not been experimentally detected. Detecting top FCNCs open the possibility to testing new physics models which predict a higher probability for this decay in nature. Thus, any signal of this decay would be an indication of new physics.

This thesis is organized as follows: Chapter 2 introduces the standard model giving some of the relevant theory for the flavor changing neutral current of the top quark, and why this decay is so suppressed in the standard model. Chapter 2 also gives an overview of the current experimental limits on top flavor changing neutral currents to date. Chapter 3 describes the Fermilab accelerator complex and the detector which are used for this thesis. Chapter 4 gives an overview of the detection of electrons and muons and gives the selection of tops flavor changing neutral current decay. Chapter 4 also describes how this selection is optimized to distinguish the signal from the background. Chapter 5 details the calculation of the acceptance for the analysis and how Monte Carlo simulations are used for predicting the background rates. Chapter 6 gives the systematic uncertainty analysis. Chapter 7 presents the details of the Feldman-Cousins limit calculation and the expected limit for the branching fraction in the absence of a signal. Chapter 8 summarizes the results of this thesis, presenting the world's best limit for the branching fraction, $\mathcal{B}(t \rightarrow Zq)$, with 95% confidence.

Chapter 2

Relevant Theory

This chapter serves as an introduction to the standard model. It outlines the flavor changing neutral current (FCNC) decay of the top quark, showing how it is suppressed in the standard model. Several other experiments have studied this decay, both in e^+e^- interactions and in earlier operations of this experiment. These experiments are discussed in this chapter, with focus given to a recent study using 1.1 fb^{-1} of data at the Collider Detector at Fermilab.

2.1 The Standard Model of Particle Physics

In the standard model (SM), the groups of fundamental particles are the gauge bosons, quarks, and leptons. An important tenant of the SM is that the exchange of gauge bosons mediates the interactions between the fundamental particles.

The fundamental particles are the six quarks and the six leptons, both arranged into three generations. Each generation is a “carbon copy” of the previous, differing only in mass. For each particle, although not shown in Table 2.1, there is an anti-particle with the opposite charge.

Table 2.1: The fundamental particles of the standard model, the quarks and leptons, displayed in generations.

	Generations		
	I	II	III
Quarks	u	c	t
	d	s	b
Leptons	ν_e	ν_μ	ν_τ
	e	μ	τ

There are four forces which categorize the interactions of the particles. These forces, listed in order of strength, are the strong, electromagnetic, weak, and gravitational force. Both quarks and leptons are spin-1/2 particles that can interact via gravity, the electromagnetic force and the weak force. One important difference between quarks and leptons is that quarks can also interact via the strong force.

Gluons are the mediators for the strong force. The strong force increases in strength as the distance between two quarks is increased. Quarks confined inside of a proton are basically free particles. At sub-atomic length scales, it is the strong force that confines quarks inside protons and neutrons. Electromagnetic interactions are mediated by photons, and the weak force interacts with particles through the exchange of the charged W and neutral Z bosons. In electromagnetic interactions, the photon couples to electric charge with interaction strength proportional to that charge. All of the SM fundamental fermions interact with the weak force by charge-changing interactions through the exchange of a W boson or neutral interactions by the exchange of a Z boson. Weak interactions are complicated by the fact that the bosons couple to weak isospin. Since the W bosons are charged, they also couple to photons. This leads to the idea that the electromagnetic and the weak forces are two aspects of the same entity, the electroweak force. Although we are most familiar with the gravitational force, it is, however, the weakest and

least understood. Its effects only become dominant at large distance scales and with objects of very large mass. The gravitational effects on elementary particles are mostly negligible.

2.1.1 Weak Interactions in the Standard Model

One important aspect of the standard model, and one which is the focus of this thesis, is the theory involving the interactions with the W^\pm and Z bosons, the charged and neutral weak interactions, respectively.

The theory governing the weak interaction is based on a combined symmetry group $SU(2)_L \times U(1)$ of weak isospin and the hypercharge, such that the generator of the group $SU(2)_L$ is given by the isospin version of the Pauli matrices $I_i \equiv \frac{1}{2}\tau_i$, and the generator of the group $U(1)$ is the weak hypercharge. The subscript “L” denotes that the weak interaction is only for left-handed fermion states.

The charged current interactions involve the coupling of the W^\pm boson to leptons in a particular generation. In charged current interactions, there is no cross-coupling between lepton generations. These couplings violate conservation laws of lepton number. Charged current interactions between the quarks do involve coupling among different generations, giving rise to interactions between generations of quarks that involve the changing and conservation of additional properties. For example, the strangeness changing process $s \rightarrow W^- + u$ should occur at the same rate as the strangeness conserving process $d \rightarrow W^- + u$. This indeed was not the case. In 1963, Cabibbo suggested that there must be an additional dependence in the weak vertices, and proposed that the vertex for the decay $s \rightarrow W^- + u$ involves a factor of $\sin(\theta_C)$ while the decay $d \rightarrow W^- + u$ involves a factor of $\cos(\theta_C)$ to account for the more prominent strangeness conserving decay. The small quantity θ_C is the “Cabibbo angle”. With this inclusion of the dependence on angle θ_C , for

charged current interactions, the up-type quarks interact with a linear combination of down-type quarks.

This angle then motivated the need for another quark, an up-type quark later known as the charm quark, proposed by Glashow, Iliopoulos and Mainanu (GIM) in 1970. This charm quark showed to have similar strangeness conserving and changing properties such that those couplings contained factors of $-\sin(\theta_C)$ and $\cos(\theta_C)$, respectively.

This parameterization was eventually extended to include the three generations of quarks, and the quark states are given by the Cabibbo-Kobayashi-Maskawa (CKM) matrix:

$$\mathbf{V}_{\text{CKM}} = \begin{pmatrix} V_{ud} & V_{us} & V_{ub} \\ V_{cd} & V_{cs} & V_{cb} \\ V_{td} & V_{ts} & V_{tb} \end{pmatrix} \approx \begin{pmatrix} 1 & \lambda & \lambda^3 \\ -\lambda & 1 & \lambda^2 \\ \lambda^3 & -\lambda^2 & 1 \end{pmatrix}. \quad (2.1)$$

Where each entry represents the relative coupling of the quarks shown, and $\lambda \equiv \sin \theta_C \approx 0.22$. It also follows from the unitarity of the CKM matrix, $\mathbf{V}_{\text{CKM}} \mathbf{V}_{\text{CKM}}^\dagger = \mathbf{V}_{\text{CKM}}^\dagger \mathbf{V}_{\text{CKM}} = \mathbf{1}$, and that

$$V_{cd}^* V_{td} + V_{cs}^* V_{ts} + V_{cb}^* V_{tb} = 0 \quad (2.2)$$

This discussion is relevant to weak charged currents. Unfortunately, the neutral current interactions in the standard model do not involve quark mixing. This implies that an interaction in which quarks change flavor must only be through charged currents, and not through a neutral current. The only way neutral current interactions in which quarks change flavor are introduced into the standard model is through additional quantum corrections. Interactions only present through these higher order processes tend to have very small branching fractions, as is seen with

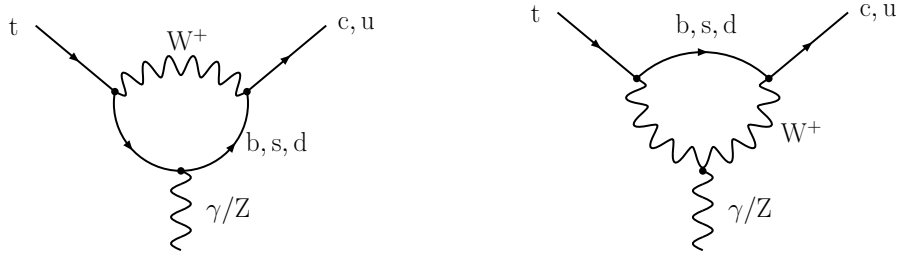


Figure 2.1: Feynman diagrams contributing to the FCNC decays at the one-loop level.

the flavor changing neutral current of the top quark, where through quantum corrections to the standard model Lagrangian, are only on the order of 10^{-14} . This suppression is discussed in the section to follow.

2.2 FCNCs in the Standard Model

In the standard model, FCNCs are highly suppressed. They do not occur at tree level, and are introduced into the standard model only by quantum corrections to the Lagrangian. The Feynman diagrams which demonstrate these “loop” corrections are shown in Figure 2.1. A search for the top quark FCNC decay was first proposed by H. Fritzsch in 1989 [1]. The branching fraction for the top FCNC decay $t \rightarrow Zq$ is proposed to be as small as $\approx 10^{-14}$, well below the experimental limits of the Tevatron or even at the Large Hadron Collider (LHC). There do exist new physics models that predict higher branching fractions up to 10^{-4} [2]; thus, any detection of this decay signature at the Tevatron would be an indication of new physics.

In terms of the Cabibbo angle, as discussed in Section 2.1.1, the matrix element of the FCNC process is obtained as a linear combination from the contributions from the d , s , and b quarks, the quarks which make up the loop. Including these

contributions,

$$\mathcal{M} \propto F(x_d) V_{cd}^* V_{td} + F(x_s) V_{cs}^* V_{ts} + F(x_b) V_{cb}^* V_{tb}, \quad (2.3)$$

where $x_i = m_i^2/M_W^2$ and m_i are the masses of the particles present in the loop, here d, s, and b. The set of functions used here are the Inami-Lim functions [3].

This equation for the matrix element is very similar to that of the unitarity relation the the CKM matrix, shown in Equation 2.2. If the masses of the quarks in the loop were identical, the matrix element for the FCNC decay would vanish. The masses are quite similar, thus giving a small value to the matrix element.

Looking at the magnitudes of the CKM matrix elements used in Equation 2.3, rewriting in terms of $\lambda \equiv \sin \theta_C$ to show the explicit dependence on the Cabibbo angle,

$$\mathcal{M} \propto (-\lambda^4) + (-\lambda^2) + \lambda^2, \quad (2.4)$$

the matrix element is shown to be proportional to λ^2 , and it is said that the decay is therefore “doubly Cabibbo-suppressed”.

2.3 Experimental Limits to Date

2.3.1 Previous Search from CDF Run-I

A previous search for the top FCNC decay was performed by the CDF experiment in 1998 [4], during the first data taking period of the experiment, Run-I. They studied the $t \rightarrow Zq$ decay at a center-of-mass energy of 1.8 TeV, using a total integrated luminosity of 110 pb^{-1} . They considered events where one top quark decays $t \rightarrow Zq$ and the other top decays via a hadronic mode $t \rightarrow Wb \rightarrow q\bar{q}'b$. Candidate events involve the Z decays $Z \rightarrow e^+e^-$ or $Z \rightarrow \mu^+\mu^-$, such that the opposite-charge

same-flavor lepton pairs are contained in $75 \text{ GeV}/c^2 < M_{l+l^-} < 105 \text{ GeV}/c^2$. Each of the four jets in signal candidate events are required to have $E_T > 20 \text{ GeV}$. With observation of only one event passing the selection requirements, a 95% C.L. upper limit is set on the branching fraction $t \rightarrow Zq < 33\%$ for a top quark mass of $175 \text{ GeV}/c^2$.

2.3.2 Previous Search from LEP

The current published best limit is from the L3 Collaboration at LEP in 2002 [5]. They studied single top production in e^+e^- annihilations, $e^+e^- \rightarrow t\bar{c}$, with center-of-mass energies from 189–209 GeV using a total integrated luminosity of 634 pb^{-1} . At this center-of-mass energy, the top quark is produced at rest, and quickly decays before hadronization. The standard model decay of the top quark $t \rightarrow Wb$ yields two final state signatures: a leptonic signature $t\bar{c} \rightarrow W^+b\bar{c} \rightarrow l^+\nu b\bar{c}$ and a hadronic signature $t\bar{c} \rightarrow W^+b\bar{c} \rightarrow q\bar{q}'b\bar{c}$. Using a neural network analysis technique, good discrimination between signal and background is seen, with no deviation from standard model backgrounds. The analysis of the non-observation of single top through $e^+e^- \rightarrow tq$ yielded an upper limit at 95% C.L. of 13.7% for a top mass of $175 \text{ GeV}/c^2$.

2.3.3 Previous Search from CDF Run-II

The most recent study of top flavor changing neutral current decays was a blind counting experiment performed using 1.1 fb^{-1} of data at the Collider Detector at Fermilab. The motivation for this thesis is based on this analysis.

The blinded region is defined as events which contain a reconstructed Z boson and four or more jets with a mass χ^2 of less than 9. The mass χ^2 variable, explained in more detail in Chapter 4.3, is constructed from W boson, the SM top mass and

Figure 2.2: The above plot shows the mass χ^2 distribution for both the tagged and anti-tagged selections. Data are overlaid with both the total background and the FCNC signal predictions at the measured 95% C.L. upper limit and shown with total systematic uncertainties. The tagged and anti-tagged selections are analyzed separately. The signal regions for the two selections are to the left of the green arrows. The main sensitivity of this search lies with the events in the tagged selection with low χ^2 .

the FCNC top mass. To increase sensitivity to such a small signal, the data sample was separated into two subsamples, one which required one identified b -quark jet in the event, and one which required zero identified b -quark jets. With signal events populating values of low χ^2 , a control region in higher χ^2 , $\sqrt{\chi^2} > 3$, was used for optimization. The optimization criteria included transverse mass $m_T \geq 200 \text{ GeV}/c^2$, leading jet $E_T \geq 40 \text{ GeV}$, second jet $E_T \geq 30 \text{ GeV}$, third jet $E_T \geq 20 \text{ GeV}$, and fourth jet $E_T \geq 15 \text{ GeV}$. Additional optimization for the counting experiment (not used in the 1.9 fb^{-1} study) included $\sqrt{\chi^2} < 1.6$ for the b -tagged selection, and $\sqrt{\chi^2} < 1.35$ for the anti-tagged selection. Using this optimization,

and normalizing the expected event yield to the top pair production cross-section measurement, an upper limit was set for the branching fraction $\mathcal{B}(t \rightarrow Zq)$ of 10.4% at 95% C.L., with an expected limit in the absence of a signal of 6.8%. This is illustrated in Figure 2.2. This result was an improvement over the CDF Run-I measurement by over a factor of three.

Chapter 3

The Experiment

The data used in this analysis were collected using the Collider Detector at Fermilab (CDF-II), a general multi-purpose detector located at the Fermi National Accelerator Laboratory (Fermilab, or FNAL). This chapter serves as an overview of the accelerator complex and the CDF-II detector, with a special emphasis on those detector components most critical to the FCNC analysis.

3.1 Fermi National Accelerator Laboratory

Fermi National Accelerator Laboratory, affectionately known as Fermilab, is located approximately 30 miles west of Chicago, Illinois. Until the commissioning of the Large Hadron Collider at CERN in 2009, the Tevatron at Fermilab remains the most energetic particle accelerator per nucleon in the world. There are five stages of acceleration which transform the protons from the nuclei of hydrogen atoms to counter-circulating beams of protons and anti-protons that each have an energy of 980 GeV [6].

As shown in Figure 3.1, protons and anti-protons are accelerated through a

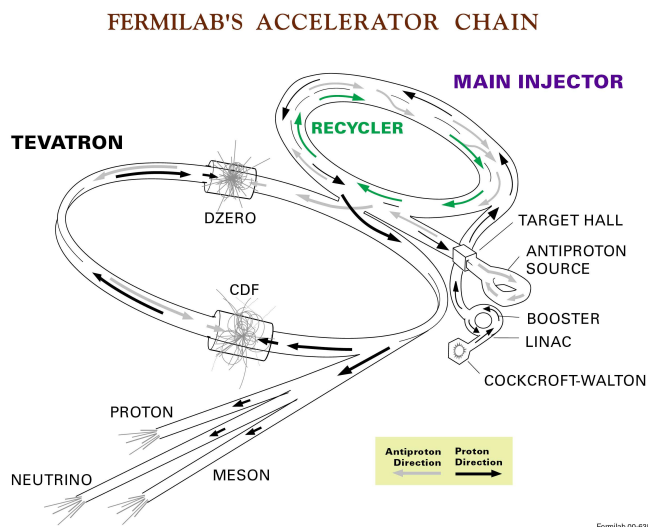


Figure 3.1: Schematic of the various Fermilab accelerator components employed in supporting Tevatron collider operations.

chain of smaller accelerators, beginning with a Cockcroft-Walton tower. The Cockcroft-Walton tower generates H^- ions by flowing hydrogen gas between a metallic cathode and anode. An electrical pulse generates an arc between the two surfaces, liberating the electrons from the metal. A magnetic field that points parallel to the cathode surface causes the electrons to travel in a tight spiral; these spiraling electrons ionize the hydrogen gas, and the H^+ ions are accelerated toward the cathode where they gain electrons from the metal surface. These resulting H^- ions are accelerated out through gaps in the anode, and leave the Cockcroft-Walton tower with an energy of 750 keV.

These ions then enter a 500 ft long linear accelerator that uses a series of time alternating electromagnetic fields at radio frequency (RF) to accelerate the H^- ions to 400 MeV. RF accelerators expose the beam of particles to a series of accelerating electromagnetic fields, each one imparting more energy to the beam. The AC nature of the linear accelerator not only accelerates the beam, but it also

separates the continuous beam of H^- ions into “bunches”.

These RF cavities are specifically designed to apply an electric field only in the direction of the beams travel to produce an acceleration. The sinusoidal nature of the time-varying electric field does not impart this acceleration automatically since throughout a complete phase of the oscillation the beam is accelerated both in its direction of travel and against, thus experiencing equal amounts of acceleration and deceleration. In order to only impart the acceleration to the beam only along the axis of its travel, it must be shielded from the decelerating fields inside of the cavity. This is done using drift tubes. A drift tube is an electrically grounded portion of the RF cavity in which the beam of particles will feel no net electric force, and is therefore shielded from the decelerating field. With the drift tubes in place, the RF cavity is then segmented into regions of electric fields only acting to accelerate the beam of particles along the axis along which it is traveling.

During the transfer to the next stage of acceleration, these ions pass through a thin carbon foil which strips the H^- ions of their electrons, leaving only the bare proton. Next, these bunches of bare protons enter the a circular accelerating ring of 475m circumference called the Booster. The protons are held on their circular path by a series of dipole magnets whose field is perpendicular to the plane of the accelerating ring. The Booster ring is a synchrotron; in each cavity, the RF frequency and the strength of the magnetic field are adjusted to be synchronous to the beam momentum and revolution frequency. With these methods, the Booster ring accelerates the protons up to 8 GeV and sends them into another accelerator, the Main Injector.

The Main Injector is also a synchrotron, accelerating the 8 GeV protons from the Booster to an energy of 150 GeV before transferring them to the Tevatron. In addition to preparing protons to be sent into the Tevatron for the colliding experiments, it provides beam to the fixed target experiments.

The production of the anti-protons begins with the 120 GeV protons from the Main Injector striking a nickel alloy target, through the interaction $p + p \rightarrow p + \bar{p} + p + \bar{p}$, with an efficiency of 16×10^{-6} . This means that for every one million protons on target, only about 16 anti-protons are produced. Anti-proton production is a very inefficient process; the ability to accumulate enough anti-protons into a focused beam is the primary limit to the luminosity of the Tevatron. The produced anti-protons will have a large energy spread, and therefore must be turned into a focused beam before being sent to the Tevatron. The method of “stochastic cooling” in a storage ring called the Debuncher reduces the spread of the anti-proton momenta relative to a central value of 8 GeV/ c in the direction of the beam. Contributions of momentum in the transverse direction are reduced as well. This 8 GeV anti-proton beam is then transferred back into the Main Injector and brought to an energy of 150 GeV to prepare for injection into the Tevatron.

The Tevatron is the final ring for the proton and anti-proton acceleration. It is a super-conducting synchrotron with a one kilometer radius. The Tevatron accelerates both the protons and anti-protons to their final collision energy of 980 GeV. At this energy, it takes only $21\mu\text{s}$ for a complete revolution. Both protons and anti-protons share the same beam pipe and magnet system, with electrostatic separators keeping the beam orbits from interacting with each other. The protons and anti-proton beams are formed into thirty-six bunches traveling in opposite directions around the ring, spiraling around each other in a helix. These beams of thirty-six bunches each are grouped into three bunches of twelve called “trains”, with 296 ns spacing in between the groups within the train, and a larger 2617 ns gap in between trains. At the CDF and D0 detector sites, the proton and anti-proton bunches are focused by super-conducting quadrupole magnets to a width of $35\mu\text{m}$ and the beams are crossed to induce the collisions.

The two collider detectors on the Tevatron are CDF and D0. The detector

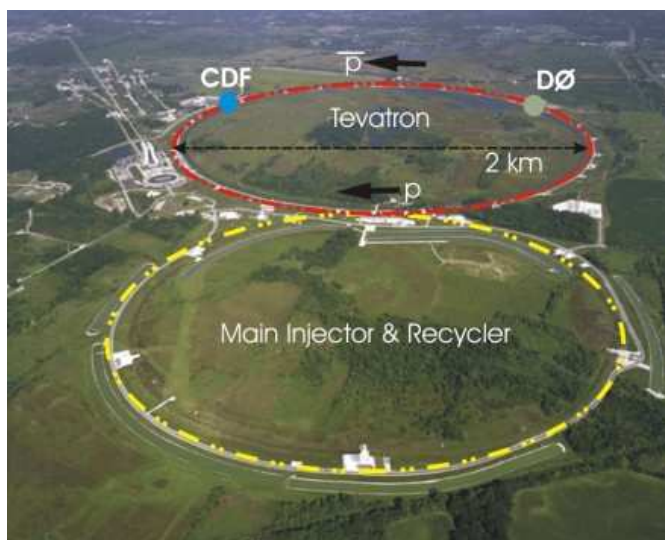


Figure 3.2: An aerial view of the Tevatron, Main Injector and locations of the CDF and DØ experiments.

used in this analysis is the Collider Detector at Fermilab, CDF, as shown in the aerial view of the Tevatron, in Figure 3.2.

3.2 The Collider Detector at Fermilab

The Collider Detector at Fermilab, CDF, was designed as a general purpose, azimuthally and forward-backward symmetric particle detector with an emphasis on precision charged particle tracking. This detector is maintained by a full-time staff of cryogenics operators and technicians and by the CDF Collaboration: an 800-physicist collaboration representing more than 60 institutions world-wide. A comprehensive description of the detector can be found elsewhere [7]; this section will concentrate on the detector components most critical to the top flavor changing neutral current analysis.

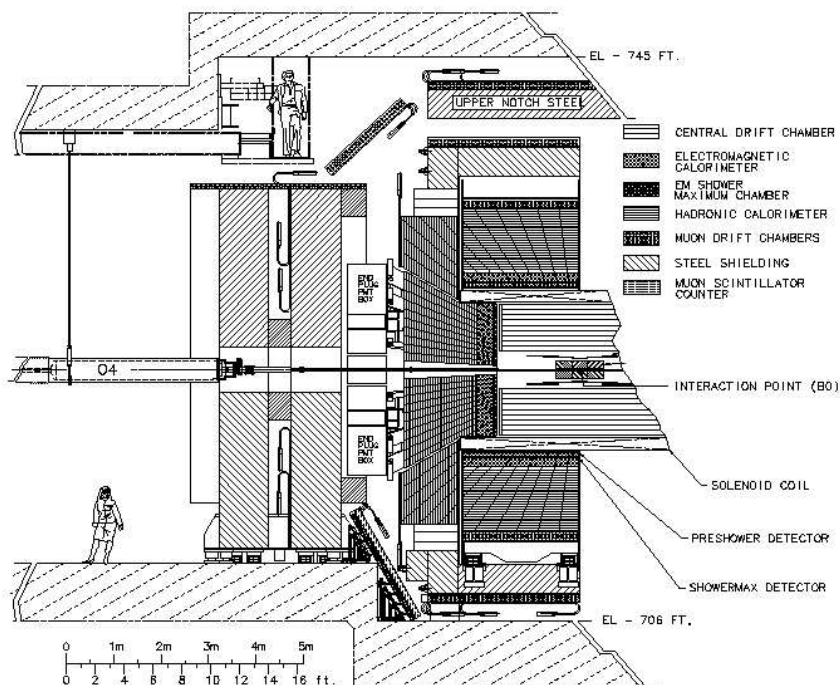


Figure 3.3: The CDF detector longitudinal view with components clearly labeled. A figure standing next to the detector is provided for scale.

3.2.1 The Detector Apparatus

The Coordinate System

The CDF detector, shown in Figure 3.3 was designed to be cylindrically symmetric around the beam line, as well as forward-backward symmetric about the collision interaction point. The detector uses cylindrical coordinates with respect to the direction of the incoming protons along the beam line, which is defined to be $+z$. This right-handed coordinate system has the transverse $x - y$ plane perpendicular to the z -axis. Using the detector's inherent polar geometry, $r = \sqrt{x^2 + y^2 + z^2}$ and $\phi = \arctan(y/x)$. The azimuthal angle ϕ is measured with respect to the x -axis, with the polar angle θ measured with respect to the z -axis. From $\theta = \arccos(z/r)$

the pseudo-rapidity is defined as:

$$\eta = -\log \tan \frac{\theta}{2} \quad (3.1)$$

from the relativistic limit of the particles rapidity, defined as

$$\zeta = \frac{1}{2} \log \left(\frac{E + p_z}{E - p_z} \right). \quad (3.2)$$

The coordinate system most commonly used is (r, η, ϕ) . This system is obtained by replacing the polar angle θ with the particles pseudo-rapidity, η , as defined above. The motivation for this preference lies in the need for a variable invariant in boosts along the z -axis, the direction of the beam. The rapidity is invariant under such boosts, and therefore so is its relativistic limit, the pseudo-rapidity. Many detector components are segmented in unit of pseudo-rapidity, as will be seen in the sections that follow.

Tracking Systems

The trajectory of charged particles emerging from a proton anti-proton collision gives valuable information about the kinematics of the interaction. Following these particles through the detector subsystems is called “tracking”. CDF’s tracking systems are placed closest to the beam pipe and are the first detector subsystems that particles pass through. The first is a silicon semiconductor tracker and the second is an open-cell wire drift chamber called the Central Outer Tracker, COT.

Both the silicon tracker and the COT are enclosed within a strong solenoidal uniform 1.4 T magnetic field; the solenoid encloses a region 2.8 m from the beam line and 3.5 m long. Charged particles in a uniform magnetic field travel in a helical trajectory; the curvature of this helix is used for charge identification and

momentum measurements of the particle.

Silicon Systems

CDF was the first detector in a hadron environment to include silicon tracking and currently has the largest operational silicon detector until the operation of the LHC. Particle tracking in CDF begins with a silicon layer mounted directly on the beam pipe. Seven more layers of silicon follow which aid in particle tracking. Having numerous layers of silicon so close to the beam pipe is critical in identifying the secondary vertex of b -jets, the jets of particles from the decay of the b -quark.

Solid state detectors, for example one made of silicon, make excellent high precision trackers. Silicon is readily available due to its commercial applications and possesses good electrical and ionization properties for use as a detector. The active part of CDF's silicon tracking system is composed of a large number of silicon wafers. When charged particles enter the semiconducting material, the charged particles ionize the material, and pairs of electrons and holes are produced. The electrons act as negative charge carriers, while the holes act as positive charge carriers.

The semiconducting material can also be "doped" by adding atoms of other elements to the semiconductors lattice structure. For example, if silicon is "n-type", it refers to the addition of an element which has more electrons than the silicon atom, and it in turn provides more electrons to the lattice. Conversely, if an atom is "p-type", it refers to doping with an element whose atoms have fewer electrons than the silicon atom. The bringing together of "n-type" and "p-type" doped silicon surfaces is called a "pn junction". The free charge carriers in the p-type and n-type silicon will recombine at the area of contact, and create a depletion region at the junction where there are no free charge carriers.

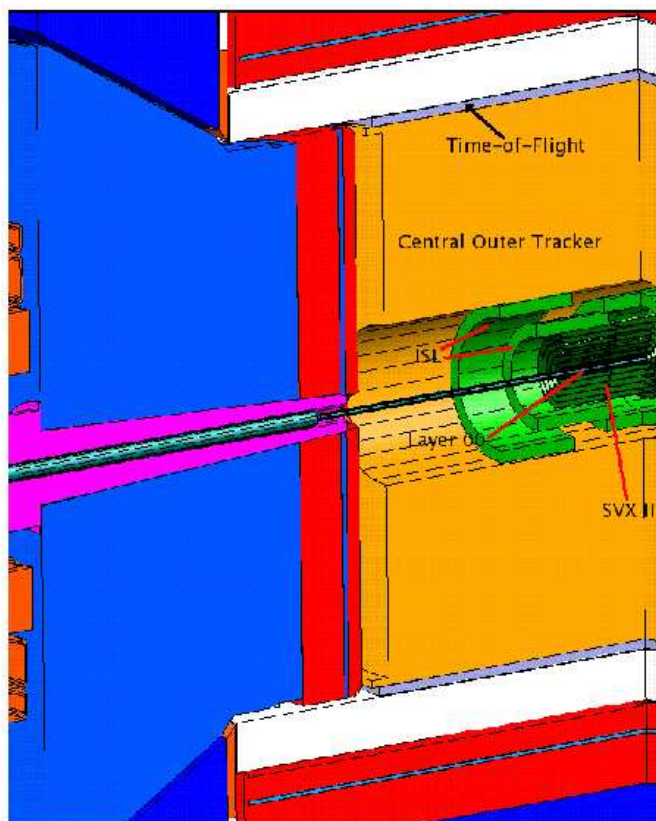


Figure 3.4: Placement of CDF tracking system components. Silicon components are in green, COT is in orange and the TOF is in blue.

The wafers consist of one type of silicon, usually an n-type. Strips of the oppositely doped silicon (here, p-type) are then applied on top of this bulk. To measure the ionized electrons from a charged particle, the depletion region must be extended by applying a voltage across the sensor. Ionized electrons from charged particles drift through the bulk towards the strip at the top where the charge is collected.

The silicon system is composed of three components: Layer-00 (L00), the Silicon Vertex Detector (SVX), and the Intermediate Silicon Layer (ISL); their relative locations are shown in Figures 3.4 and 3.5.

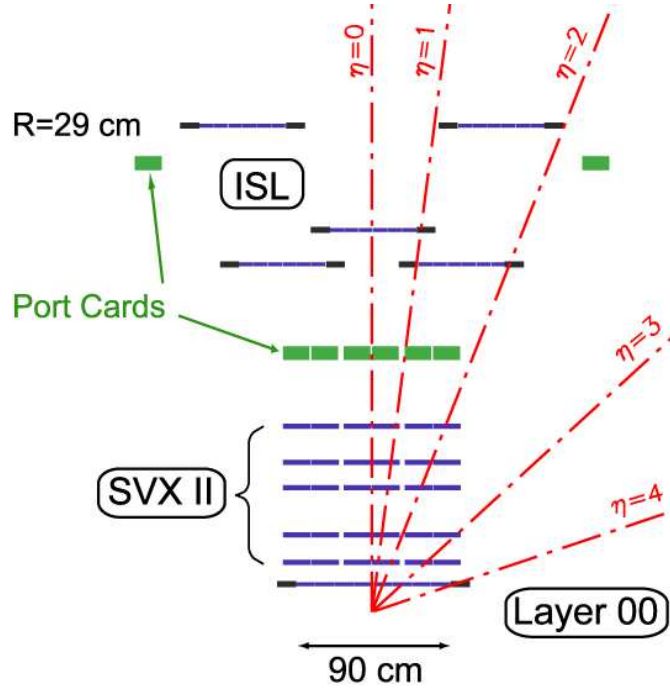


Figure 3.5: Radial placement of L00, SVXII and ISL detector components.

The Layer-00 (L00) silicon detector was not part of the original CDF technical design; it was introduced later as an enhancement to the existing silicon system to improve the impact parameter resolution on tracks and therefore the efficiency of tagging jets from b -quark production. The 90.0 cm L00 detector consists of 48 radiation-hard single-sided silicon wafers mounted directly onto the beam pipe. Each wafer uses a p-type strip implanted onto an n-type bulk. These wafers are interleaved in a 12-sided pattern as shown in Figure 3.6 . To reduce the amount of free charge carriers and to effectively prolong the life of the detector, the silicon wafers are cooled to -10°C .

Surrounding the L00 detector are the five layers of the SVX-II detector. The innermost layer is located 2.44 cm from the beam line, and the outermost layer extends to 10.6 cm. All of the wafers in the SVX-II are double sided, with a bulk

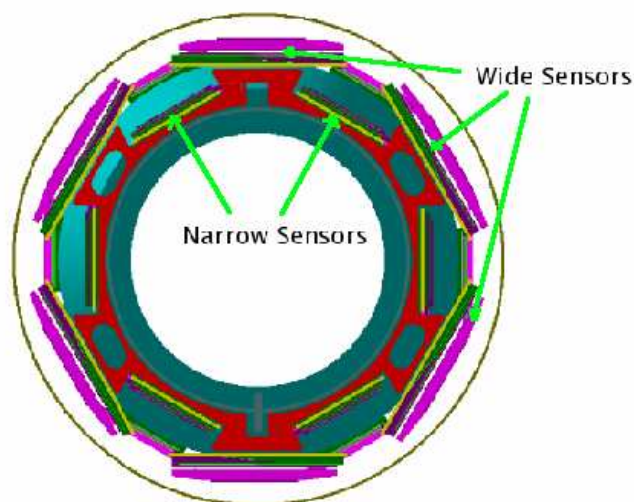


Figure 3.6: Layer 00 end view showing the alternating wide and narrow sensors displayed on a 12-sided pattern.

material of slightly n-type doped silicon. The wafers on one side have p-type strips running axially, with n-type strips on the opposite side. These silicon wafers are arranged in sets called ladders that are each four wafers long. The five layers are supported in a barrel structure with space to accommodate cooling lines. The entire SVX-II system consists of three barrels, placed end-to-end, with the nominal primary interaction from the beam in the middle of the central barrel. The SVX-II detector extends in length of 87.0 cm, and similar to L00, the silicon wafers are cooled to -10°C .

The Intermediate Silicon Layer, ISL, is located just beyond the SVX-II system. The ladders within each barrel of ISL are staggered to allow an overlapping silicon structure. The central barrel of ladders consist of one layer with staggered radii of 22.6 and 23.1 cm. The forward barrel ladders consist of two layers; the inner layer is staggered at radii of 19.7 cm and 20.28 cm, while the outer layer is staggered at radii of 28.6 cm and 29.0 cm. The purpose of the outer forward ladder is to increase

the tracking acceptance in regions of higher η . The inner layer extends in length to 65 cm, while the outer layer extends to 87.5 cm. As with the SVX-II detector, the ISL sensors are double-sided. The ISL ladders are located further away from the beam pipe than L00 and SVX, and thus they do not suffer as much radiation damage as the inner ladders. The data readout cards are also serviced by the ISL cooling lines; thus, the ISL is cooled only to $+6^\circ\text{C}$.

Wire Drift Chamber

Following the silicon detector is a wire tracking chamber called the COT. In the COT, charged particles enter the wire drift chamber and ionize the gas inside the chamber. The resulting free electrons are in an electric field, and “drift” toward the anode (the sensing wires) and away from the cathode (those wires generate the electric field). Both the position and timing are recorded.

The COT is a 310 cm long cylindrical open cell drift chamber with inner radius of 43.4 cm and an outer radius of 132.3 cm from the beam line. The chamber is filled with a 50-50 mixture of argon and ethane gases. Each measurement layer of the COT is comprised of many sense wires organized into eight superlayers, 12 wire layers each. The even numbered superlayers (2, 4, 6, and 8) are axial, oriented parallel to the beam line, while the odd numbered superlayers (1, 3, 5 and 7) are at a ± 2 degree stereo relative to the beam line. These angled layers, called stereo layers, allow reconstruction to the polar angle η and azimuthal angle ϕ of the particle’s track. The stereo wires allow resolution of z measurements within a precision of less than 5 cm. These z measurements are used as inputs into pattern recognition software. This software looks for COT hits making curves in $r - \phi$. These reconstructed curves are called tracks, and are core requirements for the identification of charged leptons, specifically electrons and muons. Quality

requirements on these tracks from the particles can be made in terms of a minimum number of hits required for both axial and stereo wires.

The momentum of charged particles can be measured from the tracking capabilities of the COT. This is because the entire tracking system, both the silicon system and the COT, are enclosed in a 1.4 T magnetic field of a superconducting solenoid; the field is parallel with the beam, pointing in the z -direction. Particles with opposite charge bend in opposite directions in the magnetic field. The radius of curvature, ρ , for these charged particle tracks is directly proportional to their momentum in that plane,

$$\rho = \frac{p_T}{0.3 \cdot B}, \quad (3.3)$$

where the radius of curvature ρ is measured in meters and the magnetic field, B , is measured in Tesla. The momentum resolution of the tracks within the COT is $\sigma_{p_T}/p_T^2 = 1.7 \times 10^3 / \text{GeVc}^{-1}$.

Calorimetry

The calorimeter surrounds the tracking volume, up to $|\eta| = 3.6$, within 3 degrees of the beam pipe, and it contains enough material to stop essentially all hadrons, photons and electrons coming from the interaction point; its goal is to measure the energy of the particles. This requires stopping the particle and collecting all of the energy deposited in the detector. It is common in high energy physics experiments for a basic calorimeter to consist of a layer of an absorbing material followed by a layer of scintillating material. The particles subsequently interact in the absorber which results in a “shower” of photons that enter the scintillating material. The energy that is deposited in the scintillator produces scintillation light via the excitation and de-excitation of the atomic electrons. The scintillation light is collected by photomultiplier tubes (PMTs).

The design of the calorimeter depends on the type of the particle to be detected. The CDF detector uses two main physical calorimeter systems of nearly identical composition: one which surrounds the tracking volume, and is centrally located about the interaction point, and one which are located in regions of higher η in the forward and backward regions of the tracking volume. Both systems are comprised of an inner electromagnetic calorimeter covering up to $|\eta| \leq 1.0$ and an outer hadronic calorimeter continuing coverage up to and including regions of $|\eta| \leq 3.6$.

CDFs calorimetry is segmented in towers, in what is called a “projective geometry” such that the boundaries between the towers are at a fixed angle with respect to the center of the detector.

High-energy electrons lose most of their energy through bremsstrahlung radiation. High energy photons lose their energy through the production of electron-positron pairs. Both of these processes take place under the influence of nuclear electric fields of the atoms in a material. Photons emitted from bremsstrahlung may be energetic enough to, in turn, pair produce. This cascade of photons and electron-positron pairs originating from a single electron or photon is called an electromagnetic shower. Electromagnetic calorimeters are designed with layers of scintillating material interleaved with lead. These showering particles generate the scintillation light, and the amount of light is recorded. The amount of scintillation light depends on the energy deposited; therefore, knowing the amount of energy deposited from the electromagnetic shower gives information to the energy of the incident electron or photon.

Outside the layers of the electromagnetic calorimeter is the hadronic calorimeter with nearly identical construction. Instead of using layers of lead, the hadronic calorimeter uses iron. The hadronic calorimeter is constructed to absorb the energy from particles more massive than electrons: particles such as protons, kaons, and

pions.

Muon Chambers

Since muons are over 200 times heavier than electrons, and only interact weakly with matter, muons with more than approximately $4 \text{ GeV}/c^2$ of energy will pass through both calorimeters without being absorbed. The muons will deposit little energy in the electromagnetic and hadronic calorimeters, so CDF has muon chambers residing outside of the calorimetry, such that particles which make it to the muon chambers are assumed to be muons. The muon chambers are wire chambers similar to those used in tracking and are once again segmented in η and ϕ . The gas used in the muon chambers is a 50% mixture of argon and ethane. Beyond these drift chambers lie scintillation counters which are used to associate muons with a particular beam crossing and for timing to reject backgrounds from out-of-time interactions, which may be the result of cosmic rays. Hits from these layers of wires gives the reconstruction of a short track, or a “stub”, which is then matched back to tracks reconstructed from the tracking system for muon identification.

For the purposes of this analysis, there are three sections of muon detectors, distinguished by geometry, but all built on the same model: the Central Muon Detector (CMU), the Central Muon Upgrade (CMP), and the Central Muon Extension (CMX) in extended regions on both η and ϕ . The CMU covers regions up to $|\eta| \leq 0.6$, and lies directly outside the central hadronic calorimeter; this close proximity to the hadronic calorimeter means that occasionally energetic particles which are not muons make their way through the hadronic calorimeter and end up making stubs in the CMU. This problem motivated the construction of the CMP. The CMP has similar angular coverage as the CMU, with the addition of steel shielding between it and the CMU to reduce the contamination of non-muons

in the muon systems. Higher regions of η are covered by the CMX; specifically $0.6 \leq |\eta| \leq 1.0$.

Luminosity Measurement

The beam luminosity measurement is determined using gas Cherenkov counters (CLC) located around the beam line in the forward region of $3.7 < |\eta| < 4.7$. The CLC serves the purpose of measuring the luminosity of each bunch of protons and anti-protons, along with separating collisions from particles in the beam bunches from those from beam losses. Particles from beam losses are typically out of time with the bunches in the Tevatron. The amplitude of the signal received from the CLC is proportional to the number of proton-anti-proton interactions. This is converted into a luminosity measurement and assigned a 6% systematic uncertainty due to the error on the knowledge of the proton-antiproton total elastic cross section [8].

3.2.2 Data Acquisition and the CDF Trigger System

Due to the frequency of interactions and particles passing through the detector, it is impossible to record every event from every collision, so CDF has implemented a 3-tier “trigger” system to filter out and record to tape only interesting events. There exist multiple lists of criteria of what is considered interesting; for example, events with high momentum jets, events with multiple detected leptons, etc.

This section serves as a brief outline of the data acquisition at CDF; a much more detailed discussion can be found elsewhere [7].

Level 1

The first level of the CDF trigger system uses the tracking, calorimeter, and muon detector information to decide, all inside a 296 ns bunch crossing window, whether to keep or discard this event. Custom hardware designed specifically for this purpose quickly reconstructs the simple event objects. The decision for keeping an event is only based on information from the COT, the calorimeters, and the muon systems. Some particle identification can be done in Level 1; for example, a track from the COT can be matched to towers of deposited energy in the calorimeters or the muon chambers to discriminate electrons from muons. Several hardware sub-processes use the information from these detector components to extract further information about the energy deposited in the calorimeters, the sum of the transverse energy in an event, the number of hits in the COT, etc and a decision is made. The data from the selected event is then filtered through to the second tier.

Level 2

The second level of the CDF trigger system is comprised of both hardware and software for the decision making, and it only deals with events that have passed all the right criteria from the Level 1 trigger. Here, decisions are made during a longer $20\mu\text{s}$, so more information can be extracted, leading to a more detailed reconstruction of the event. In addition to the information gathered from the Level 1 requirements, Level 2 decisions are made using data taken from the silicon detectors. At this level, simple clustering of calorimeter towers is performed for photon, electron, muon, and jet identification. If an event is accepted by the Level 2 requirements, then the data from the detector in its entirety is read out and used in Level 3 for this event.

Level 3

The final level of the CDF trigger system, Level 3, the full event is reconstructed in software. The data from events which passed the Level 2 requirements are sent to one of 300 commercial multi-processor machines where they are written to tape at a rate of 75Hz, as compared to the 300Hz input rate. Vetoed events are discarded, and accepted events are fully reconstructed, with calibration constants added as well as physics objects definitions used in offline studies.

3.2.3 Triggers Used for This Thesis

For the flavor changing neutral current analysis, the triggers used require energetic electrons and muons. Details of the exact trigger paths are discussed later in Section 4.6.

High E_T Electrons

The Level 1 requirements for this trigger require energy to be deposited in the central calorimeter to be at least 8 GeV, the ratio of the energy deposited in the hadronic to the electromagnetic calorimeters to be less than 0.125, and this energy deposit in the calorimeter must match with tracks in the COT that have transverse momentum, $p_T > 8.3$ GeV/ c . At Level 2, the calorimeter requirements become more stringent as the initial cluster must have energy of at least 8 GeV and have $E_T > 16$ GeV. At Level 3, the electron candidate using a clustering algorithm and the $E_T > 18$ GeV, as well as having a matched track with $p_T > 9$ GeV/ c .

High p_T Muons

High p_T muon requirements consist of a Level 1 accepted event showing stubs in both the CMU and the CMP, that are matched to a COT track with $p_T >$

4 GeV/ c . Level 2 adds the additional requirement that the track be energetic, with $p_T > 8$ GeV/ c . The Level 3 requirements show that the stub matches fully to a reconstructed track with $p_T > 18$ GeV/ c . The CMX trigger is nearly exact to that of the CMUP, except for tighter thresholds for the transverse momentum at both Level 1 and Level 2: at Level 1 the CMX stub is required to be matched to a track of at least $p_T > 8$ GeV/ c , and at Level 2, this stub must be shown to match to a fully reconstructed track of $p_T > 10$ GeV/ c .

Chapter 4

Object Identification and Event Reconstruction

The goal of this thesis is to distinguish $t\bar{t}$ events which decay with at least one top undergoing an FCNC decay from those events in which the top quark decays as expected by the Standard Model. The base event selection therefore requires exactly two charged leptons of the same flavor and of the opposite charge to reconstruct the Z boson present in the final state of an FCNC event. In addition to identifying these leptons, the final state also includes four jets: one jet from the top that decays via the FCNC decay, and three jets from the top that decays via the Standard Model, one from the quark jet, and two from the hadronically decaying W boson. The event selection is then optimized through cuts on the transverse energy of the four leading jets and on transverse mass of the event. This event selection and these optimizations are discussed in this chapter.

4.1 Object Identification

For both $Z \rightarrow e^+e^-$ and $Z \rightarrow \mu^+\mu^-$ signatures, one lepton is identified clearly as an electron or muon, using criteria developed by the CDF Collaboration. These criteria make use of information from the tracking, calorimetry and muon systems. The other lepton can either be a clearly identified electron or muon, or it can be a “track lepton”. The track lepton is a well defined object through the tracking systems, but without reference to the calorimetry or muon systems. Reconstructing these track leptons aid in recovering some lost signal acceptance since the lepton identification is not highly efficient. The analysis for this thesis does not use the $Z \rightarrow \tau^+\tau^-$ channel, since tau leptons decay very quickly and into a variety of decay products, both leptons and hadrons. The tau leptons decaying into an electron or a muon can be reconstructed as such, and those decaying hadronically are difficult to distinguish from jets.

4.1.1 Electron Identification

Electrons leave a track in the detector and deposit virtually all of their energy in the electromagnetic calorimeter. The electron selection criteria is therefore based on a track which points to a deposit of energy in the electromagnetic calorimeter. This thesis uses two specific definitions for electrons as developed by the CDF Collaboration. Central electrons deposit their energy in the central electromagnetic calorimeter, in the range $|\eta| < 1.1$, and phoenix electrons deposit their energy in the electromagnetic calorimeter in the range $1.2 \leq |\eta| \leq 2.8$. It is required that the energy deposited in the calorimeter from an electron be isolated from other energy in the event. Also, the amount of energy deposited in the electromagnetic calorimeter should be very large compared to the hadronic calorimeter, since the electromagnetic calorimeter is many radiation lengths deep.

Central Electrons

For a central electron, the transverse energy, E_T , of the cluster in the electromagnetic calorimeter must be at least 20 GeV, and the momentum of the track matched to the calorimeter cluster must be at least 10 GeV/ c . In addition, the ratio of the cluster E_T to the transverse momentum, p_T , of the track must be less than 2.0 unless the track is of high momentum, greater than 50 GeV/ c . This looser requirement on the p_T of the track is to account for the emission of photons, via bremsstrahlung radiation, as the electron passes through the material of the detector. * The electron cluster is required to be within the fiducial volume of the central electromagnetic calorimeter.

A track segment is a set of hits in the same superlayer of the COT. The track of the electron is required to have at least 3 axial segments and at least 2 stereo segments, each consisting of at least 5 hits in the COT, and the track $|z_0|$ must be less than 60 cm. These tracks are then matched to the clusters of energy in the electromagnetic calorimeter by extrapolating the track to the shower maximum detector. The distance from which the track crosses the plane of the detector should be small for the track to be considered a good match; this distance should be less than 3 cm along the direction of the beam.

The energy deposited in the calorimeters play a very important role in distinguishing electrons from jets. An isolated electron has very little energy in the areas surrounding the cluster in the electromagnetic calorimeter; the towers surrounding the electron shower are required to contain no more than 10% of the electrons total energy. The electron will deposit almost all of its energy in the electromagnetic calorimeter. The amount of energy deposited in the hadronic calorimeter

*This p_T requirement does reduce the measured p_T of the track. A possible exception is the rare case where the electron emits a photon carrying a significant amount of its momentum. Here, the photon shower will overlap with the electron shower in the calorimeter, and the measured energy of the cluster remains a good measure of the total energy deposited by the electron.

is required to be less than 5.5% of the energy deposited in the electromagnetic calorimeter.

Phoenix Electrons

Phoenix electrons have similar selection criteria to the central electrons, as the transverse energy of the cluster in the electromagnetic calorimeter must be at least 20 GeV and the electron must be within the fiducial volume of the electromagnetic calorimeter, with $1.2 < |\eta| < 2.4$. Phoenix electrons do not have an additional track momentum requirement, as the track p_T is not independent from the E_T of the calorimeter cluster in the algorithm used.

Phoenix electrons are reconstructed as a function of the number of silicon hits and the energy deposited in the electromagnetic calorimeter. The calorimeter provides an energy measurement and the information from the silicon and shower maximum detectors provide position measurements. This tracking algorithm is referred to as “Phoenix” tracking, hence the name for the reconstructed phoenix electron. This algorithm requires at least three hits from the silicon detector, and similar to the central electrons, the algorithm requires the $|z_0|$ of the track to be less than 60 cm.

Phoenix electrons must meet the same requirements on the calorimeter isolation and amount of deposited energy. The area surrounding the cluster in the electromagnetic calorimeter are required to contain no more than 10% of the electrons total energy, and the amount of energy deposited in the hadronic calorimeter is required to be less than 5.5% of the energy deposited in the electromagnetic calorimeter.

4.1.2 Muon Identification

Muons are minimum ionizing particles, so they do not interact before exiting the detector, they only ionize the material through which they pass. An important requirement for identifying muons is the presence of the ionization in detectors placed outside of the electromagnetic and hadronic calorimetry, where no other particles should reach. A properly reconstructed muon is a track that points to a track segment in the muon chambers (known as a “stub”). The different types of muons are therefore classified by the detectors that contain the track stub, the central muon chambers, the central muon upgrade, and the central muon extension. This thesis utilizes two types of muons: central muons which pass through both the central muon detector and the central muon upgrade, $|\eta| < 0.6$, and forward muons which pass through the central muon extension in higher η , up to $0.6 < |\eta| < 1.0$.

Tracks associated with muons are required to have a p_T of at least 20 GeV/ c . Forward muons have the additional requirement that the track must have traversed all layers of the COT. All stubs associated with muons are also required to reside in the fiducial volume of the respective muon detector; central muons must have stubs in both the central muon detector and the central muon upgrade detector, and forward muons must have stubs only in the central muon extension detector. These stubs must also match to their respective extrapolated tracks. Tracks for central muons are required to be within 7 cm and 5 cm from stubs in the central muon and central muon upgrade detectors, respectively. Similarly for the forward muons, they are required to be no more than 6 cm from the stub in the central muon extension detector.

Muons deposit very little energy in the calorimetry, both central and forward muons are required to deposit no more than 2 GeV of energy in the electromagnetic calorimeter and no more than 6 GeV of energy in the hadronic calorimeter, with

specific corrections made for muons of higher momentum. Isolation requirements for muons are analogous to those set for electron identification.

4.1.3 Track Lepton Identification

A track lepton is defined as a well-measured, isolated track without reference to energy deposits in the calorimeters or in the muon detectors. Track leptons are required to have $p_T > 20 \text{ GeV}/c$ and a variety of kinematic and isolation requirements. This thesis utilizes track lepton criteria from studies in a previous thesis for measuring the top quark cross section [9].

Track leptons are required to be contained in the fiducial volume of the COT, with minimum hit requirements of at least 24 axial and 20 stereo superlayer hits. Since the tracks are required to be within the fiducial volume of the COT, they are therefore limited to the range $|\eta| \leq 1.1$. In addition, information from the silicon detector is used to ensure the quality of the track. If the track has passed through at least three active layers of silicon, then it must have at least three silicon hits attached.

Isolation requirements are most important to discriminate a track lepton from a jet. Similar to how calorimeter isolation is required for leptons, isolation for tracks is defined in terms of a ratio of the tracks p_T and the energies of the tracks within a cone around the lepton track. The p_T of every track with $p_T > 0.5 \text{ GeV}/c$ in an angular region of $\Delta R < 0.4$ is summed, where the angular region is defined by $\Delta R = \sqrt{\Delta\eta^2 + \Delta\phi^2}$. The ratio of the track lepton's p_T to the sum p_T is required to be at least 0.9.

4.1.4 Jet Reconstruction

A jet is a spray of hadrons and other particles produced through the hadronization of quarks and gluons. As they pass through the detector, their energy is measured in the calorimeters. In the data, the energy is measured by selecting a single tower in the calorimeter, called a “seed” tower. These seed towers are chosen from a list of all towers containing at least 1 GeV of energy. Then, similar to energy reconstruction for tracks, surrounding towers within an angular region of $\Delta R = \sqrt{\Delta\eta^2 + \Delta\phi^2}$ are then included in the jet cluster; for this thesis, the region used is $\Delta R < 0.4$.

Unfortunately, just using the energy in the towers is not a good enough measure of the energy of the parton that initially produced the jet. The CDF Collaboration has done many studies dedicated to the response of the calorimetry to jets, and have assigned correction factors to help better estimate the energy of the parton. These jet corrections adjust the jets energy measured in the calorimeter for any nonlinearities and lost energy due to calorimeter regions not instrumented.

For this thesis, after all corrections are included, jets are used with transverse energies $E_T \geq 15$ GeV within pseudorapidities $|\eta| < 2.4$.

4.2 Event Reconstruction

The event selection for this thesis requires events having exactly two charged leptons, electrons or muons, of the same flavor and opposite charge. The invariant mass of the pair must be inside a Z mass window of 76 GeV/ c^2 and 106 GeV/ c^2 . One of the leptons must be a tight central lepton and the other lepton can either be another tight lepton of the same flavor or a track lepton. For track leptons used as electrons, and energy loss due to bremsstrahlung radiation is recovered by replac-

ing the tracks transverse momentum by the transverse energy of the central cell of the associated calorimeter cluster if the transverse energy is larger than the transverse momentum. In addition to the lepton pair, four or more reconstructed jets are required with transverse energies $E_T \geq 15$ GeV after all jet energy corrections within pseudorapidities of $|\eta| < 2.4$.

4.3 Mass χ^2 Discriminant

The decay products of a top FCNC decay can be detected by the components of the CDF-II detector, and therefore can be all utilized to reconstruct the full event kinematics. This is also helpful to distinguish the presence of the FCNC signal over the backgrounds. A mass χ^2 variable using information from the constituent particles can be constructed.

In a top FCNC event, one of the tops will decay via the standard model predictions to the type $t \rightarrow Wb$. Thus, the two jets from the hadronic decay of the W are used in this χ^2 variable, in conjunction with a third jet to reconstruct the top quark. The reconstructed Z boson is paired with the fourth jet in the event. In each χ^2 permutation, information for identifying the b -jet is not used since ambiguity arises from mis-identifying it as a charm jet as a b -jet. This overwhelms the possibility of a benefit from using the b -jet tagging information. The other top quark in an FCNC decay will decay into $t \rightarrow Zq$. The mass χ^2 is defined as

$$\chi^2 = \left(\frac{m_{W,\text{rec}} - m_{W,\text{PDG}}}{\sigma_W} \right)^2 + \left(\frac{m_{t \rightarrow Wb,\text{rec}} - m_t}{\sigma_{t \rightarrow Wb}} \right)^2 + \left(\frac{m_{t \rightarrow Zq,\text{rec}} - m_t}{\sigma_{t \rightarrow Zq}} \right)^2, \quad (4.1)$$

where, for each permutation, the masses are obtained by the following prescription:

1. The four-vectors of the four leading jets are corrected for their energies according to CDF collaboration specific corrections.

2. The invariant mass of the first two jets is calculated and the reconstructed mass of the W is formed, $m_{W,\text{rec}}$.
3. The momentum four-vectors of both of the jets used to reconstruct the W are varied within their respective resolutions to fix the mass of the reconstructed W to its value listed in the Particle Data Group book [10].
4. Using the W mass in conjunction with the third jet, the standard model top mass is reconstructed, $m_{t \rightarrow Wb,\text{rec}}$.
5. Using the two leptons in the event, the Z mass is reconstructed.
6. Similar to the W , the Z mass is fixed to its value stated in the Particle Data Group book [10] by varying the two lepton four-vectors. The assumption is used that the leptons' resolutions are constant percentages of their total momenta.
7. With the Z and the fourth jet in the event, the FCNC top mass is reconstructed, $m_{t \rightarrow Zq,\text{rec}}$.

With the above calculation for the mass χ^2 distribution, a top quark mass of $m_t = 175 \text{ GeV}/c^2$ is assumed as in the Monte Carlo simulations. The widths used in the mass χ^2 are the RMS mass found through the calculations in Monte Carlo simulation, and are $\sigma_W = 15 \text{ GeV}/c^2$, $\sigma_{t \rightarrow Wb} = 24 \text{ GeV}/c^2$, and $\sigma_{t \rightarrow Zq} = 21 \text{ GeV}/c^2$. This procedure is repeated for all possible permutations of the four leading jets in the event, and the permutation with the lowest χ^2 is selected.

4.4 Optimization of Analysis Variables

For this thesis, two signal regions are defined, one which utilizes b -tagging information, a “tagged” selection, and one which requires exactly zero b -tagged jets in

Table 4.1: The event selection criteria for this thesis.

Kinematic Variable	Optimized Cut
Transverse Mass	≥ 200 GeV
Leading Jet E_T	≥ 40 GeV
Second Jet E_T	≥ 30 GeV
Third Jet E_T	≥ 20 GeV
Fourth Jet E_T	≥ 15 GeV

the event, an “anti-tagged” selection. These two regions are optimized to obtain the best expected limit in the absence of a signal. The optimization was done separately for the two signal regions, with cuts on the transverse momenta of the four leading jets, transverse mass of the event, and mass χ^2 in addition to the base selection of $Z \rightarrow \ell^+ \ell^-$ and four or more jets. This thesis uses these exact selection criteria previously optimized. [†] The final selection criteria are summarized in Table 4.1.

It is expected that the decay products of the top quark are more central than the forward decaying Z +jets, the largest background contribution to the FCNC signal. The transverse mass of the event is sensitive to this difference. Transverse mass is defined as

$$m_T = \sqrt{\left(\sum E_T\right)^2 - \left(\sum \vec{p}_T\right)^2}, \quad (4.2)$$

where the sums include the four leading jets and the reconstructed Z . The final event selection accepts only events with $m_T \geq 200$ GeV/ c^2 .

The motivation for the variable E_T requirement of the leading jets in the event comes from the expectation that FCNC signal events contain higher energy jets, whereas for most backgrounds some of the jets come from radiation of additional partons. To improve the separation of signal and background, the jets are sorted by

[†]During the optimization process, a cut on the mass χ^2 variable was included. Since the analysis for this thesis uses the entire shape of the mass χ^2 variable, no cuts are used.

decreasing E_T and a “sliding” E_T cut is applied, i.e. $E_{T,1} \geq 40\text{ GeV}$, $E_{T,2} \geq 30\text{ GeV}$, $E_{T,3} \geq 20\text{ GeV}$, and $E_{T,4} \geq 15\text{ GeV}$ to the four leading jets in each event.

4.5 Signal and Control Regions

In addition to the two “tagged” and “anti-tagged” regions, a third “control” region is added for events with $Z \rightarrow \ell^+\ell^-$ and four or more jets. Events fall in the control region if they pass the base selection but fail at least one of the optimized selection criteria discussed above. Information from the b -jet is not used in defining the control region. The signal acceptance in the control region is a mere 10%, whereas 67% of all Z +jets events fall into the control region; therefore the control region helps to improve the sensitivity of the fit to the mass χ^2 shape by better constraining Z +jets rate and shape systematic uncertainties.

4.6 Data Sample

The data used in this thesis were collected with the CDF-II detector between March 2002 and May 2007 corresponding to an integrated luminosity of 1.9 fb^{-1} . Data runs 179057–186598 are excluded, due to the compromised tracking capabilities of the COT, and runs prior to 150145 are excluded for muons in the CMX detector, since triggering capabilities on these muons was not available. A list of the datasets and the corresponding luminosities can be found in Table 4.2. The data analyzed for this analysis were collected with inclusive lepton triggers as discussed in Section 3.2.3; the electron trigger requires $E_T > 18\text{ GeV}$, and muons are selected with $p_T > 18\text{ GeV}/c$. Due to several changes in the CMX-based triggers, some of the data include additional jet requirements, see Table 4.3 for details.

The “CDF Good Run List”, version 18 [12] is applied to the data, and it

Table 4.2: In this table, the full data taking periods, run ranges, datasets, and luminosities [11] as quoted by the CDF collaboration and used in this thesis.

Period	Run Range	Muon Dataset	Electron Dataset	Luminosity (pb^{-1})
0	138425–186598	bhmu0d	bhel0d	331.47
1–4	190697–203799	bhmu0h	bhel0h	362.94
5–7	203819–212133	bhmu0i	bhel0i	258.37
8	217990–222426	bhmu0i	bhel0i	166.29
9	222529–228596	bhmu0i	bhel0i	156.76
10	228644–233111	bhmu0i	bhel0i	243.19
11	233133–237795	bhmu0j	bhel0j	234.99
12	237845–241664	bhmu0j	bhel0j	162.01
Total				1916.02

is required that data from the silicon detector, electromagnetic calorimeter, and muon sub-detectors be marked “good.” In addition, for the period in this run list without triggering on muons from the CMX detector, these muons are removed by hand. For runs in which the beam lines were fitted only for the first 31 million Level 2 accept signals (230536, 231179, 231241, 231334, 236653, 235056, 236040), only the first 1800 run sections are used.

Table 4.3: List of trigger paths used for this thesis and their corresponding run ranges [11].

Trigger Name	Run Range
ELECTRON_CENTRAL_18_v	138425–241664
MUON_CMUP18	138425–241664
MUON_CMX18_L2	138425–200272
MUON_CMX18_L2_PT15	138425–226194
MUON_CMX18_L2_PT15_LUMI_200	200273–226194
MUON_CMX18_&_JET10	226195–241664
MUON_CMX18_&_JET10_LUMI_270	226195–241664
MUON_CMX18_&_JET10_DPS	226195–241664

Chapter 5

Acceptance for the Top FCNC Decay

The analysis of this thesis sets an upper limit on the branching fraction $\mathcal{B}(t \rightarrow Zq)$, a decay not prominent in the standard model. To calculate the acceptance for the signal of a top undergoing a flavor changing neutral current decay, all possible probabilities for the $t\bar{t}$ pair to decay into either $t \rightarrow Wb$ or $t \rightarrow Zq$ must be included. Measurements of the $t\bar{t}$ pair production cross section only consider the $t \rightarrow Wb$ decay because of its experimental prominence; therefore, the cross section used must be modified to be a function of the probability of detecting a top quark FCNC decay. Including this FCNC decay mode to the top pair production cross section yields an acceptance correction that is based on the limit set for a top FCNC decay. It is said that the acceptance correction “runs” with the $t \rightarrow Zq$ limit. The full details of this acceptance definition and calculation including the Monte Carlo samples generated for these purposes are discussed in this chapter.

Table 5.1: List of Monte Carlo samples generated for various FCNC signal channels. The abbreviation “incl.” refers to the inclusive decay of the boson shown.

$t\bar{t}$ Decays	Sample Name	Sample Size	Description
$ZcWb$	$Z(\ell\ell)W(q\bar{q}')$	539,445	Signal Monte Carlo Sample: $Z \rightarrow e^+e^-$ or $Z \rightarrow \mu^+\mu^-$, and $W \rightarrow q\bar{q}'$
$ZcWb$	$Z(\ell\ell)W(\ell\nu)$	111,181	$Z \rightarrow e^+e^-$ or $Z \rightarrow \mu^+\mu^-$ and $W \rightarrow e\nu$, $W \rightarrow \mu\nu$, or $W \rightarrow \tau\nu$
$ZcWb$	$Z(\text{incl.})W(\text{incl.})$	116,573	Inclusive Z and W decays
$ZcZc$	$Z(\ell\ell, q\bar{q})Z(\ell\ell, q\bar{q})$	116,573	Double FCNC decay: $Z \rightarrow e^+e^-$, $Z \rightarrow \mu^+\mu^-$, or $Z \rightarrow q\bar{q}$
$ZuWb$	$Z(\ell\ell)uW(q\bar{q}')$	116,573	$Z \rightarrow e^+e^-$ or $Z \rightarrow \mu^+\mu^-$ and $W \rightarrow q\bar{q}'$

5.1 Signal Monte Carlo Simulation

Monte Carlo samples representing the FCNC signature were generated using the PYTHIA event generator, version 6.216 [13], for the 1.1fb^{-1} run range (runs 141544–222426) with a top mass of $175\text{ GeV}/c^2$. The decay $t \rightarrow Zq$ is not in the list of standard decays within PYTHIA; therefore, the existing decay products of the $t \rightarrow Wd$ decay channel, which has a negligible branching fraction, were redefined to be a Z boson and a c or u quark. A discussion on incorporating the helicity discrepancies is given in Section 5.2.4.

The FCNC signal Monte Carlo samples are summarized in Table 5.1. In the main sample, there is no preference to which top quark is forced into the FCNC decay $t \rightarrow Zc$, as the other top quark is automatically forced to the Standard Model decay, $t \rightarrow Wb$. Additional MC samples include samples with different decay modes of the W and Z bosons, a sample in which the $t \rightarrow Zc$ decay is replaced by $t \rightarrow Zu$, and a “double FCNC” sample in which both top quarks decay via the FCNC $t \rightarrow Zc$.

5.2 Scaling of the Monte Carlo Simulations

The analysis for this thesis uses the Monte Carlo simulation samples generated for datasets with an integrated luminosity of 1.1 fb^{-1} . To ensure that the Monte Carlo samples used properly represent the full 1.9 fb^{-1} data set, several adjustments were made. To scale the 1.1 fb^{-1} Monte Carlo samples to the full 1.9 fb^{-1} data set used for this thesis, luminosity scaling factors were applied. To account for differences in the trigger and reconstruction efficiencies, efficiency scale factors were applied. Additionally, to ensure correctness in the efficiency for identifying b -quark jets, tagging scale factors are applied to the Monte Carlo samples.

5.2.1 Scaling for Luminosity

The Monte Carlo simulation samples are based on 1.1 fb^{-1} of data, equivalent to CDF data taking periods 0–8, or runs 141544–222426. Studies completed in the course of this thesis have shown that the kinematic variables used in this thesis do not have dependence on instantaneous luminosity, as documented in Appendix B. To appropriately represent the increased number of events in the full 1.9 fb^{-1} data sample, the Monte Carlo simulation samples are “scaled up” by an appropriate factor applied on an event-by-event basis.

As recommended by the CDF Collaboration, a method was devised for “scaling up” the existing samples with a few important assumptions. It is assumed that the detector performance remains constant through data taking periods 1–12, which is after the performance issues with CMX muon detection were resolved. A weight is therefore introduced to all reconstructed events in Monte Carlo from periods 1–8 to assure they are representative of data taken in periods 1–12. This is shown below.

$$\mathcal{L}^{0-12} = \mathcal{L}^0 + w^{\text{lumi}} \cdot \mathcal{L}^{1-8} \quad \Rightarrow \quad w^{\text{lumi}} = \frac{\mathcal{L}^{1-12}}{\mathcal{L}^{1-8}} \approx 2.0. \quad (5.1)$$

5.2.2 Scaling for Trigger and Reconstruction Efficiencies

To take into account differences seen in trigger and reconstruction efficiencies between the data and Monte Carlo samples, scale factors are applied to the Monte Carlo samples. Scale factors are applied on a per-object basis, and also take into account the added efficiency of recovering tight leptons as tracks. Each event received a scale factor of

$$\mathcal{S} = \mathcal{S}_{L1} \cdot \mathcal{S}_{L2} + (1 - \mathcal{S}_{L1}) \cdot \mathcal{S}_{L2} \cdot \mathcal{S}_{T1} + (1 - \mathcal{S}_{L2}) \cdot \mathcal{S}_{L1} \cdot \mathcal{S}_{T2}, \quad (5.2)$$

where \mathcal{S}_{L1} and \mathcal{S}_{L2} are the scale factors for the leptons, and \mathcal{S}_{T1} and \mathcal{S}_{T2} are the track scale factors for the tracks matched to these leptons.

Trigger efficiencies are also assigned, assuming that all tight leptons could fire the trigger, and that phoenix electrons and tracks would not have. The per-event trigger efficiency is then given by

$$\mathcal{E}_{\text{trig}} = \mathcal{E}_{L1} + \mathcal{E}_{L2} - \mathcal{E}_{L1} \cdot \mathcal{E}_{L2}. \quad (5.3)$$

In the above efficiency equation, \mathcal{E}_{L1} and \mathcal{E}_{L2} are the trigger efficiencies for leptons. The lepton identification and reconstruction scale factors and lepton trigger efficiencies used for the above calculations are listed in Table 5.2.

5.2.3 Scaling for b -quark Jet Efficiencies

Unfortunately, simply using the fraction of b -quark jet identified events in the Monte Carlo simulation and using this as the “tagging efficiency”, or the efficiency

Table 5.2: The scale factors and trigger efficiencies used to scale the Monte Carlo simulation estimates for electron, muon, and track reconstruction as obtained from the CDF Collaboration.

	Period 0	Periods 1–12
Central Electrons		
Trigger Efficiency	0.962±0.007	0.967±0.004
ID/Reconstruction Scale Factor	0.991±0.004	0.976±0.005
Phoenix Electrons		
ID/Reconstruction Scale Factor	0.929±0.006	0.935±0.008
Central Muons, CMUP		
Trigger Efficiency	0.902±0.004	0.920±0.006
ID/Reconstruction Scale Factor	0.936±0.006	0.923±0.007
Forward Muons, CMX (Arches)		
Trigger Efficiency	0.967±0.004	0.955±0.007
ID/Reconstruction Scale Factor	1.010±0.006	0.989±0.008
Forward Muons, CMX (Miniskirts/Keystone)		
Trigger Efficiency	—	0.866±0.012
ID/Reconstruction Scale Factor	—	0.888±0.020
Track Leptons		
Reconstruction Scale Factor	0.954 ± 0.011	

for identifying b -quark jets, is insufficient because this efficiency is lower in data than shown in Monte Carlo simulation for heavy flavor jets, meaning those containing b -quark and c -quark jets. Also, the fraction of light flavor jets that are incorrectly identified is higher in the data than in the Monte Carlo simulation. These discrepancies must be corrected on a jet-by-jet basis.

Heavy flavor jets in the Monte Carlo simulation are identified by matching b and c hadrons from a list of observed particles to jets in the event. If a b or c hadron is within an (η, ϕ) cone of $\Delta R = \sqrt{\Delta\eta^2 + \Delta\phi^2} < 0.4$ of a jet, that jet is considered to be a heavy flavor jet. Otherwise, a jet is classified as a light flavor jet. Heavy flavor jets that are not b -tagged in the Monte Carlo are considered “untagged”.

The number of tagged heavy flavor jets are re-weighted by the b -tagging scale factor, 0.95 ± 0.05 .

For light flavor jets, the tagging information from the Monte Carlo simulation is ignored. Instead, an estimation for the background of incorrectly tagged, or “mistagged” light flavor jets is calculated by applying a parameterization to the Monte Carlo jets, as recommended by the CDF Collaboration. To account for these corrections, a weight is assigned to each reconstructed Monte Carlo event that represents the probability that at least one of the jets in the event is tagged, either as a genuine heavy flavor jet or as a mistagged light flavor jet:

$$\begin{aligned} \mathcal{P}_{\text{event,tag}} &= 1 - \prod_i (\text{probability that jet } i \text{ is not tagged}) \\ &= 1 - \prod_j (1 - \mathcal{P}_{\text{mistag},j}) \cdot \prod_k (1 - \mathcal{S}_k) \cdot \prod_l 1. \end{aligned} \quad (5.4)$$

Here the index i runs over all jets, j runs over all light flavor jets, k runs over all tagged and matched heavy flavor jets, and l runs over the remaining non-tagged but jets matched to heavy flavor jets. $\mathcal{P}_{\text{mistag},j}$ is the “mistag probability”, so the expression $1 - \mathcal{P}_{\text{mistag},j}$ is the probability that the j th jet was not tagged due to it being a light flavor jet, or on that was not matched to heavy flavor. \mathcal{S}_k is the tagging scale factor, so the expression $1 - \mathcal{S}_k$ represents the remaining probability of the k th jet being b -tagged, and matched to heavy flavor, but missed in reconstruction. Finally, all jets that are not b -tagged and are not matched to heavy flavor will not be considered as a “tagged” jet. The final event tagging efficiency of a given Monte Carlo sample is then given by the sum of all per-event weights divided by the number of events.

5.2.4 Scaling for the Redefined $t \rightarrow Wd$ Vertex

Due to the fact that the $t \rightarrow Wd$ decay channel was redefined into decay products of the FCNC decay, $t \rightarrow Zc$, PYTHIA does not know the type of interaction involved at the decay vertex. Hence, PYTHIA decays the particles isotropically in their rest frame, i.e. flat in $\cos\theta^*$, the cosine of the angle between the top boost direction and the lepton with the same charge sign as the top.

All FCNC signal Monte Carlo events are re-weighted according to a Z helicity of 65% longitudinal and 35% left-handed or right-handed. This value is inspired by the prediction of the Standard Model Higgs mechanism. For a Z decaying into two charged leptons, the change from left-handed to right-handed is equivalent to studying the oppositely charged lepton. Since the CDF-II detector is approximately symmetric with respect to positively and negatively charged leptons, the Z helicity is re-weighted to be 65% longitudinal, 35% left-handed, and 0% right-handed. For the “double FCNC” decay, the events are re-weighted with the product of the individual helicity weights. Ignorance of the exact nature of the interaction is taken into account by assigning a corresponding systematic uncertainty on the signal acceptance, as described in Section 6.1.

5.3 Normalization to a Reinterpreted Top Pair Production Cross Section

The number of expected FCNC signal events as a function of the branching fraction $\mathcal{B}(t \rightarrow Zq)$ is normalized to the expected number of signal events after background subtraction in a measurement of the top pair production cross section. The decay channel used is the “Lepton+Jets” channel, where both top decays via the Standard Model $t \rightarrow Wb$, and one W boson undergoes the leptonic decay $W \rightarrow l\nu$, and

Table 5.3: Selection criteria for the $t\bar{t}$ cross section analysis requiring two or more b -tags.

Selection Criterion	Selection Cut
Lepton type	Tight central leptons: TCE, CMUP, CMX
Number of tight leptons	exactly 1
Number of jets	≥ 3
Jet E_T (Level 5 corrected)	≥ 20 GeV
Missing E_T	≥ 30 GeV
Z veto	Yes
Dilepton veto	Yes
$ z $ jet vertex	≤ 60 cm
Δz lepton-jet vertex	≤ 5 cm
H_T	≥ 200 GeV
Number of identified b -quark jets	≥ 2

the other W boson decays hadronically into two jets. In optimizing the selection for this thesis, results for the calculation of top pair production cross section were from another CDF Collaboration analysis based on 1.1 fb^{-1} of data. The resultant cross section for events which showed at least two identified b -quark jets is $\sigma_{t\bar{t}} = (8.8 \pm 1.1) \text{ pb}$. The selection criteria for the $t\bar{t}$ cross section analysis are summarized in Table 5.3.

This thesis uses the 1.9 fb^{-1} data set, and unfortunately no update of the top pair production cross section was available. The normalization information was therefore measured using the CDF Collaborations recommended procedures, and the results for the background contributions with an assumed top pair cross section of 8.8 pb are shown in Table 5.4. Observed were 277 events and with an expected 30.4 ± 8.2 events from non- $t\bar{t}$ backgrounds. The uncertainties of the cross section and their influence on this thesis are discussed in Section 6.3.

Table 5.4: Table of background contributions calculated for the Lepton+Jets selection with at least two identified b -quark jets. A $t\bar{t}$ production cross section of $\sigma_{t\bar{t}} = 8.8$ pb is assumed.

Sample	1 Jet	2 Jets	3 Jets	4 Jets	≥ 5 Jets
WW	0.0±0.0	0.5±0.1	0.5±0.1	0.2±0.0	0.1±0.0
WZ	0.0±0.0	2.6±0.3	0.8±0.1	0.2±0.0	0.0±0.0
ZZ	0.0±0.0	0.1±0.0	0.0±0.0	0.0±0.0	0.0±0.0
SM $t\bar{t}$ (8.8 pb)	0.0±0.0	32.9±5.2	90.2±14.1	113.7±17.6	41.1±6.3
Single Top (s)	0.0±0.0	8.4±1.2	2.8±0.4	0.7±0.1	0.1±0.0
Single Top (t)	0.0±0.0	2.0±0.3	1.8±0.2	0.5±0.1	0.1±0.0
$Z+LF$	0.0±0.0	1.1±0.2	0.7±0.1	0.2±0.0	0.1±0.0
$Wb\bar{b}$	0.0±0.0	33.9±13.3	10.6±4.3	2.0±0.9	0.5±0.2
$Wc\bar{c}/Wc$	0.0±0.0	6.1±2.5	2.7±1.1	0.7±0.3	0.2±0.1
Total HF	0.0±0.0	39.9±15.8	13.3±5.3	2.6±1.2	0.6±0.3
Total MC	0.0±0.0	47.5±6.8	96.9±14.9	115.6±17.8	41.5±6.4
Mistags	0.0±0.0	4.3±1.0	2.6±0.7	0.7±0.2	0.2±0.1
Non- W	0.0±0.0	2.7±1.9	0.8±1.5	0.5±1.5	0.2±1.5
Total Prediction	0.0±0.0	94.5±17.4	113.6±15.9	119.4±17.9	42.5±6.5
Observed	0.0±0.0	107.0±0.0	118.0±0.0	115.0±0.0	44.0±0.0

5.4 Acceptance Definition and Calculation

5.4.1 Acceptance Definition

The number of expected FCNC signal events is quantified through an acceptance and a tagging efficiency. The acceptance for the signal includes the branching fraction for the channel, the geometric acceptance, and the efficiency of identifying the signal in the absence of b -jet information. The acceptance for the FCNC signal Monte Carlo is determined by applying the basic event selection, as described in Chapter 4, to the signal Monte Carlo and then correcting for the known limitations of the Monte Carlo simulation.

For all FCNC signal Monte Carlo samples, the denominator of the acceptance is defined as the sum of the helicity weights (see Section 5.2.4) for events containing

a generated Z boson with its mass between $76 \text{ GeV}/c^2$ and $106 \text{ GeV}/c^2$. The numerator of the acceptance is defined as the number of reconstructed events after the above baseline selection and after helicity re-weighting and applying luminosity scaling and all per-event scale factors \mathcal{S} and efficiencies \mathcal{E} , as described by:

$$\mathcal{A}^j = \frac{\sum_i^j \mathcal{S}_i \cdot \mathcal{E}_i \cdot w_i^{\text{hel}}}{\sum_i^j w_i^{\text{hel}}}, \quad (5.5)$$

where the sums go over all events in a given data period j , and w_i^{hel} is the helicity weight of event i after applying the ‘‘CDF Good Run List’’, version 18 [12] in both the numerator and the denominator. The signal acceptance formula is derived for the case of luminosity scaling. The acceptance is the weighted average of the acceptances for period 0, \mathcal{A}^0 , and periods 1–8, \mathcal{A}^{1-8} , where the latter represents periods 1–12:

$$\mathcal{A} = \frac{\mathcal{L}^0}{\mathcal{L}^{0-12}} \cdot \mathcal{A}^0 + \frac{\mathcal{L}^{1-12}}{\mathcal{L}^{0-12}} \cdot \mathcal{A}^{1-8} = \frac{\mathcal{L}^0}{\mathcal{L}^{0-12}} \cdot \frac{\sum_i^0 \mathcal{S}_i \cdot \mathcal{E}_i \cdot w_i^{\text{hel}}}{\sum_i^0 w_i^{\text{hel}}} + \frac{\mathcal{L}^{1-12}}{\mathcal{L}^{0-12}} \cdot \frac{\sum_i^{1-8} \mathcal{S}_i \cdot \mathcal{E}_i \cdot w_i^{\text{hel}}}{\sum_i^{1-8} w_i^{\text{hel}}}. \quad (5.6)$$

The helicity weights depend only on the underlying physics process, not on the run range. This simplifies the acceptance calculation by replacing the sum of helicity weights for a run period j by its luminosity-scaled average:

$$\sum_i^j w_i^{\text{hel}} = \frac{\mathcal{L}^j}{\mathcal{L}^{0-8}} \sum_i^{0-8} w_i^{\text{hel}}. \quad (5.7)$$

Insert (5.7) into (5.6) and obtain:

$$\begin{aligned} \mathcal{A} &= \frac{\mathcal{L}^{0-8}}{\mathcal{L}^{0-12}} \left(\frac{\sum_i^0 \mathcal{S}_i \cdot \mathcal{E}_i \cdot w_i^{\text{hel}}}{\sum_i^{0-8} w_i^{\text{hel}}} + \frac{\mathcal{L}^{1-12}}{\mathcal{L}^{1-8}} \cdot \frac{\sum_i^{1-8} \mathcal{S}_i \cdot \mathcal{E}_i \cdot w_i^{\text{hel}}}{\sum_i^{0-8} w_i^{\text{hel}}} \right) \\ &= \frac{\mathcal{L}^{0-8}}{\mathcal{L}^{0-12}} \cdot \frac{\sum_i^{0-8} \mathcal{S}_i \cdot \mathcal{E}_i \cdot w_i^{\text{hel}} \cdot w_i^{\text{lumi}}}{\sum_i^{0-8} w_i^{\text{hel}}}, \end{aligned} \quad (5.8)$$

where the luminosity weights assume values of $w_i^{\text{lumi}} = 1$ for all events in period 0 and $w_i^{\text{lumi}} = \mathcal{L}^{1-12}/\mathcal{L}^{1-8} \approx 2.0$ for all events in periods 1–8.

5.4.2 Acceptance Calculation

To derive an upper limit on $\mathcal{B}(t \rightarrow Zq)$ from the number of observed candidate events, a relation can be made between the number of candidate events with the $t\bar{t}$ production cross section and the probabilities \mathcal{P} for a $t\bar{t}$ pair to decay into single FCNC ($t\bar{t} \rightarrow WbZq$) and double FCNC ($t\bar{t} \rightarrow ZqZq$) final states:

$$N_{\text{signal}} = \{(\mathcal{P}(t\bar{t} \rightarrow WbZq) \cdot \mathcal{A}_{WZ}) + (\mathcal{P}(t\bar{t} \rightarrow ZqZq) \cdot \mathcal{A}_{ZZ})\} \cdot \sigma_{t\bar{t}} \cdot \int \mathcal{L} dt, \quad (5.9)$$

where \mathcal{A}_{WZ} is the acceptance for $t\bar{t} \rightarrow WbZq$, \mathcal{A}_{ZZ} is the acceptance for $t\bar{t} \rightarrow ZqZq$, $\sigma_{t\bar{t}}$ is the $t\bar{t}$ production cross section, and $\int \mathcal{L} dt$ is the integrated luminosity. The above probabilities are products of branching fractions, based on the assumption that either top or anti-top quark can decay via the FCNC $t \rightarrow Zq$ with branching fraction $\mathcal{B}_Z \equiv \mathcal{B}(t \rightarrow Zq)$ or according to the Standard Model decay $t \rightarrow Wb$ with branching fraction $1 - \mathcal{B}_Z$:

$$\begin{aligned} N_{\text{signal}} &= \{2 \cdot \mathcal{B}_Z \cdot (1 - \mathcal{B}_Z) \cdot \mathcal{A}_{WZ} + \mathcal{B}_Z^2 \cdot \mathcal{A}_{ZZ}\} \cdot \sigma_{t\bar{t}} \cdot \int \mathcal{L} dt \\ &= \mathcal{B}_Z \cdot \mathcal{A}_{WZ} \cdot \{2 \cdot (1 - \mathcal{B}_Z) + \mathcal{R}_{ZZ/WZ} \cdot \mathcal{B}_Z\} \cdot \sigma_{t\bar{t}} \cdot \int \mathcal{L} dt, \quad (5.10) \end{aligned}$$

where $\mathcal{R}_{ZZ/WZ} \equiv \mathcal{A}_{ZZ}/\mathcal{A}_{WZ}$. For small \mathcal{B}_Z and $\mathcal{R}_{ZZ/WZ}$, the term in curly brackets is a small “running” correction factor to the main acceptance.

The measurement is normalized to the $t\bar{t}$ production cross section in the Lep-ton+Jets channel, $\sigma_{t\bar{t}}$, as described in Section 5.3. This has the advantage of removing the dependence on luminosity uncertainties and reducing many other

systematic uncertainties. The $t\bar{t}$ production cross section is calculated as

$$\sigma_{t\bar{t}} = \frac{N_{\text{LJ}} - B_{\text{LJ}}}{\mathcal{A}_{\text{LJ}} \cdot \int \mathcal{L} \, dt}, \quad (5.11)$$

where N_{LJ} is the total number of events, B_{LJ} is the number of background events, and \mathcal{A}_{LJ} is the total acceptance times branching fraction for the Lepton+Jets event selection. In order to use this $t\bar{t}$ cross-section for normalization, the acceptance times branching fraction contributions from FCNC decays must be reinterpreted:

$$\begin{aligned} \mathcal{A}_{\text{LJ}} &= \mathcal{P}(t\bar{t} \rightarrow WbWb) \cdot \mathcal{A}_{WW,\text{LJ}} + \mathcal{P}(t\bar{t} \rightarrow WbZq) \cdot \mathcal{A}_{WZ,\text{LJ}} + \mathcal{P}(t\bar{t} \rightarrow ZqZq) \cdot \mathcal{A}_{ZZ,\text{LJ}} \\ &= (1 - \mathcal{B}_Z)^2 \cdot \mathcal{A}_{WW,\text{LJ}} + 2 \cdot \mathcal{B}_Z \cdot (1 - \mathcal{B}_Z) \cdot \mathcal{A}_{WZ,\text{LJ}} + \mathcal{B}_Z^2 \cdot \mathcal{A}_{ZZ,\text{LJ}} \\ &= \mathcal{A}_{WW,\text{LJ}} \cdot \left\{ (1 - \mathcal{B}_Z)^2 + 2 \cdot \mathcal{B}_Z \cdot (1 - \mathcal{B}_Z) \cdot \mathcal{R}_{WZ/WW,\text{LJ}} + \mathcal{B}_Z^2 \cdot \mathcal{R}_{ZZ/WW,\text{LJ}} \right\}, \end{aligned} \quad (5.12)$$

where $\mathcal{A}_{WW,\text{LJ}}$, $\mathcal{A}_{WZ,\text{LJ}}$, and $\mathcal{A}_{ZZ,\text{LJ}}$ are acceptance times branching fraction of the Lepton+Jets event selection for the SM $t\bar{t}$ decay, the single FCNC decay, and the double FCNC decay, respectively. Furthermore, the acceptance ratios are defined as $\mathcal{R}_{WZ/WW,\text{LJ}} \equiv \mathcal{A}_{WZ,\text{LJ}}/\mathcal{A}_{WW,\text{LJ}}$ and $\mathcal{R}_{ZZ/WW,\text{LJ}} \equiv \mathcal{A}_{ZZ,\text{LJ}}/\mathcal{A}_{WW,\text{LJ}}$.

Inserting Equation (5.12) into (5.11) and replacing $\sigma_{t\bar{t}}$ in (5.10) with the result yields the final acceptance formula:

$$\begin{aligned} N_{\text{signal}} &= \mathcal{B}_Z \cdot (N_{\text{LJ}} - B_{\text{LJ}}) \cdot \frac{\mathcal{A}_{WZ}}{\mathcal{A}_{WW,\text{LJ}}} \cdot \\ &\quad \frac{2 \cdot (1 - \mathcal{B}_Z) + \mathcal{R}_{ZZ/WZ} \cdot \mathcal{B}_Z}{\underbrace{(1 - \mathcal{B}_Z)^2 + 2 \cdot \mathcal{B}_Z \cdot (1 - \mathcal{B}_Z) \cdot \mathcal{R}_{WZ/WW,\text{LJ}} + \mathcal{B}_Z^2 \cdot \mathcal{R}_{ZZ/WW,\text{LJ}}}_{\text{"running" acceptance correction}}} \end{aligned} \quad (5.13)$$

This equation summarizes all ingredients required to calculate the branching fraction $\mathcal{B}_Z \equiv \mathcal{B}(t \rightarrow Zq)$: the number of signal events, N_{signal} , total number of events and number of background events from the Lepton+Jets cross section measure-

ment, $N_{LJ} - B_{LJ}$, two acceptances from the FCNC event selection, \mathcal{A}_{WZ} and \mathcal{A}_{ZZ} , and three acceptances from the Lepton+Jets event selection, $\mathcal{A}_{WW,LJ}$, $\mathcal{A}_{WZ,LJ}$, and $\mathcal{A}_{ZZ,LJ}$. The signal and background numbers for the full 1.9 fb^{-1} sample are obtained as outlined in Section 5.3. The acceptances are derived from the Monte Carlo simulation.

5.5 Monte Carlo Simulation of Background Processes

The dominant source of background contributions in the search for the FCNC decay $t \rightarrow Zq$ comes from contributions from Standard Model Z s produced in association with jets, Z +jets. ALPGEN v2.10 + PYTHIA Monte Carlo samples are used for $Z+0, 1, 2, 3, 4$ partons, and for two heavy flavor samples, $Z+b\bar{b}+0, 1, 2$ partons, and $Z+c\bar{c}+0, 1, 2$ partons. ALPGEN v2.10 contains a built-in mechanism to remove the overlap between jets from parton showers and from hard scattering matrix elements at the generator level. The samples with the largest parton multiplicities, i.e. $Z+4$ partons, $Zb\bar{b}+2$ partons, and $Zc\bar{c}+2$ partons, are generated using “inclusive” matching, allowing the parton shower to fill in additional jets. For all other samples “exclusive” matching was used. The samples are listed below.

The ALPGEN samples are combined according to their relative cross sections. The light flavor samples can also contain heavy flavor from the parton shower, which constitutes another overlap between the light and heavy flavor samples that is not removed automatically, and therefore must be removed by hand. The jet-based overlap removal scheme developed by the CDF collaboration is also applied. This scheme keeps $b\bar{b}$ or $c\bar{c}$ pairs in the light flavor sample only if they come from the parton shower and are contained in the same reconstructed jet ($\Delta R < 0.4$). In

the heavy flavor samples, all events with $b\bar{b}$ and $c\bar{c}$ pairs from the matrix element are kept if they do not share the same jet.

For this thesis, ALPGEN samples are used to predict shapes of kinematic distributions and ratios of event yields for the same jet multiplicity. Since it is known that the ALPGEN Monte Carlo simulation underestimates Z +jets cross section, the jet multiplicities, and the b -tagging rates, absolute predictions of these quantities will not be derived. To try and account for these differences found between the Monte Carlo simulations and in the data, systematic uncertainties arrive due to the choice of the renormalization and factorization scale in the separate ALPGEN samples. These differences have been studied, and results are detailed in Section 6.4.2.

Smaller Backgrounds

Smaller contributions to the expected background come from Standard Model ($t \rightarrow Wb$) production and diboson (WZ , ZZ) production. For both contributions, the standard CDF Collaboration Monte Carlo samples generated with the PYTHIA event generator are used, as summarized in Table 5.6.

Standard Model $t\bar{t}$ pairs decaying into the dilepton mode $t\bar{t} \rightarrow WbWb \rightarrow \ell\nu b\ell\nu b$ contain two charged leptons that can be reconstructed within the Z mass window. Top decays of the form $t\bar{t} \rightarrow WbWb \rightarrow \ell\nu bqqb$, or more colloquially the Lepton+Jets mode, can also contribute at a much smaller rate, when one of the jets is mis-reconstructed as a lepton. The background from Standard Model $t\bar{t}$ events is enhanced in the tagged data sample, as it contains two b -jets in each event. To predict the number of Standard Model $t\bar{t}$ events expected in 1.9 fb^{-1} , a background estimation tool developed by the CDF Collaboration is used.

Events with WZ and ZZ dibosons constitute a background for FCNC events

as both contain a real Z boson with additional jets in the final state. For WZ production the number of events expected in 1.9 fb^{-1} using the theoretical cross section as given in [14] and the luminosity weights discussed in Section 5.2.1. The cross section uncertainty for WZ production includes only the theoretical uncertainty.

The ZZ production cross section, given in [14], only accounts for the case of two on-shell Z s in specific final states, assuming the zero-width approximation. The total cross section is then calculated by dividing the product of the cross section and branching fraction for these final states by their known branching fractions, a technique developed by the CDF Collaboration. Conversely, the Monte Carlo sample used in this analysis also allows for off-shell Z s and Z/γ^* interference, and the final state particles used to obtain the on-shell cross sections have different couplings to on-shell Z s than to off-shell Z/γ^* s. The extrapolation to the full cross section takes both effects into account.

The branching fraction for $Z \rightarrow b\bar{b}$ is 15%; this accounts for the enhanced ZZ events in the tagged data sample. For ZZ production, the combined uncertainties are applied from the on-shell to off-shell ratio and the theoretical uncertainties.

5.5.1 Comparison of Data to Monte Carlo Simulation

A detailed data to Monte Carlo comparison for all kinematic variables used in the analysis was performed, and the results of these studies are summarized in Appendix A. For the tagged and the anti-tagged signal regions, the control region, and the pre-tagged baseline selection, the data are compared with the sum of all expected backgrounds. The background contributions from SM $t\bar{t}$ production and diboson production are fixed to the number of expected events in 1.9 fb^{-1} . The Z +jets backgrounds are added such that the total background is normalized to the

data event yield. The expected FCNC signal shape is also shown for comparison. A Kolmogorov-Smirnov (KS) test is shown on each plot, and the Baker-Cousins χ^2 [15] is calculated for each comparison. No significant discrepancies are found in any of the variables examined.

Table 5.5: The names, cross sections, and number of events for the Z +jets Monte Carlo samples. The first block gives the Z + light flavor samples and the second and third block give the Z + heavy flavor samples.

Sample	Dataset Name	Cross Section (pb)	Number of Events
$Z \rightarrow e^+e^- + 0p$	ztopp0	158	2,639,520
$Z \rightarrow e^+e^- + 1p$	ztopp1	21.6	2,630,345
$Z \rightarrow e^+e^- + 2p$	ztop2p	3.47	536,159
$Z \rightarrow e^+e^- + 3p$	ztop3p	0.550	528,491
$Z \rightarrow e^+e^- + 4p$	ztop4p	0.099	525,065
$Z \rightarrow \mu^+\mu^- + 0p$	ztopp0	158	2,665,104
$Z \rightarrow \mu^+\mu^- + 1p$	ztopp6	21.6	2,664,729
$Z \rightarrow \mu^+\mu^- + 2p$	ztop7p	3.47	530,843
$Z \rightarrow \mu^+\mu^- + 3p$	ztop8p	0.550	536,159
$Z \rightarrow \mu^+\mu^- + 4p$	ztop9p	0.099	536,159
$Z \rightarrow e^+e^- + b\bar{b} + 0p$	ztopb0	0.511	532,205
$Z \rightarrow e^+e^- + b\bar{b} + 1p$	ztopb1	0.134	525,955
$Z \rightarrow e^+e^- + b\bar{b} + 2p$	ztopb2	0.039	405,652
$Z \rightarrow \mu^+\mu^- + b\bar{b} + 0p$	ztopb5	0.511	530,793
$Z \rightarrow \mu^+\mu^- + b\bar{b} + 1p$	ztopb6	0.134	525,695
$Z \rightarrow \mu^+\mu^- + b\bar{b} + 2p$	ztopb7	0.039	536,159
$Z \rightarrow e^+e^- + c\bar{c} + 0p$	ztopc0	1.08	699,861
$Z \rightarrow e^+e^- + c\bar{c} + 1p$	ztopc1	0.331	710,734
$Z \rightarrow e^+e^- + c\bar{c} + 2p$	ztopc2	0.107	663,518
$Z \rightarrow \mu^+\mu^- + c\bar{c} + 0p$	ztopc5	1.08	710,734
$Z \rightarrow \mu^+\mu^- + c\bar{c} + 1p$	ztopc6	0.331	710,734
$Z \rightarrow \mu^+\mu^- + c\bar{c} + 2p$	ztopc7	0.107	705,108

Table 5.6: The dataset names, cross sections, number of events in the sample, and expected number of events in 1.9 fb^{-1} for both the SM $t\bar{t}$ and the WZ and ZZ diboson Monte Carlo samples. Also included in the uncertainty calculation is the 6% luminosity uncertainty.

Sample	Cross Section (pb)	Generated Events	Events <i>b</i>-Tagged	Events Anti-Tagged	Events Control
SM $t\bar{t}$	8.8 ± 1.1	4,719,385	1.7 ± 0.2	0.7 ± 0.1	1.8 ± 0.2
WZ	3.96 ± 0.06	2,340,145	0.2 ± 0.1	1.4 ± 0.1	2.1 ± 0.1
ZZ	3.40 ± 0.25	2,323,812	0.3 ± 0.1	1.1 ± 0.1	1.8 ± 0.1

Chapter 6

Determination of Sources of Systematic Uncertainty

The systematic uncertainties for the analysis of this thesis are presented in three main categories: systematic uncertainties associated with the signal acceptance, those associated with the background processes estimation, and those associated with the normalization to the top pair production cross section measurement in the Lepton + Jets channel. Final results for this thesis derive from a template fit to the shape of the mass χ^2 kinematic variable; therefore, shape systematic uncertainties are included as well as rate systematic uncertainties in the study. Details are discussed in this chapter.

6.1 Signal Rate Systematic Uncertainties

Rate systematic uncertainties of the expected signal due to top FCNC decays have been evaluated using Monte Carlo simulations, as described in Section 5.1. In the formula for the full signal acceptance, Equation 5.13, it is the acceptance

ratio $\mathcal{A}_{WZ}/\mathcal{A}_{WW,LJ}$ that shows the largest dependence on the signal acceptance. This acceptance ratio, $\mathcal{A}_{WZ}/\mathcal{A}_{WW,LJ}$, is comprised of the acceptance of the FCNC selection for the main FCNC signal, \mathcal{A}_{WZ} , and the acceptance of the Lepton + Jets selection from Standard Model $t\bar{t}$ decays. The various uncertainties on this ratio have been studied. They are shown in detail in this section, and are outlined in Table 6.3.

Equation 5.13 includes other terms which could possibly have signal systematic uncertainties associated with them. These other terms are suppressed by a factor of $\mathcal{B}(t \rightarrow Zq)$ compared to the leading $\mathcal{A}_{WZ}/\mathcal{A}_{WW,LJ}$, and their contributions to the total signal systematic uncertainty is neglected.

Jet Energy Scale

For this thesis, the uncertainty in the measured energy for reconstructed jets are a major source of systematic uncertainties. The uncertainty that arises in the jet energy scale (JES) influences uncertainties in both the signal and the background systematic uncertainties. Depending on a jets reconstructed transverse momentum and energy, that jet could cause an event to migrate from the signal to the control region, because of the “floating E_T ” cut applied, as described in Section 4.4. The uncertainty in the JES has been estimated by varying the JES using a procedure recommended by the CDF Collaboration. For both the signal and the background rate, variations in the JES will be treated as a shape uncertainty.

Secondary Vertex Tagging of Jets

To estimate the systematic uncertainty associated with the b -tagging algorithm, the per-jet tagging probability is varied. The tagging probability and mistag probability are varied independently by $\pm 1\sigma$.

The uncertainty in the tagging probability comes from the b -tagging scale factor. This scale factor is the leading source of systematic uncertainty for the acceptance ratio, $\mathcal{A}_{WZ}/\mathcal{A}_{WW,LJ}$. Variation of these b -tagging scale factors shows the greatest difference among the systematic uncertainties in the three selection regions. The uncertainty due to the b -tagging scale factor is 5.6% for the tagged region, 16.1% for the anti-tagged selection, and 10.2% for the control region. With these differences, it becomes evident that the differences in the selection aid in the cancellation of the systematic uncertainties in the acceptance ratio. For example, the selection for the Lepton+Jets analysis is most similar to the tagged region of the FCNC analysis. Consequently, the ratio of the acceptances for these two regions has the lowest systematic uncertainty. When the selections for the acceptances differ, as in the control region, the reverse is true, as the systematic uncertainty for the acceptance ratio is amplified.

The uncertainty surrounding the incorrect identification of jets, or “mis-tagging” of jets, comes from the “ $\alpha\beta$ correction”, a correction factor applied which translates the reconstruction to an incorrect secondary vertex as a mistag. The systematic uncertainty associated with the $\alpha\beta$ correction is below 1% for all three regions.

Z Boson Helicity in Top Decays

The Monte Carlo simulations generated for the FCNC signal needed to be re-weighted to account for the redefined Z boson helicity. When the signal Monte Carlo simulations were generated, the decay vertex $t \rightarrow Wd$ was manipulated to make the $t \rightarrow Zc$ decay. Upon the manipulation, the Z boson was then decayed isotropically in its rest frame. To correct the helicity of the Z boson to match the expected Standard Model-like Higgs mechanism, the decay was re-weighted

Table 6.1: Systematic uncertainties due to the Z helicity. Shown are shifts of the acceptance ratio $\mathcal{A}_{WZ}/\mathcal{A}_{WW,LJ}$ with respect to the default Z helicity of 65% longitudinal and 35% left-handed. The total systematic uncertainty is obtained from taking half of the largest difference as the 2σ systematic uncertainty.

Helicity	Base Sel. (%)	b -Tagged (%)	Anti-Tagged (%)	Control (%)
35% LH, 65% Long.			— <i>Default</i> —	
Flat	−4.3	−4.3	−4.0	−5.1
100% Longitudinal	+5.0	+4.7	+5.1	+5.7
100% Left-Handed	−9.3	−8.8	−9.5	−10.6
100% Right-Handed	−8.6	−8.9	−7.8	−10.4
35% RH, 65% Long.	+0.2	±0.0	+0.6	+0.1
Total Uncertainty (%)	3.6	3.4	3.7	4.1

65% longitudinal and 35% left-handed. To understand how this choice for the Z helicity affects the signal acceptance, and consequently the acceptance ratio, the acceptance was recalculated for a handful of helicity choices, as listed in Table 6.1. Half of the difference between the lowest and the highest acceptance ratio was used as the 2σ systematic uncertainty, resulting in approximately 3.5%.

Lepton Scale Factors and Trigger Efficiencies

To calculate the statistical uncertainties due to the scale factors for lepton identification and reconstruction and for the trigger efficiencies, both the lepton scale factors and the trigger efficiencies are varied on a per-lepton basis. An assumption that all lepton scale factors are fully correlated is used, and they are shifted simultaneously by $\pm 1\sigma$, using the values listed in Table 5.2.

Similarly, a full correlation between all trigger efficiencies is assumed, and they are also shifted by $\pm 1\sigma$. The effect of the lepton scale factors on the acceptance ratio $\mathcal{A}_{WZ}/\mathcal{A}_{WW,LJ}$ is 0.5% for all three selections. The systematic effect due to

the trigger efficiencies is 0.2%.

Initial State and Final State Radiation

The modeling of initial state radiation (ISR) and final state radiation (FSR) in Monte Carlo simulations has an affect on the number of reconstructed jets. Since the selection for the FCNC analysis requires at least four jets, it is sensitive to the amount of ISR and FSR. Monte Carlo samples were generated to study this effect on the signal acceptance. The samples contain 50,000 FCNC signal events, and represent each of the following: more ISR, more FSR, less ISR, and less FSR. In each sample, the amount of ISR or FSR is shifted by by $\pm 1\sigma$ accordingly.

The effect of varying the amount of ISR and FSR on the acceptance ratio is shown in Table 6.2. The numerator was obtained by applying the signal event selection on each of the four samples. The denominator is taken from the CDF Collaboration on an ISR/FSR study in the context of the Lepton+Jets acceptance. The results for the effect of varying the amount of ISR and FSR on the acceptance ratio $\mathcal{A}_{WZ}/\mathcal{A}_{WW,LJ}$ are 5.1% for the tagged selection, 4.8% for the anti-tagged selection, and 4.2% for the control region.

Tagging Efficiencies in $t \rightarrow Z u$ and $t \rightarrow Z c$

The Monte Carlo simulations used in this thesis to calculate the signal acceptance for the FCNC signal only contain the channel $t \rightarrow Z c$ and not $t \rightarrow Z u$. This thesis aims to set a limit on the branching fraction $\mathcal{B}(t \rightarrow Z q)$. The difference in detecting these two channels lies in the difference in the probability for identifying b and c quarks. Using a Monte Carlo simulation sample generated for this exact purpose, one which contains the decay $W(q\bar{q}') Z(\ell\ell)u$, it is found that the the probability for a $t\bar{t} \rightarrow WbZu$ event to be b -tagged is $(91 \pm 1)\%$ of the probability for a

Table 6.2: Systematic uncertainties due to initial and final state radiation. Shown are shifts of the acceptance ratio $\mathcal{A}_{WZ}/\mathcal{A}_{WW,LJ}$ for different amounts of initial and final state radiation. The total uncertainty is obtained by adding the individual uncertainties in quadrature.

Sample	Base Selection (%)	<i>b</i> -Tagged (%)	Anti-Tagged (%)	Control (%)
More ISR	-0.2	0.3	0.1	-3.6
Less ISR	0.2	2.7	-2.8	1.1
More FSR	-0.3	2.1	-3.2	0.4
Less FSR	1.1	3.7	-2.1	1.7
Total	1.1	5.1	4.8	4.2

$t\bar{t} \rightarrow WbZc$ event to be *b*-tagged. This shows that there is a definite probability of misidentifying the *c*-quark jet in the $t\bar{t} \rightarrow WbZc$ decay as a *b*-quark jet, due to their similar reconstructions.

Using the knowledge that the Standard Model branching fraction of a top FCNC decay into a second generation *c* quark is generally larger than the branching fraction into a first generation *u* quark, the assumption constructed is that this will remain true in models of physics beyond the Standard Model, where a sizeable $t \rightarrow Zq$ branching fraction is seen. To place a systematic uncertainty on the tagging efficiency of a $t \rightarrow Zu$ event versus a $t \rightarrow Zc$ event, a “worst case scenario” is constructed, in which a large percentage, 50%, of the $t \rightarrow Zq$ decays are of the type $t \rightarrow Zu$. In this case, it is estimated that the probability of identifying at least one *b*-jet in the event is then reduced to 95.5%. This difference of 4.5% between the $t \rightarrow Zc$ case and the “worst case scenario” is added to the systematic uncertainties in both the anti-tagged and the tagged signal selections.

Parton Distribution Functions

Parton distribution functions (PDFs) affect only $t\bar{t}$ production, and not the details of the decay. The systematic uncertainty used is therefore an uncertainty on the choice of the PDFs of the proton and anti-proton. Following CDF Collaboration recommendations, the PDF systematic uncertainty used comes from an analysis on a double b -tagged Lepton+Jets cross section analysis [9], and is determined to be 0.9%.

Luminosity

The FCNC signal acceptance is normalized to the acceptance calculated for the Lepton+Jets top cross section analysis; thus the common factor of the luminosity uncertainty cancels in the ratio, as shown explicitly in Section 5.4.1.

6.2 Background Rate Systematic Uncertainties

This thesis is a shape fit analysis for the mass χ^2 kinematic variable, where the largest background rate, Z +jets production, in the control region is left as a free fit parameter. This makes the analysis largely insensitive to absolute predictions of the total background rates from Standard Model $t \rightarrow Wb$ decays and diboson WZ and ZZ production.

The systematic uncertainties assigned to these background rates are obtained by varying lepton scale factors, trigger efficiencies, b -tagging scale factors, and by varying the $\alpha\beta$ correction. Uncertainties associated with shifts in the jet energy scale (JES) are treated as a free parameter in the fit, as described in Section 7.1.

These backgrounds are also subject to an uncertainty in the luminosity measurement; the CDF Collaboration recommendation of a 6% systematic uncertainty

Table 6.3: Summary of systematic shifts of the acceptance ratio $\mathcal{A}_{WZ}/\mathcal{A}_{WW,LJ}$. In the case of asymmetric uncertainties for the upwards and the downwards shift of a parameter, the larger of the two is used. Note that the upper grouping contains those systematic uncertainties that are correlated, and the lower grouping includes those anti-correlated between the anti-tagged and the b -tagged selection.

Systematic Uncertainty (%)	Base Selection	b-Tagged	Anti-Tagged	Control Region
Lepton Scale Factor	0.5	0.5	0.5	0.6
Trigger Efficiency	0.2	0.2	0.2	0.2
ISR/FSR	1.8	4.8	5.5	4.0
Helicity Re-Weighting	3.5	3.4	3.6	4.0
Parton Distribution Functions	0.9	0.9	0.9	0.9
Jet Energy Scale	— <i>Fit Parameter</i> —			
Total Correlated	3.9	6.2	6.1	5.9
B -Tagging Scale Factor	10.2	5.6	16.1	10.2
Mistag $\alpha\beta$ Correction	0.6	0.4	1.0	0.6
$\mathcal{B}(t \rightarrow Zc)$ versus $\mathcal{B}(t \rightarrow Zu)$	0.0	4.5	4.5	0.0
Total Anti-Correlated	10.2	7.2	16.7	10.2

is assigned. All background rate systematic uncertainties are summarized in Table 6.4.

6.3 Systematic Rate Uncertainties Due to Normalization

In this thesis, the measurement of the branching fraction $t \rightarrow Zq$ is normalized to the $t\bar{t}$ pair production cross section measurement in the Lepton + Jets channel. Equation (5.13) shows that the expected number of events is dependent on the number of signal and background events, namely $N_{\text{signal}} \propto N_{\text{LJ}} - B_{\text{LJ}}$. Consequently, the statistical uncertainty associated with the Lepton+Jets signal and the total uncertainty on the background need to be added to the total systematic

Table 6.4: The summary of systematic uncertainties on the sum of the backgrounds from SM $t\bar{t}$ production and WZ and ZZ diboson production. In the case of asymmetric uncertainties for the upwards and the downwards shift of a parameter, the larger of the two is used. Note that the upper grouping contains those systematic uncertainties that are correlated, and the lower grouping includes those anti-correlated between the anti-tagged and the b -tagged selection.

Systematic Uncertainty (%)	Base Selection	b-Tagged	Anti-Tagged	Control Region
Luminosity	6.0	6.0	6.0	6.0
Lepton Scale Factor	1.3	1.4	1.4	1.3
Trigger Efficiency	0.4	0.4	0.4	0.4
Jet Energy Scale		— <i>Fit Parameter</i> —		
Total Correlated	6.2	6.2	6.2	6.2
B -Tagging Scale Factor	0.0	3.1	2.4	0.0
Mistag $\alpha\beta$ Correction	0.0	0.8	0.7	0.0
Total Anti-Correlated	0.0	3.2	2.5	0.0

uncertainty of the $\mathcal{B}(t \rightarrow Zq)$ measurement. The numerical values needed for the calculation are shown in Table 5.4. The systematic uncertainty on the signal has already been taken into account in the calculation of systematic uncertainties of the acceptance ratio $\mathcal{A}_{WZ}/\mathcal{A}_{WW,LJ}$, as shown in Table 6.3.

Using the total number of events and the number of expected background events in the Lepton+Jets channel, the number of signal events with three or more jets is expected to be $N_{LJ} - B_{LJ} = 246.6 \pm 17.5$ (stat.). To calculate the total background uncertainty, the background uncertainties in the n -jet bins ($n \geq 3$) are added in quadrature. The resulting number of expected background events with three or more jets is $B_{LJ} = 30.4 \pm 8.2$ (stat. + syst.). The total uncertainty on $N_{LJ} - B_{LJ}$ is obtained by adding the uncertainties on signal and background in quadrature, resulting in $N_{LJ} - B_{LJ} = 246.6 \pm 19.3$ (stat. + syst.) or a relative uncertainty of 7.8%.

6.4 Mass χ^2 Shape Systematic Uncertainties

This thesis' calculation of a limit on the branching fraction $\mathcal{B}(t \rightarrow Zq)$ is based on a template fit to the shape of the mass χ^2 distribution in three distinct regions: b -tagged and an anti-tagged signal regions, and a control region. This technique requires a good understanding of the systematic influences that could modify the mass χ^2 shape; this means identifying which variables shift the mean and change the shape of the $\sqrt{\chi^2}$ distribution.

To quantify what influences the shape of the mass $\sqrt{\chi^2}$, shifted distributions were constructed and compared with the default distribution. The default $\sqrt{\chi^2}$ distribution was composed of all base selection requirements, as described in Chapter 4.2. Quantitatively, the shape of a shifted distribution, s is compared to the default (base selection) distribution d , and the relative shift of the mean value was studied:

$$\text{Shift} = \frac{\langle s(\sqrt{\chi^2}) \rangle - \langle d(\sqrt{\chi^2}) \rangle}{\langle d(\sqrt{\chi^2}) \rangle}. \quad (6.1)$$

The Kolmogorov-Smirnov (KS) distance between the default and the shifted distribution is given by:

$$\text{KS Distance} = \max_{0 \leq \sqrt{\chi^2} < \infty} \left| S(\sqrt{\chi^2}) - D(\sqrt{\chi^2}) \right|, \quad (6.2)$$

where S and D are the cumulative distribution function (C.D.F.s) of s and d , respectively.

The results for the dominant background from Z +jets and for the main FCNC signal sample are summarized in Table 6.5. Uncertainties in the JES show by far the largest overall effect; details of these studies are shown in Section 6.4.1. Smaller effects come from variations in the ALPGEN parameters, detailed in Section 6.4.2. Background shape uncertainties from all other sources of background uncertainties

are shown to be negligible.

6.4.1 Shape Systematic Uncertainties Associated with the Jet Energy Scale

Systematic uncertainties on the shape of the mass χ^2 associated with the jet energy scale (JES) were studied using created templates of the mass χ^2 distribution for five different settings for shifts in the JES: nominal, $\pm 1\sigma$, and $\pm 2\sigma$. Sub-figures 6.1 (a) to (d) illustrate the shape changes due to JES uncertainties on both signal and background. Uncertainties in JES result in a large variation of both the pre-tagged Z +jets normalization and shape. The variation is smaller in the optimized selections compared to the base selection. In both cases the influence on the FCNC signal is smaller than on the Z +jets background. A comparison with data in Sub-figures 6.1 (e) and (f) shows that the pre-tagged mass χ^2 distribution is more compatible with a JES shift of -1σ than with the default JES. As JES uncertainties are the largest known shape uncertainties, they are used as representative of all shape uncertainties.

Table 6.5: An overview of shape differences due to systematics uncertainties. For the main background sample (Z +jets) and the main FCNC signal sample, shown are the mean value of $\sqrt{\chi^2}$ and the Kolmogorov-Smirnov (KS) distance between the distributions.

Sample	Systematic Uncertainty	Mean $\sqrt{\chi^2}$	Shift (%)	KS Distance ($\times 10^{-3}$)
Z +Jets	Default	2.463	0.0	-0.0
Z +Jets	JES $+1\sigma$	2.595	5.3	65.4
Z +Jets	JES -1σ	2.357	-4.3	52.9
Z +Jets	ALPGEN $qfac = ktfac = 0.5$	2.449	-0.6	11.1
Z +Jets	ALPGEN $qfac = ktfac = 2.0$	2.521	2.3	42.4
Z +Jets	Lepton SF $+1\sigma$	2.464	0.0	0.0
Z +Jets	Lepton SF -1σ	2.463	0.0	0.0
Z +Jets	Trigger Efficiency $+1\sigma$	2.463	0.0	0.0
Z +Jets	Trigger Efficiency -1σ	2.463	0.0	0.0
Z +Jets	B -Tagging SF $+1\sigma$	2.463	0.0	0.0
Z +Jets	B -Tagging SF -1σ	2.463	0.0	0.0
Z +Jets	$\alpha\beta$ Correction $+1\sigma$	2.463	0.0	0.0
Z +Jets	$\alpha\beta$ Correction -1σ	2.463	0.0	0.0
FCNC $Z(\ell\ell)W(q\bar{q}')$	Default	1.274	0.0	-0.0
FCNC $Z(\ell\ell)W(q\bar{q}')$	JES $+1\sigma$	1.284	0.8	7.6
FCNC $Z(\ell\ell)W(q\bar{q}')$	JES -1σ	1.265	-0.7	7.3
FCNC $Z(\ell\ell)W(q\bar{q}')$	Helicity Flat	1.274	0.0	1.0
FCNC $Z(\ell\ell)W(q\bar{q}')$	Helicity 100% Longitudinal	1.278	0.3	2.4
FCNC $Z(\ell\ell)W(q\bar{q}')$	Helicity 100% Left-Handed	1.265	-0.7	5.2
FCNC $Z(\ell\ell)W(q\bar{q}')$	Helicity 100% Right-Handed	1.278	0.4	5.0
FCNC $Z(\ell\ell)W(q\bar{q}')$	Helicity 35% Right-Handed	1.278	0.3	3.1
FCNC $Z(\ell\ell)W(q\bar{q}')$	More ISR	1.294	1.6	11.1
FCNC $Z(\ell\ell)W(q\bar{q}')$	Less ISR	1.266	-0.6	8.6
FCNC $Z(\ell\ell)W(q\bar{q}')$	More FSR	1.273	-0.0	7.2
FCNC $Z(\ell\ell)W(q\bar{q}')$	Less FSR	1.272	-0.1	7.6
FCNC $Z(\ell\ell)W(q\bar{q}')$	Lepton SF $+1\sigma$	1.274	0.0	0.0
FCNC $Z(\ell\ell)W(q\bar{q}')$	Lepton SF -1σ	1.274	-0.0	0.0
FCNC $Z(\ell\ell)W(q\bar{q}')$	Trigger Efficiency $+1\sigma$	1.274	0.0	0.0
FCNC $Z(\ell\ell)W(q\bar{q}')$	Trigger Efficiency -1σ	1.274	-0.0	0.0
FCNC $Z(\ell\ell)W(q\bar{q}')$	B -Tagging SF $+1\sigma$	1.274	0.0	-0.0
FCNC $Z(\ell\ell)W(q\bar{q}')$	B -Tagging SF -1σ	1.274	0.0	-0.0
FCNC $Z(\ell\ell)W(q\bar{q}')$	$\alpha\beta$ Correction $+1\sigma$	1.274	0.0	-0.0
FCNC $Z(\ell\ell)W(q\bar{q}')$	$\alpha\beta$ Correction -1σ	1.274	0.0	-0.0

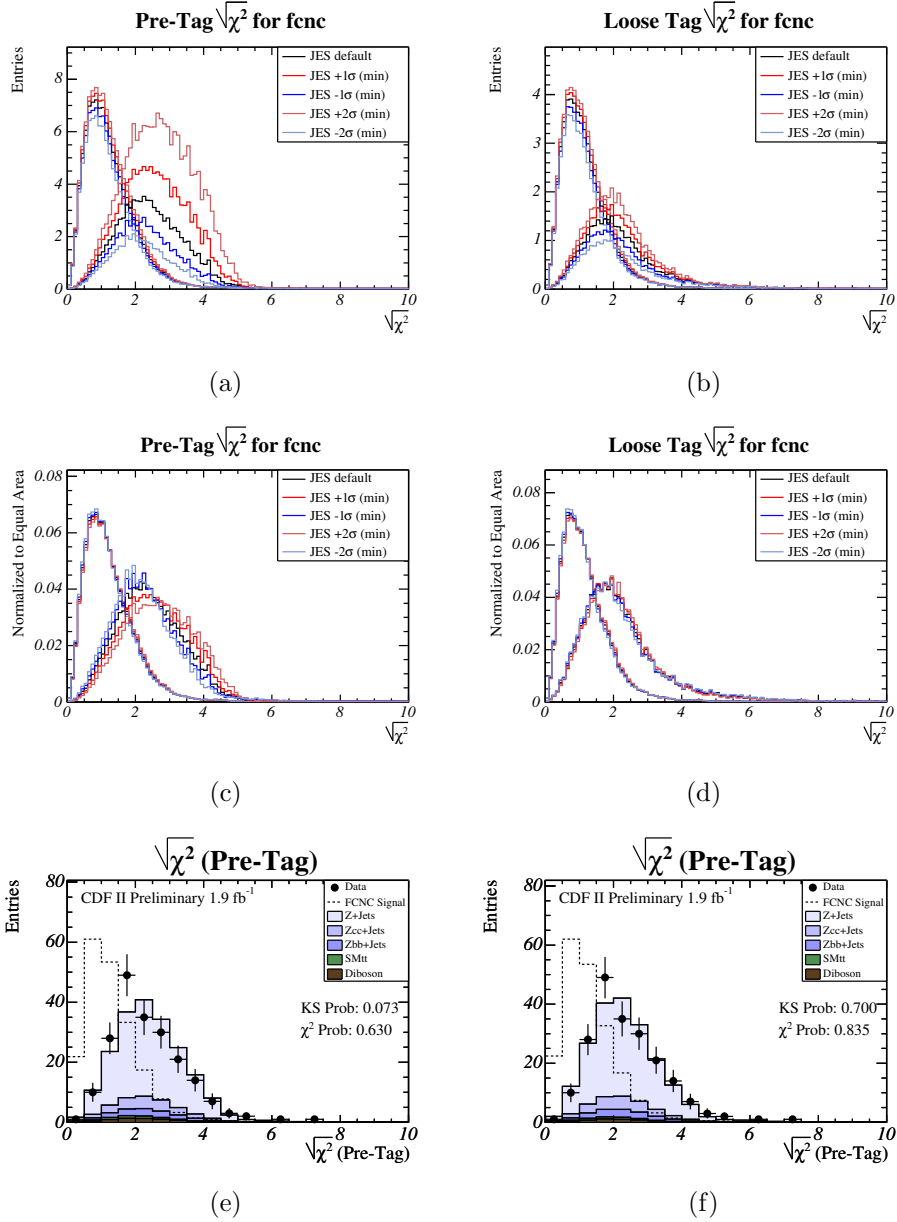


Figure 6.1: Shown are the JES templates used to fit the mass χ^2 distribution; FCNC signal peaks below $\sqrt{\chi^2} = 1$ and the Z +jets templates above $\sqrt{\chi^2} = 2$. (a) The unnormalized templates for the base selection. (b) The unnormalized templates for the b -tagged selection, magnified by a factor of 10. (c) and (d) The same templates as in (a) and (b), but normalized to equal area. Comparison of the pre-tagged χ^2 shapes in data with background for (e) nominal JES and (f) JES shifted by -1σ .

6.4.2 Shape Systematic Uncertainties Associated with the Choice of ALPGEN Parameters

As shown in Table 6.5, the second largest variation on the background normalization is the choice of the parameters for the ALPGEN Monte Carlo generator, namely the choices for the renormalization and factorization scale and the vertex energy scale. The default settings for the renormalization and factorization energy scale is $Q = \text{qfac} \times \sqrt{M_Z^2 + \sum p_T^2(p)}$, where qfac is a multiplicative factor set to 1.0. The vertex energy scale is given by $Q = \text{ktfac} \times p_T$, with a default value of $\text{ktfac} = 1.0$. The effect of these scales on the shape of the mass χ^2 are calculated by varying the values of qfac and ktfac . Special Monte Carlo samples for this exact purpose were generated, where qfac and ktfac are varied at the same time to values of 0.5 and 2.0.

The systematic uncertainties on the total Z +jets rate associated with ALPGEN uncertainties are irrelevant because the number of Z +jets events in the control region is a free parameter in the likelihood fit. The uncertainties of the χ^2 shape due to the choice of the ALPGEN parameters are much smaller than the uncertainties due to JES variations. To verify that the JES uncertainty can be used to represent the total shape systematic uncertainty on the signal, pseudo-experiments were generated with shifted χ^2 shapes according to the ALPGEN uncertainties. They were then fit assuming that the shift came from the JES uncertainty. A bias of +0.21% in the average measured branching fraction $\mathcal{B}(t \rightarrow Zq)$ was observed; this bias is small compared to the typical RMS of the distribution of pseudo-experiments of approximately 2.5%. This bias is taken into account by “smearing” all pseudo-experiments with a Gaussian random number from a distribution with a width of 0.21%.

Chapter 7

Calculation of an Upper Limit on

$\mathcal{B}(t \rightarrow Zq)$

To calculate an upper limit on the branching fraction $\mathcal{B}(t \rightarrow Zq)$, the best fit to the data is acquired with a custom maximum likelihood fitter with its framework based on Minuit [16]. To derive an upper limit on the branching fraction $\mathcal{B}(t \rightarrow Zq)$, a customized Feldman-Cousins expected limit technique [17] with systematic uncertainties included is used. This chapter will serve to outline the details of the likelihood fitter and its configuration, and to show the calculation of the expected limit.

7.1 The Maximum Likelihood Fitter

The template fit is a binned maximum likelihood fit based on Minuit. The fitter is customized to take into account correlations between bins and the constraints that are put on the calculation. The branching fraction $\mathcal{B}(t \rightarrow Zq)$ is a fit parameter of the fitter, and is one of the several parameters of interest in this thesis. The fitter

is configured in the following way:

1. The branching fraction \mathcal{B}_Z is a free parameter in the fit. Although there is a possibility of calculating an unphysical region for \mathcal{B}_Z , for example a negative value for the branching fraction, the Feldman-Cousins construction permits setting a limit in an unphysical regime; however, the Poisson probability is ill defined for a negative number of expected events. This is corrected for by not allowing the content of any template bin to be less than 0.01.
2. The shift in the jet energy scale (σ_{JES}) is a free fit parameter.
3. The number of Z +jets events in the signal region, $Z_{\text{signal}} \equiv Z_{\text{tagged}} + Z_{\text{anti}}$ is related to the number of Z +jets events in the control region, Z_{control} , by a Gaussian constraint imposed on the ratio of the number of events in the signal region to those in the control region, $\mathcal{R}_{\text{sig}} \equiv Z_{\text{signal}}/Z_{\text{control}}$. Details are provided later in Section 7.1.2.
4. The distribution of the number of Z +jets events in both signal regions is controlled by the tagging fraction, $f_{\text{tag}} \equiv Z_{\text{tagged}}/Z_{\text{signal}}$; f_{tag} is a free parameter in the fit.
5. The event counts in the two signal regions are given by:

$$Z_{\text{tagged}} = f_{\text{tag}} \cdot Z_{\text{signal}} = f_{\text{tag}} \cdot \mathcal{R}_{\text{sig}} \cdot Z_{\text{control}}, \quad (7.1)$$

$$Z_{\text{anti}} = (1 - f_{\text{tag}}) \cdot Z_{\text{signal}} = (1 - f_{\text{tag}}) \cdot \mathcal{R}_{\text{sig}} \cdot Z_{\text{control}}. \quad (7.2)$$

7.1.1 Templates Used in the Likelihood Fitter

Using the configurations and input parameters mentioned in the previous section, templates for both the FCNC signal and for the background processes were gen-

erated. All templates are adjusted to specific values in shifted JES.

Two signal templates were generated, one which represented the single FCNC decay signal $Z(\ell\ell)W(q\bar{q}',\ell\nu)$, and one for the double FCNC channel $Z(\ell\ell,q\bar{q})Z(\ell\ell,q\bar{q})$. The normalization for the templates vary s a function of the main fit parameter, $\mathcal{B}(t \rightarrow Zq)$ by the acceptance formula, shown in Equation 5.13. This effect is demonstrated in Figure 7.1.

The contributions from background Z events containing light flavor and heavy flavor jets ($c\bar{c}$, $b\bar{b}$) from the Z +jets background contributions show very similar mass χ^2 shapes, so these samples are combined into a single template for each of the three signal regions. Each sample is properly weighted according to their relative cross-sections according the the ALPGEN Monte Carlo generator. The number of Z +jets events in the control region is a free parameter in the fit, but the ratio $\mathcal{R}_{\text{sig}} = Z_{\text{signal}}/Z_{\text{control}}$ is used as a constraint. This is discussed later in Section 7.1.2.

The number of events expected in the smaller background channels, namely SM $t\bar{t}$ and WZ and ZZ diboson production, is fixed to the predicted number of events in 1.9 fb^{-1} , as shown in Table 5.6.

7.1.2 Using the Control Region to Constrain the Signal Regions

In Monte Carlo simulation, $\mathcal{R}_{\text{sig}} \equiv Z_{\text{signal}}/Z_{\text{control}}$ is measured to be $\mathcal{R}_{\text{sig}} = 0.51$. The ALPGEN Monte Carlo simulations with varied renormalization and factorization scales and vertex energy scales are used to estimate the uncertainty on this number. The ratio varies from $\mathcal{R}_{\text{sig}} = 0.43$ for $\text{qfac} = \text{ktfac} = 2.0$ to $\mathcal{R}_{\text{sig}} = 0.56$ for $\text{qfac} = \text{ktfac} = 0.5$. A conservative uncertainty of $\mathcal{R}_{\text{sig}} = 0.51 \pm 0.10$ is used, and \mathcal{R}_{sig} is constrained within 20%. As mentioned previously in Chapter 6, shifts

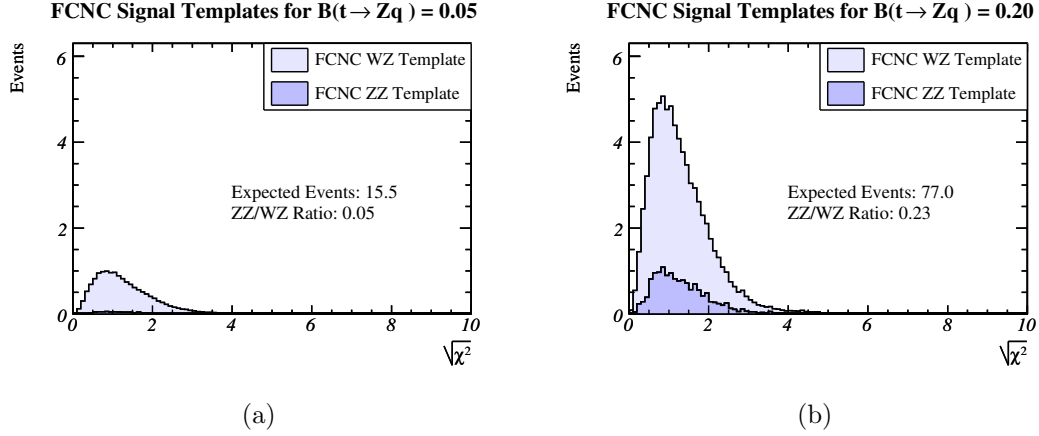


Figure 7.1: Full FCNC signal template for different assumed branching fractions $\mathcal{B}(t \rightarrow Zq)$. (a) $\mathcal{B}(t \rightarrow Zq) = 5\%$. (b) $\mathcal{B}(t \rightarrow Zq) = 20\%$.

in the JES also play a very large role in the shape systematic uncertainties for this analysis, and \mathcal{R}_{sig} will vary as a function of the shift in JES. The fitter accounts for this dependence on the shift in JES, σ_{JES} , by parameterizing $\mathcal{R}_{\text{sig}}(\sigma_{\text{JES}})$ with a third order polynomial, keeping the same relative uncertainty of 20%, as shown in Fig. 7.2.

7.2 The Feldman-Cousins Limit Calculation

The template fit used in this thesis returns a value for the branching fraction, $\mathcal{B}(t \rightarrow Zq)$, with systematic uncertainties included. To convert this central value returned by the likelihood fitter into a limit, the Feldman-Cousins framework is used. Details on this prescription can be found elsewhere [18]. This method of limit calculation is very useful in this analysis since the Feldman-Cousins framework gives the proper coverage for a 95% confidence region. The Feldman-Cousins method also has the ability to distinguish a one-sided interval from a two-sided

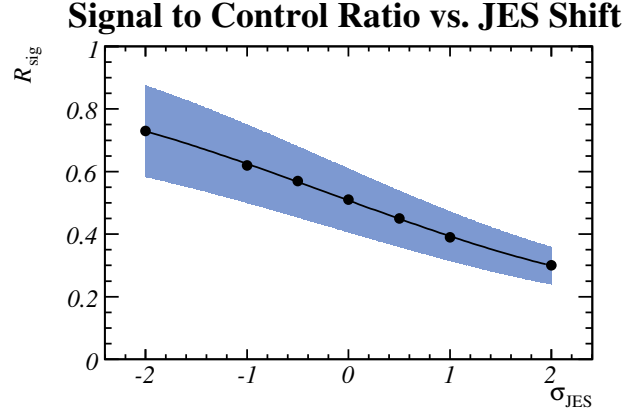


Figure 7.2: An illustration of the constraint on the ratio \mathcal{R}_{sig} of the number of Z +jets events in the signal regions over the number of Z +jets events in the control region as a function of the jet energy scale shift, σ_{JES} .

interval; meaning that this statistical method can distinguish the cases of setting a limit from making a measurement.

The Feldman-Cousins method constructs intervals using a likelihood ordering principal, based on the likelihood ratio

$$\mathcal{R}(\mathcal{B}_{\text{meas}}|\mathcal{B}_{\text{true}}) = \frac{\mathcal{P}(\mathcal{B}_{\text{meas}}|\mathcal{B}_{\text{true}})}{\mathcal{P}(\mathcal{B}_{\text{meas}}|\mathcal{B}_{\text{best}})} \quad (7.3)$$

where $\mathcal{P}(\mathcal{B}_{\text{meas}}|\mathcal{B}_{\text{true}})$ is the probability to measure an FCNC branching fraction of $\mathcal{B}_{\text{meas}}$ given the true branching fraction $\mathcal{B}_{\text{true}}$. $\mathcal{P}(\mathcal{B}_{\text{meas}}|\mathcal{B}_{\text{best}})$ is the largest probability obtained for $\mathcal{B}_{\text{meas}}$ for any $\mathcal{B}_{\text{true}}$ in the physical range. These probabilities are calculated using Monte Carlo simulations, called pseudo-experiments. Details on these probabilities, and how they are constructed from pseudo-experiments are described in the sections to follow.

7.2.1 Pseudo-Experiments Used in the Limit Calculation

The Feldman-Cousins limit technique is employed in this thesis, and it must be customized to include the systematic uncertainties encountered in the analysis. This is done by including them in the pseudo-experiments used for the Feldman-Cousins construction. These pseudo-experiments take into account all of the systematic effects and the correlations present in the analysis.

The pseudo-experiments for the Feldman-Cousins construction are generated in the following way:

1. The shift in JES (σ_{JES}) is a free fit parameter. A random JES shift is drawn from a unit Gaussian distribution, and template morphing is used to get interpolated versions of all of the templates for that generated JES shift. Aspects of template morphing are described below in Section 7.2.2.
2. The signal templates for the single and double FCNC decays are combined for the assumed true branching fraction $\mathcal{B}(t \rightarrow Zq)$ according to the running acceptance formula, Equation 5.13.
3. The number of expected FCNC signal events are “smeared” according to the total systematic rate uncertainties, both correlated and uncorrelated, given in Table 6.3.
4. Using calculations for the Z +jets background contribution from the 1.1 fb^{-1} results, the expected number of Z +jets events in the control region are estimated, Z_{control} .
5. The ratio \mathcal{R}_{sig} is generated randomly from a Gaussian distribution with a mean of $(51 \pm 10)\%$ to obtain the expected number of Z +jets events in the two signal regions using the relation $Z_{\text{signal}} = \mathcal{R}_{\text{sig}} \cdot Z_{\text{control}}$. The mean is

adjusted according to the generated JES shift, as outlined in Section 7.1.2, while keeping the same relative uncertainty of 20%.

6. The tagging fraction, f_{tag} , is generated from a Gaussian distribution with mean and width of $(15 \pm 2)\%$, based on the background tagging rates measured in 1.1 fb^{-1} of data. Both Z_{tagged} and Z_{anti} are obtained according to Equations 7.1 and 7.2, respectively.
7. The total number of expected events from the smaller backgrounds are also “smeared” according to their systematic rate uncertainties, shown in Table 6.4.
8. Poisson random numbers are drawn from the constructed signal and background templates to generate the pseudo-experiment. Thirty-three sets of pseudo-experiments, each containing 250,000 events, were generated for true values of the branching fraction $\mathcal{B}(t \rightarrow Zq)$ from 0% to 16%.

7.2.2 Template Morphing

An interpolation technique called template morphing has been used in the likelihood fitter and in the generation of pseudo-experiments for this thesis. Template morphing treats the shape fits as continuous nuisance parameters, with the ability to add constraints. For a given shift parameter, all of the templates are recalculated, and then fit by the likelihood fitter.

The linear interpolations that need to be performed are between histograms by “compound horizontal template morphing”, described in [19] and [20]. In Figure 7.3, an illustration of template morphing between histograms is shown. The first step is to integrate the source and target histograms to generate their cumulative distribution functions (C.D.F.s). Next, horizontal line segments are drawn

Figure 7.3: Illustration of compound horizontal template morphing. A 75% morphed histogram is obtained by (a) constructing cumulative distribution functions (C.D.F.s) of the two source histograms, (b) constructing a new C.D.F. by dividing each horizontal line segment between the C.D.F.s at a fractional length of $\lambda = 0.75$, and (c) taking the derivative of the resulting C.D.F.

between points on both C.D.F.s. The C.D.F. for the interpolated histogram is generated from the horizontal line segments, using fractions λ of the source and $1 - \lambda$ of the target histogram. The points on the line segments are connected, and the full C.D.F. of the interpolated histogram is generated. The histograms are recovered by differentiating the resulting C.D.F.s.

7.2.3 The Feldman-Cousins Construction

Using the pseudo-experiments, described in Section 7.2.1, the Feldman-Cousins bands are constructed following the prescription in [18].

Using the generated pseudo-experiments based on the true values for $\mathcal{B}(t \rightarrow Zq)$, $\mathcal{B}_{\text{true}}$, the likelihood ratio is constructed, as shown in Equation 7.3. For a single given $\mathcal{B}_{\text{true}}$, the numerator of Equation 7.3 is given by a distribution of pseudo-experiments generated at that $\mathcal{B}_{\text{true}}$. An example of a set of pseudo-experiments generated at $\mathcal{B}_{\text{true}} = 3.75\%$ and filled into a histogram is shown in

Figure 7.4 (a).

The denominator of the likelihood ratio is also generated from pseudo-experiments. The quantity $\mathcal{P}(\mathcal{B}_{\text{true}}|\mathcal{B}_{\text{meas}})$ is created by gathering the bin contents for a given interval in $\mathcal{B}_{\text{meas}}$ from the histograms of pseudo-experiments for all $\mathcal{B}_{\text{true}}$. This gives a distribution of $\mathcal{B}_{\text{true}}$ for a $\mathcal{B}_{\text{meas}}$. An illustration of this technique is shown in Figure 7.4 (b). For a given value of $\mathcal{B}_{\text{meas}}$ in the physical range of values for a branching fraction ($\mathcal{B}_{\text{meas}} \geq 0$), the quantity $\mathcal{B}_{\text{best}}(\mathcal{B}_{\text{meas}})$ is the position of the maximum in the $\mathcal{P}(\mathcal{B}_{\text{true}}|\mathcal{B}_{\text{meas}})$ distribution. The quantity $\mathcal{P}(\mathcal{B}_{\text{meas}}|\mathcal{B}_{\text{best}})$ is the maximum value, and is determined by fitting to a double bifurcated Gaussian distribution. For regions $\mathcal{B}_{\text{meas}}$, where it is unphysical, the best $\mathcal{B}_{\text{true}}$ is chosen to be $\mathcal{B}_{\text{true}} = 0$. The maxima are plotted and fit to parameterize $\mathcal{P}(\mathcal{B}_{\text{meas}}|\mathcal{B}_{\text{best}})$ as a function of $\mathcal{B}_{\text{meas}}$, as shown for example in Figure 7.4 (c).

Likelihood ratios $\mathcal{R}(\mathcal{B}_{\text{meas}}|\mathcal{B}_{\text{true}})$ of Equation 7.3 for all available values of $\mathcal{B}_{\text{true}}$ are constructed. The value of the likelihood ratio for a given $\mathcal{B}_{\text{meas}}$ is then plotted, and then fit with a continuous function to generate a distribution for $\mathcal{B}_{\text{meas}}$. This is illustrated in Figure 7.4 (d). From this distribution of the likelihood ratio for a single value of $\mathcal{B}_{\text{true}}$, the smallest possible interval in $\mathcal{B}_{\text{meas}}$ is found such that 95% of all pseudo-experiments are contained. This value of the likelihood ratio is the value for the Feldman-Cousins band for the given $\mathcal{B}_{\text{true}}$.

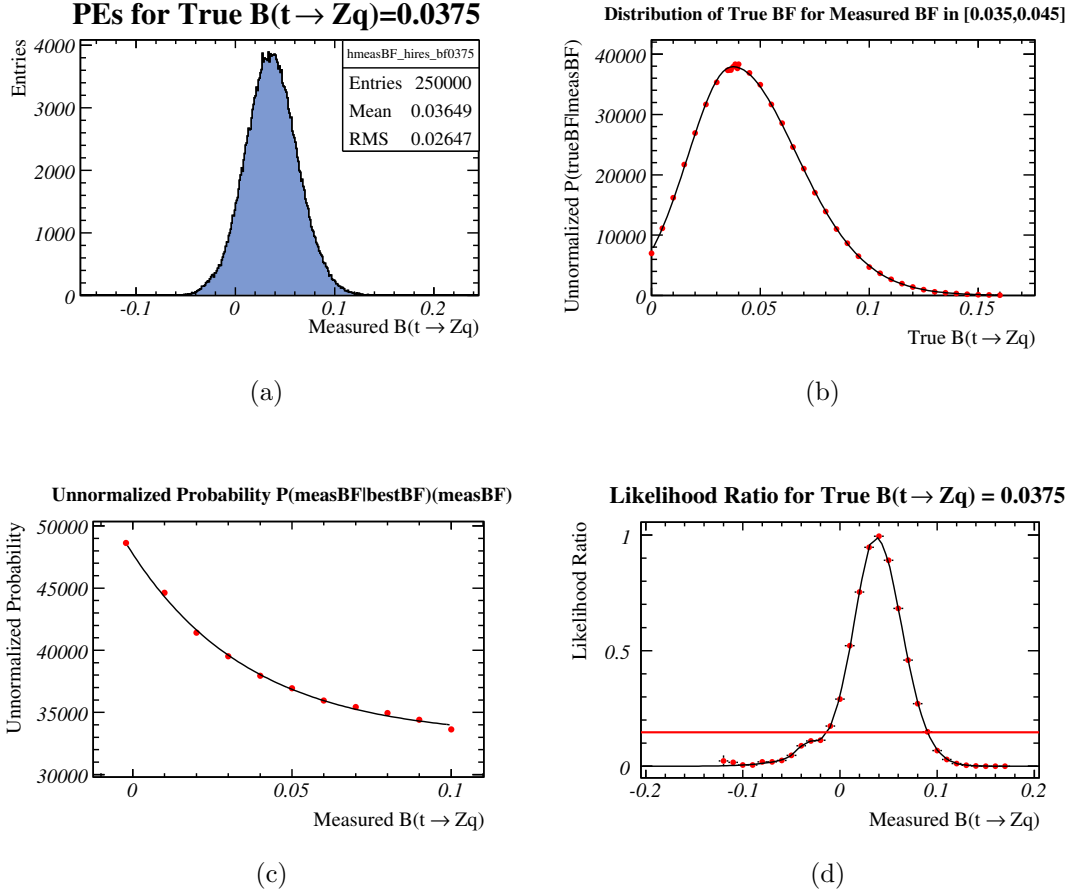


Figure 7.4: Illustration of Feldman-Cousins construction. (a) Unnormalized $\mathcal{P}(\mathcal{B}_{\text{meas}}|\mathcal{B}_{\text{true}})$ for $\mathcal{B}_{\text{true}} = 3.75\%$. (b) Unnormalized $\mathcal{P}(\mathcal{B}_{\text{true}}|\mathcal{B}_{\text{meas}})$ for $\mathcal{B}_{\text{meas}}$ in the range of 3.5% to 4.5%. (c) Unnormalized $\mathcal{P}(\mathcal{B}_{\text{meas}}|\mathcal{B}_{\text{best}})(\mathcal{B}_{\text{meas}})$. (d) Likelihood ratio $\mathcal{R}(\mathcal{B}_{\text{meas}}|\mathcal{B}_{\text{true}})$ for $\mathcal{B}_{\text{true}} = 3.75\%$. 95% of all pseudo-experiments generated at $\mathcal{B}_{\text{true}} = 3.75\%$ have likelihood ratios above the horizontal line.

7.2.4 The Expected Limit Calculation

Using the Feldman-Cousins framework, an expected limit in the absence of signal can be constructed by convoluting the Feldman-Cousins bands with the set of pseudo-experiments for a $\mathcal{B}_{\text{true}} = 0$. For each interval in $\mathcal{B}_{\text{true}}$, the corresponding interval of $\mathcal{B}_{\text{meas}}$ is extracted from the Feldman-Cousins band. The mean and width of the resulting distribution of $\mathcal{B}_{\text{true}}$ constitute the expected limit and its uncertainty, see Fig. 7.5 (b). As shown, the expected upper limit on $\mathcal{B}(t \rightarrow Zq)$ at 95% C.L. is $(5.0 \pm 2.2)\%$.

(b)

Figure 7.5: (a) The Feldman-Cousins band, generated from pseudo-experiments for true branching fractions from 0%–16%. (b) The expected 95% C.L. upper limit on the branching fraction $\mathcal{B}(t \rightarrow Zq)$.

Chapter 8

Result and Conclusions

8.1 Result: An Upper Limit on $\mathcal{B}(t \rightarrow Zq)$

This thesis has fit 1.9 fb^{-1} of CDF data with a customized binned maximum likelihood fitter to determine an upper limit on the branching fraction, $\mathcal{B}(t \rightarrow Zq)$. Using the same fitter for both the pseudo-experiments and the Feldman-Cousins framework, the best fit to the data is shown in Figure. 8.1 (a). The fitted value for the branching fraction is $\mathcal{B}(t \rightarrow Zq) = -1.49\%$. The full list of fit parameters is given in Table 8.1. Using the Feldman-Cousins limit calculation framework, the calculated branching fraction is converted into the upper limit with 95% confidence of $\mathcal{B}(t \rightarrow Zq) < 3.7\%$, as shown in Fig 8.1 (b), agreeing well with the expected limit in absence of a signal of $(5.0 \pm 2.2)\%$.

In summary, this thesis provided the world's best limit on the branching fraction $\mathcal{B}(t \rightarrow Zq) < 3.7\%$ at 95% C.L. in a direct search for the flavor changing neutral current decay of the top quark $t \rightarrow Zq$ in events with a Z boson and four or more jets. In 1.9 fb^{-1} of CDF Run II data, no evidence was found for the decay $t \rightarrow Zq$. This result will spark interest for continuing this work at the LHC to probe the

Table 8.1: Parameters of best fit to the data. The central value of \mathcal{R}_{sig} can be derived from $\sigma_{\mathcal{R}_{\text{sig}}}$ and σ_{JES} : $\mathcal{R}_{\text{sig}} = 52.2\%$. Together with the tagging fraction, f_{tag} , the number of Z +jets events in the tagged and anti-tagged signal regions can be obtained: $Z_{\text{tagged}} = 13.5$ and $Z_{\text{anti}} = 53.9$.

Fit Parameter	Value		
Branching Fraction, $\mathcal{B}(t \rightarrow Zq)$ (%)	-1.49	\pm	1.52
Z +Jets Events in Control Region, Z_{control}	129.0	\pm	11.1
Shift in Ratio Control/Signal Region, $\sigma_{\mathcal{R}_{\text{sig}}}$	-0.61	\pm	0.60
Tagging Fraction, f_{tag} (%)	20.0	\pm	5.9
Jet Energy Scale Shift, σ_{JES}	-0.74	\pm	0.43

limits of top FCNCs in the standard model and beyond.

(b)

Figure 8.1: (a) Mass χ^2 distribution for the best fit to the data. The data points are shown together with the fitted background shape and the fit uncertainty. The expected signal from $t \rightarrow Zq$ decays at the observed 95% C.L. limit of 3.7%. The fit parameters are given in Table 8.1. (b) The Feldman-Cousins band with the measured branching fraction $\mathcal{B}(t \rightarrow Zq)$. The Feldman-Cousins band is refined with 0.1% steps between $\mathcal{B}_{\text{true}} = 3.55\%$ and $\mathcal{B}_{\text{true}} = 3.95\%$. The measured value of $\mathcal{B}(t \rightarrow Zq) = -1.49\%$ corresponds to a limit of 3.7% at 95% C.L.

8.2 Implications for Future Work

This thesis used only the standard model allowed decays to look for evidence of flavor changing neutral currents of the top quark. Although there do exist many beyond the standard model (BSM) models to help explain higher branching fractions for $\mathcal{B}(t \rightarrow Zq)$, such as two-Higgs-doublet and Supersymmetric (SUSY) models, this thesis has not ruled out any such models. With an extended data sample from CDF, it is expected that the upper limit scales as the inverse of the square root of the integrated luminosity. Using this formulation, with predicted integrated luminosity of 8 fb^{-1} by the end of operations in 2010, the limits for the $\mathcal{B}(t \rightarrow Zq)$ are on the order of 1%.

Limitations on luminosity become a moot point for the experiments at the Large Hadron Collider (LHC) as the integrated luminosities are expected to climb to hundreds of inverse femtobarns. At 100 fb^{-1} , tens of millions of $t\bar{t}$ pairs are produced per year. For the ATLAS experiment using Monte Carlo simulations, combining results for leptonic and hadronic decay modes could yield a branching fraction for $t \rightarrow Zq$ as low as 1.8×10^{-4} [21] with 100 fb^{-1} . With such sensitivity, BSM models can be tested in hopes to unveil new physics. Figure 8.2 shows the relative sensitivities of top's FCNC decay throughout the experiments conducted to date with the expected sensitivity added by the ATLAS experiment at the LHC [22].

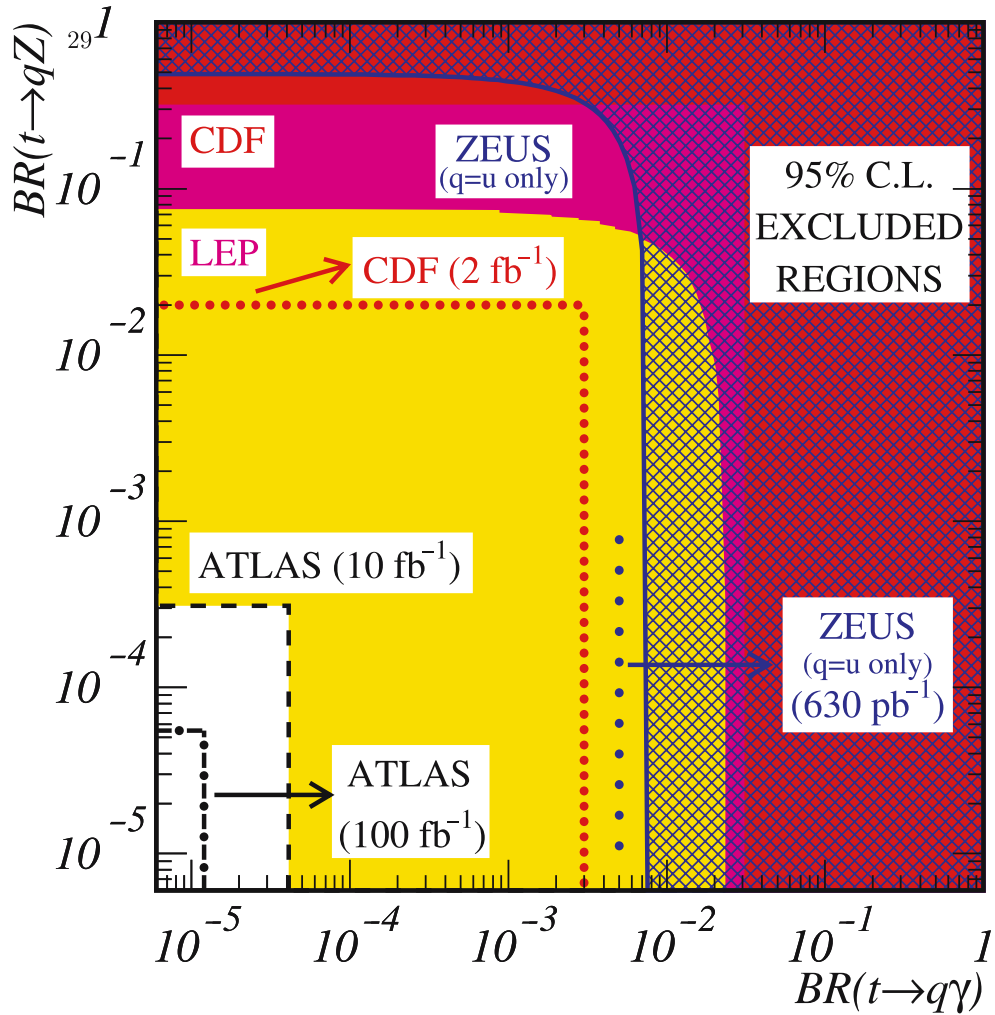


Figure 8.2: Shown are the 95% C.L. limits on tops FCNC decays to date [22]. With upwards of hundreds of inverse femtobarns of data at the ATLAS experiment at the LHC, the regions excluded at 95% C.L. will grow tremendously. Shown are the CDF Run-II “expected” sensitivity, as the results for this thesis were not included in this study.

Bibliography

- [1] H. Fritzsch, *t-Quarks May Decay into Z-Bosons and Charm*, Phys. Lett. **B224** (1989), 423.
- [2] J. A. Aguilar-Saavedra, *Top flavour-changing neutral interactions: Theoretical expectations and experimental detection*, Acta Phys. Polon. **B35** (2004), 2695–2710, hep-ph/0409342.
- [3] T. Inami and C. S. Lim, *Effects of Superheavy Quarks and Leptons in Low-Energy Weak Processes $K_L \rightarrow \mu^+\mu^-$, $K^+ \rightarrow \pi^+\nu\bar{\nu}$ and $K^0 \leftrightarrow \bar{K}^0$* , Prog. Theor. Phys. **65** (1981), 297.
- [4] F. Abe et al. (CDF Collaboration), *Search for Flavor-Changing Neutral Current Decays of the Top Quark in $p\bar{p}$ Collisions at $\sqrt{s} = 1.8$ TeV*, Phys. Rev. Lett. **80** (1998), 2525–2530.
- [5] P. Achard et al. (L3 Collaboration), *Search for Single Top Production at LEP*, Phys. Lett. **B549** (2002), 290–300, hep-ex/0210041.
- [6] C. Gattuso et al., *Accelerator Concepts, Fermilab Accelerator Division Documentation*, http://www-bdnew.fnal.gov/_operations_/rookie-books_/Concepts.v3.1.pdf (retrieved: May 18, 2008).

- [7] P. T. Lukens (CDF IIb Collaboration), *The CDF IIb detector: Technical design report*, FERMILAB-TM-2198.
- [8] D. Acosta et al., *The performance of the CDF luminosity monitor*, Nucl. Instrum. Meth. **A494** (2002), 57–62.
- [9] CDF Collaboration, *Cross-Section with Displaced Vertex Web Page*, http://www-cdf.fnal.gov/physics/new/top/2006/xs_ljetsvx/public.html (retrieved: November 9, 2007).
- [10] S. Eidelman et al. (Particle Data Group Collaboration), *Review of particle physics*, Phys. Lett. **B592** (2004), 1.
- [11] *Top Group Winter 2008 Luminosity*, http://www-cdf.fnal.gov/internal/physics/top/RunIITopProp/gen6Sum06/lumi_v18.html (retrieved: November 9, 2007).
- [12] CDF Collaboration, *Good Run List v18*, <http://www-cdf.fnal.gov/internal/dqm/goodrun/good.html> (retrieved: November 9, 2007).
- [13] T. Sjöstrand, L. Lönnblad, and S. Mrenna, *PYTHIA 6.2: Physics and manual*, (2001), hep-ph/0108264.
- [14] J. M. Campbell and R. K. Ellis, *An update on vector boson pair production at hadron colliders*, Phys. Rev. **D60** (1999), 113006.
- [15] S. Baker and R. Cousins, *Clarification of the Use of χ^2 and Likelihood Functions in Fits to Histograms*, Nucl. Instrum. Meth. **A221** (1984), 437–442.
- [16] F. James and M. Roos, *Minuit: A System for Function Minimization and Analysis of the Parameter Errors and Correlations*, Comput. Phys. Commun. **10** (1975), 343–367.

- [17] G. Feldman and R. Cousins, *Unified approach to the classical statistical analysis of small signals*, Phys. Rev. D **57(7)** (1998), 3873–3889.
- [18] G. J. Feldman and R. D. Cousins, *A Unified approach to the classical statistical analysis of small signals*, Phys. Rev. **D57** (1998), 3873–3889, physics/9711021.
- [19] A. L. Read, *Linear interpolation of histograms*, Nucl. Instrum. Meth. **A425** (1999), 357–360.
- [20] T. R. Junk, *Including Systematic Uncertainties in Computing p-Values and Limits with mclimit_csm.C*, Talk given at CDF Top Meeting, June 28, 2007, http://www-cdf.fnal.gov/internal/WebTalks/Archive/0706/070628_top/ (retrieved: January 6, 2008).
- [21] L. Chikovani and T. Djobava, *ATLAS Sensitivity to the Flavour-Changing Neutral Current Decay $t \rightarrow Zq\bar{s}$* , 2002, <http://www.citebase.org/abstract?id=oai:arXiv.org:hep-ex/0205016>.
- [22] J. Carvalho, N. Castro, L. Chikovani, T. Djobava, J. Dodd, S. McGrath, A. Onofre, J. Parsons, and F. Veloso, *Study of ATLAS sensitivity to FCNC top decays*, European Physical Journal C **52** (2007), 999.

Appendix A

Control Plots

Contained in this appendix are a medley of control plots validating the Monte Carlo simulations used with the datasets.

In each plot, the background contributions from SM $t\bar{t}$ and diboson production are normalized according to the expected number of events in 1.9 fb^{-1} , seen in Table 5.6.

In Section A.1, jet multiplicity plots are shown. The Z +jets samples are added such that the total background is normalized to the 0-jet bin before b -tagging.

In Section A.2, kinematic distributions for each important variable in this thesis are shown. All kinematic distributions are $N - 1$ distributions, meaning that all selection cuts are applied except for the kinematic variable shown. Sections A.3 and A.4 show these same kinematic variables, but with shifted jet energy scales applied. The Z +jets backgrounds in the kinematic variable plots are added such that the total background is normalized to the data event yield.

A.1 Jet Multiplicity

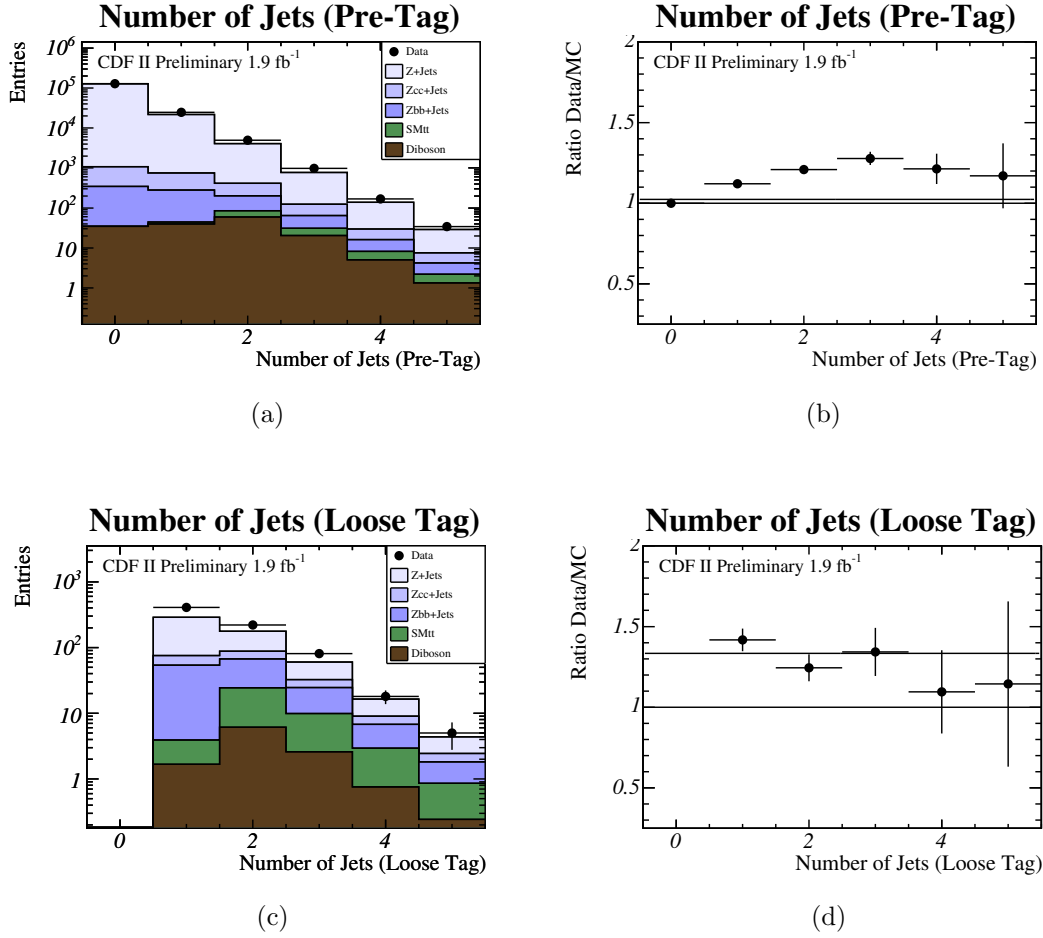


Figure A.1: Data-Monte Carlo comparisons of the number of jets in events with a reconstructed Z . (a) Distribution of the number of jets before b -tagging. (b) Ratio of data over Monte Carlo before b -tagging. (c) Distribution of the number of jets after b -tagging. (d) Ratio of data over Monte Carlo after b -tagging.

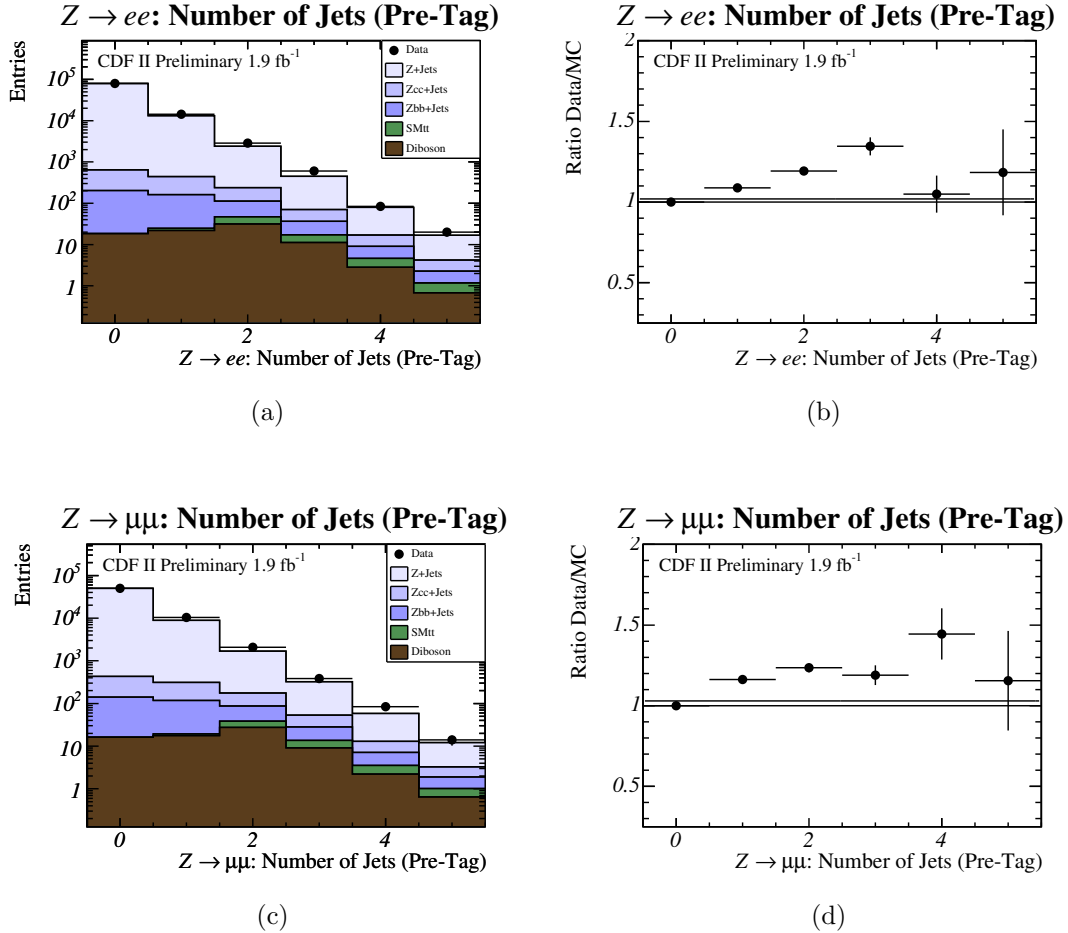


Figure A.2: Data-Monte Carlo comparisons of the number of jets in events with a reconstructed Z before b -tagging. (a) Distribution of the number of jets for $Z \rightarrow e^+e^-$ only. (b) Ratio of data over MC for $Z \rightarrow e^+e^-$. (c) Distribution of the number of jets for $Z \rightarrow \mu^+\mu^-$ only. (d) Ratio of data over Monte Carlo for $Z \rightarrow \mu^+\mu^-$.

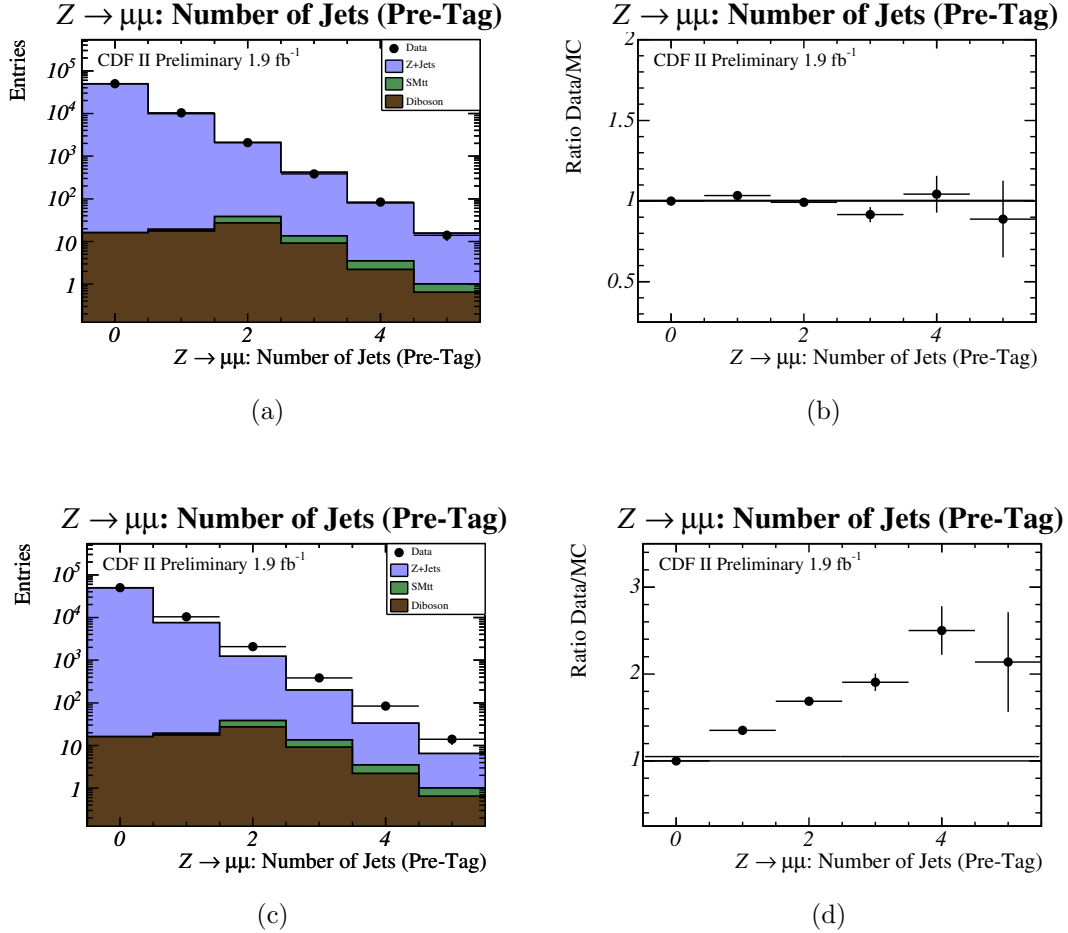


Figure A.3: Data-Monte Carlo comparisons of the number of jets in events with a reconstructed $Z \rightarrow \mu^+\mu^-$ for systematic ALPGEN samples, see Section 6.4.2. (a) Distribution of the number of jets for $qfac = ktfac = 0.5$. (b) Ratio of data over Monte Carlo for $qfac = ktfac = 0.5$. (c) Distribution of the number of jets for $qfac = ktfac = 2.0$. (d) Ratio of data over Monte Carlo for $qfac = ktfac = 2.0$.

A.2 Kinematic Distributions

A.2.1 The Mass $\sqrt{\chi^2}$ Distribution

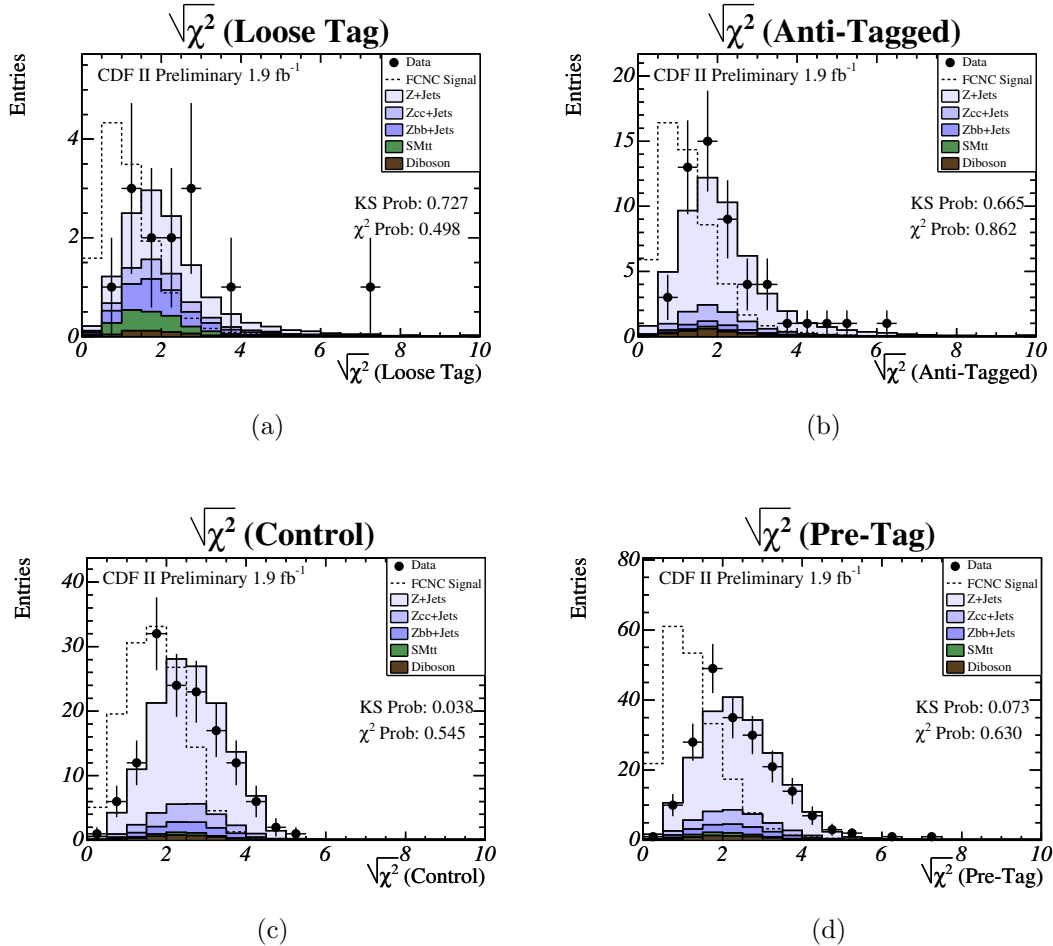


Figure A.4: The $\sqrt{\chi^2}$ distribution for the (a) tagged, (b) anti-tagged, (c) control and (d) pre-tagged selections. The expected backgrounds are normalized to the data event yield. The dashed line shows the shape expected from the main FCNC signal, also normalized to the data event yield.

A.2.2 The Transverse Mass Distribution

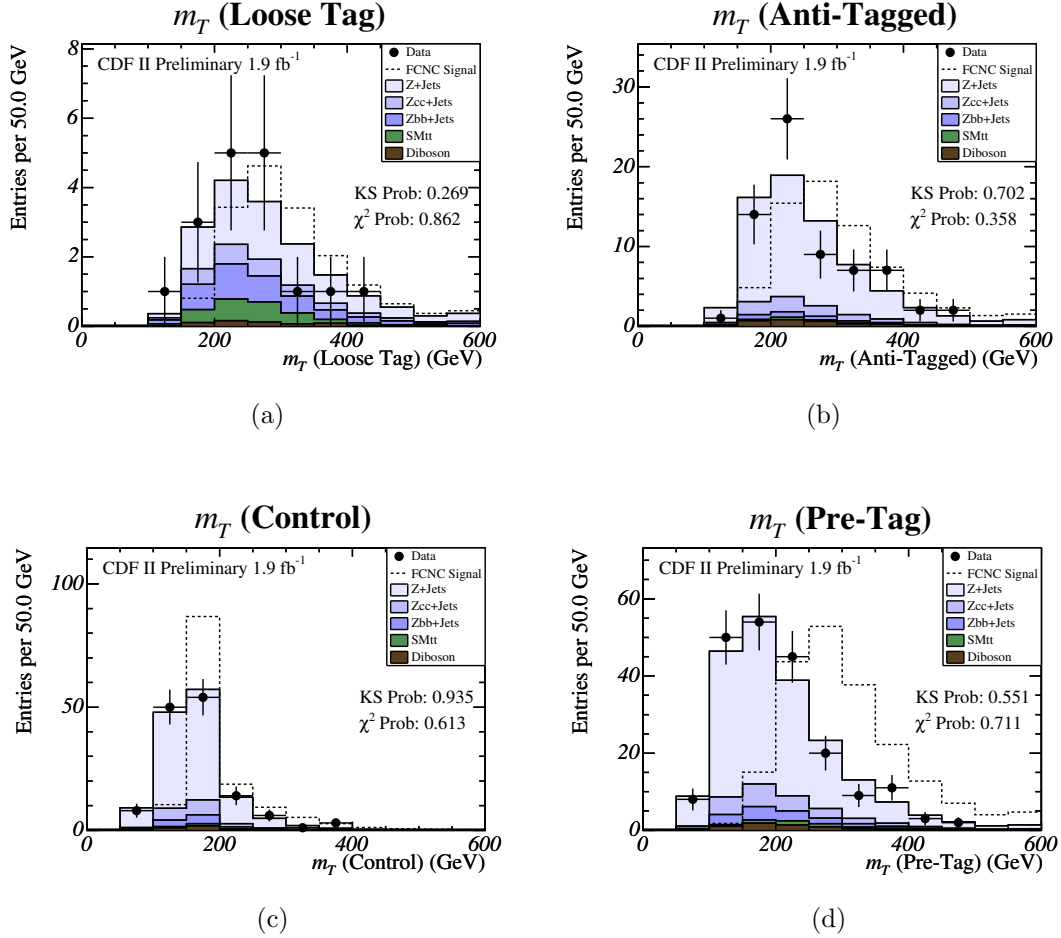


Figure A.5: The transverse mass distribution for the (a) tagged, (b) anti-tagged, (c) control, and (d) pre-tagged selections. The expected backgrounds are normalized to the data event yield. The dashed line shows the shape expected from the main FCNC signal, also normalized to the data event yield.

A.2.3 The Leading Jet E_T Distribution

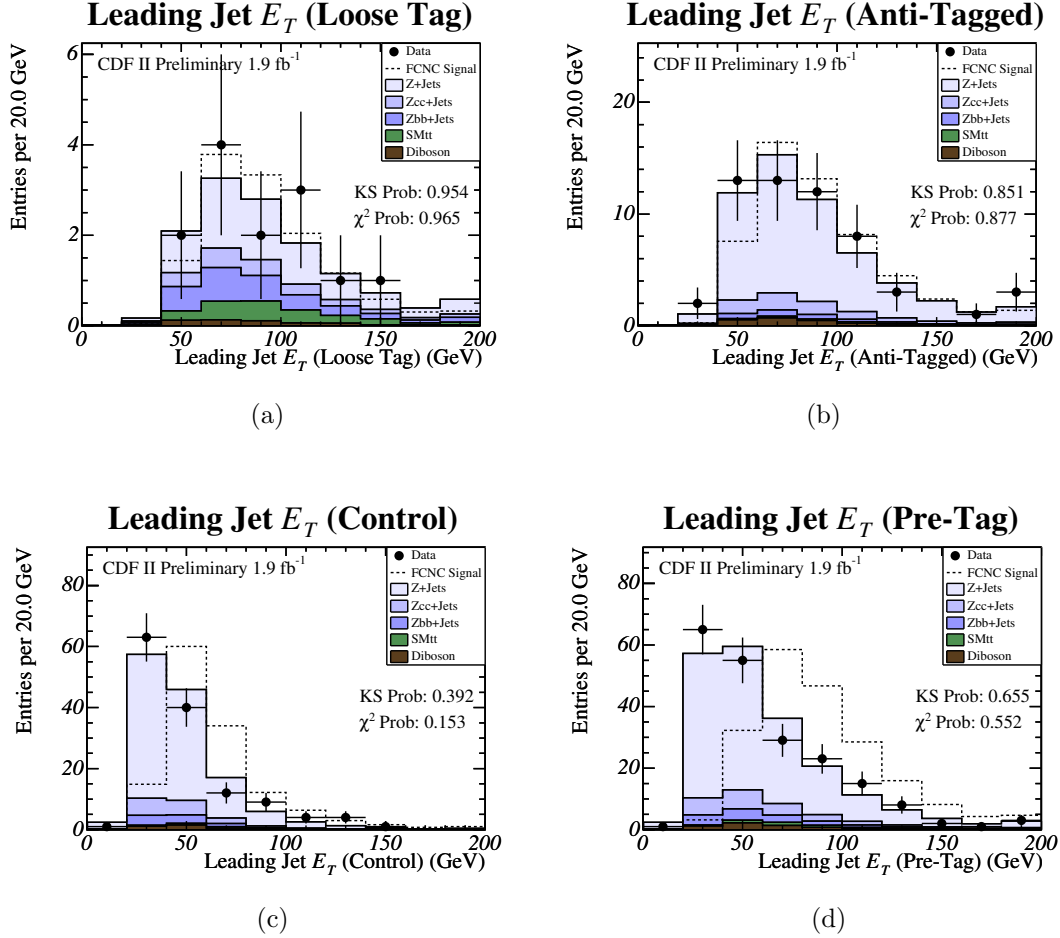


Figure A.6: The transverse energy distribution of the leading jet for the (a) tagged, (b) anti-tagged, (c) control, and (d) pre-tagged selections. The expected backgrounds are normalized to the data event yield. The dashed line shows the shape expected from the main FCNC signal, also normalized to the data event yield.

A.2.4 The Second Jet E_T Distribution

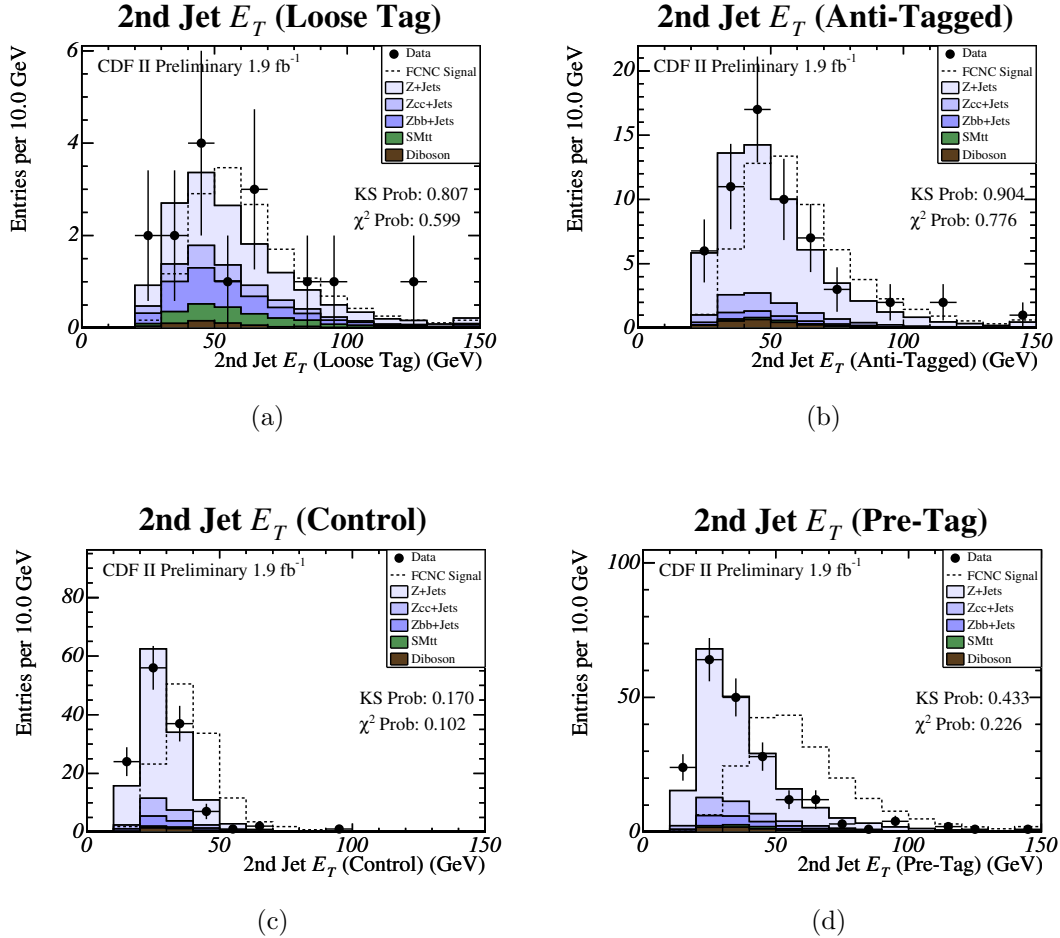


Figure A.7: The transverse energy distribution of the second jet for the (a) tagged, (b) anti-tagged, (c) control, and (d) pre-tagged selections. The expected backgrounds are normalized to the data event yield. The dashed line shows the shape expected from the main FCNC signal, also normalized to the data event yield.

A.2.5 The Third Jet E_T Distribution

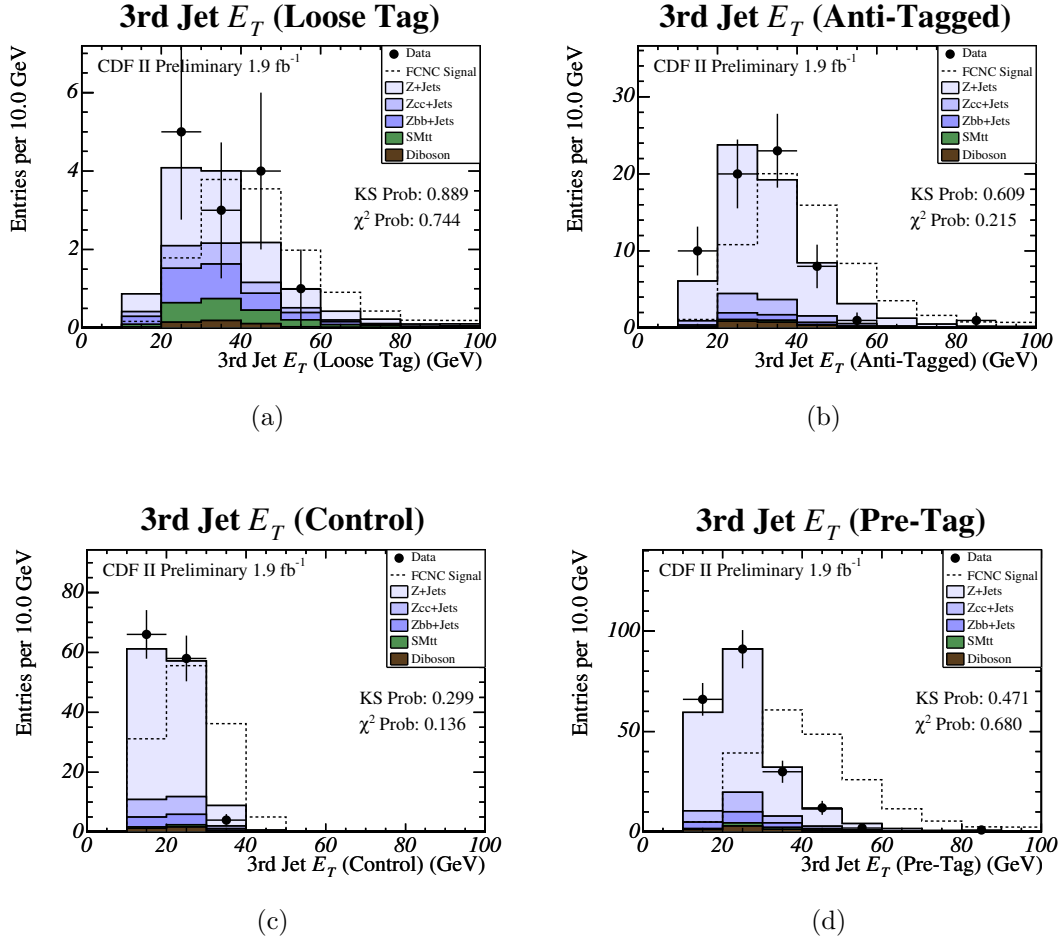


Figure A.8: The transverse energy distribution of the third jet for the (a) tagged, (b) anti-tagged, (c) control, and (d) pre-tagged selections. The expected backgrounds are normalized to the data event yield. The dashed line shows the shape expected from the main FCNC signal, also normalized to the data event yield.

A.2.6 The Fourth Jet E_T Distribution

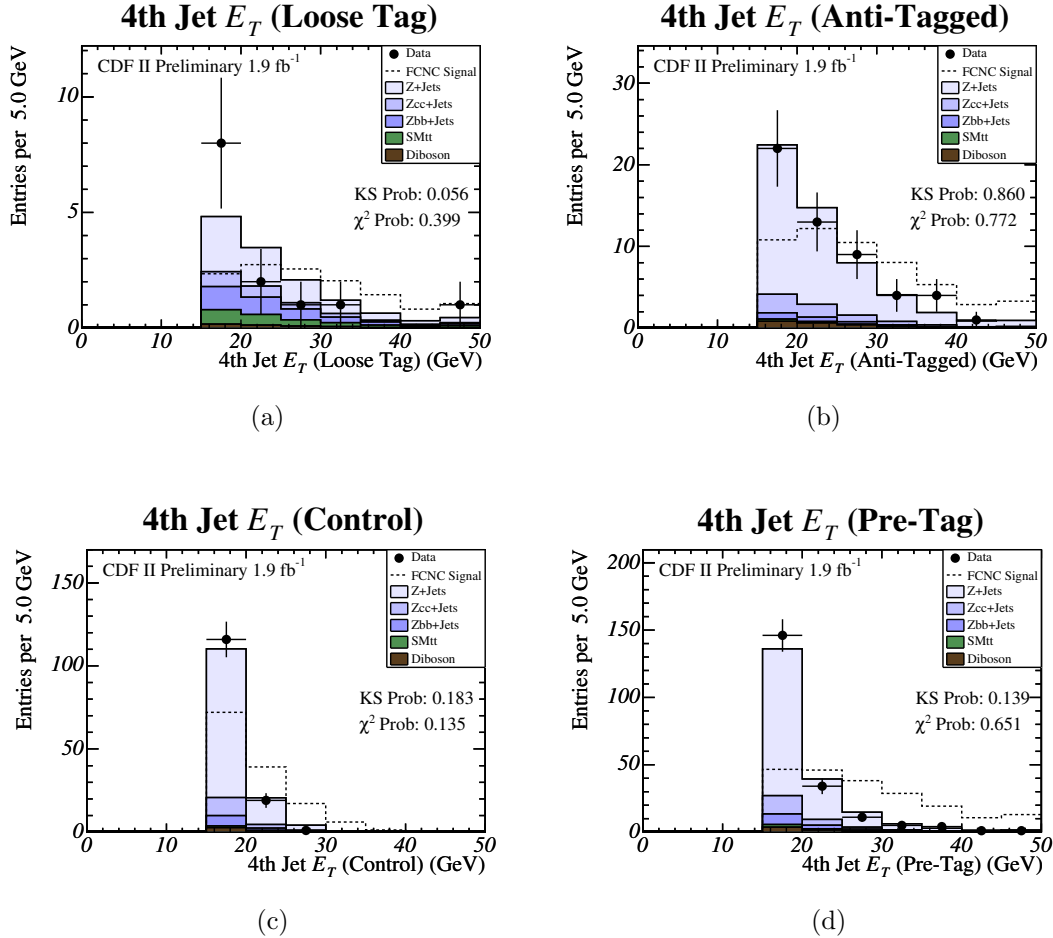


Figure A.9: The transverse energy distribution of the fourth jet for the (a) tagged, (b) anti-tagged, (c) control, and (d) pre-tagged selections. The expected backgrounds are normalized to the data event yield. The dashed line shows the shape expected from the main FCNC signal, also normalized to the data event yield.

A.2.7 The Z Mass Distribution

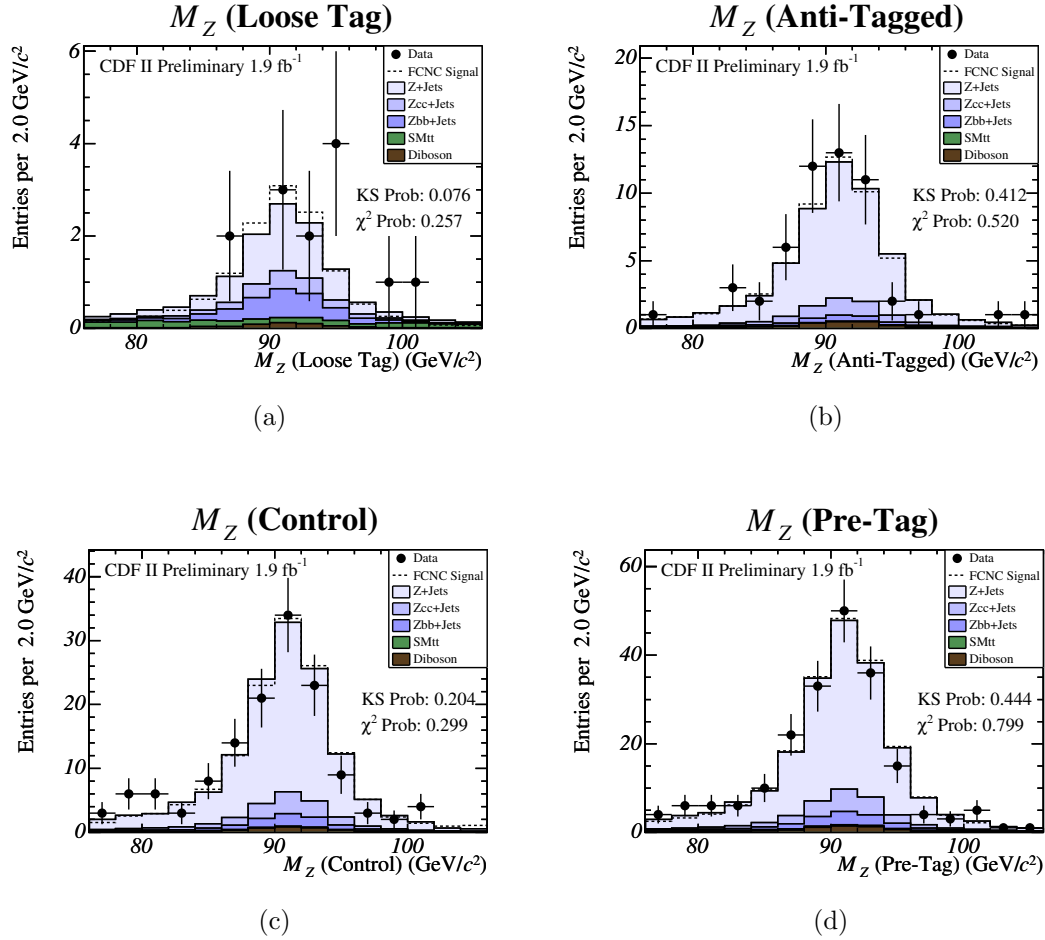


Figure A.10: The Z mass distribution for the (a) tagged, (b) anti-tagged, (c) control, and (d) pre-tagged selections. The expected backgrounds are normalized to the data event yield. The dashed line shows the shape expected from the main FCNC signal, also normalized to the data event yield.

A.2.8 The G_T Distribution

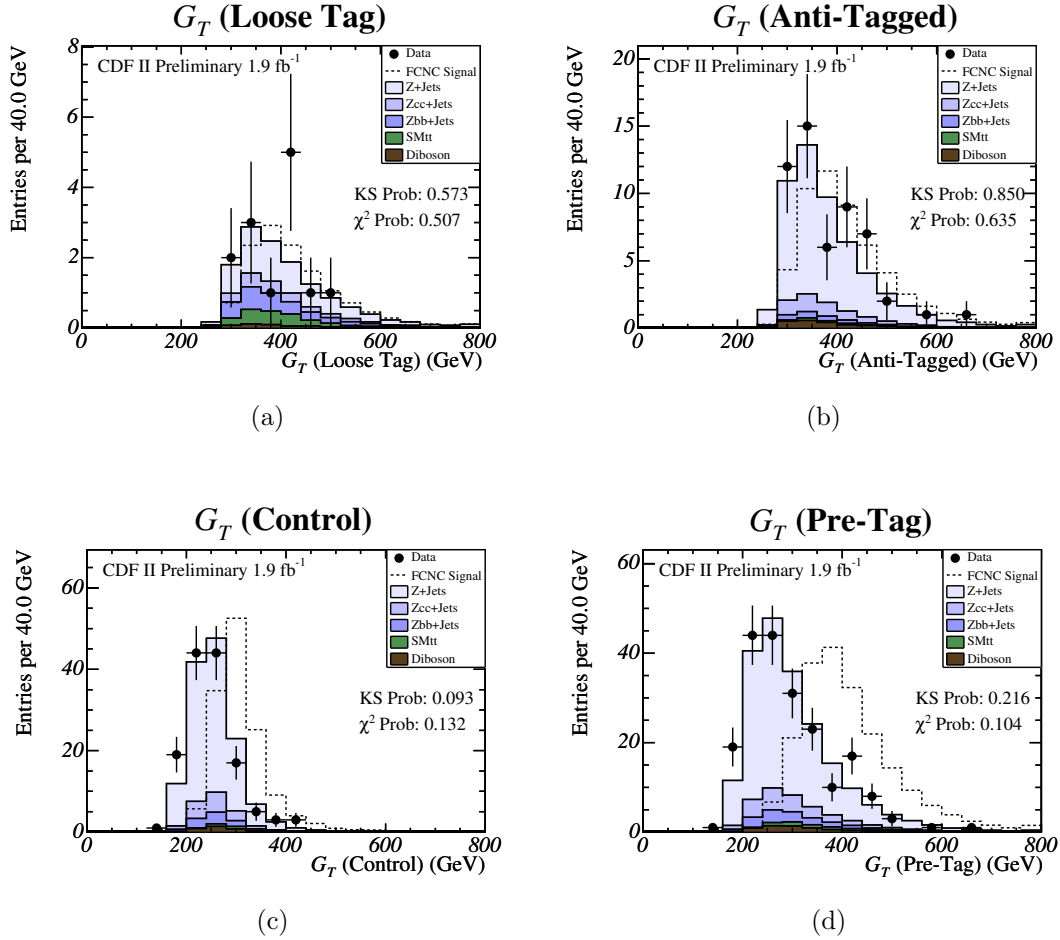


Figure A.11: The G_T distribution for the (a) tagged, (b) anti-tagged, (c) control, and (d) pre-tagged selections. The variable G_T , defined as the scalar sum of the lepton transverse momenta and the jet transverse energies, is not used as a cut in this analysis. The expected backgrounds are normalized to the data event yield. The dashed line shows the shape expected from the main FCNC signal, also normalized to the data event yield.

A.2.9 The Missing Transverse Energy Distribution

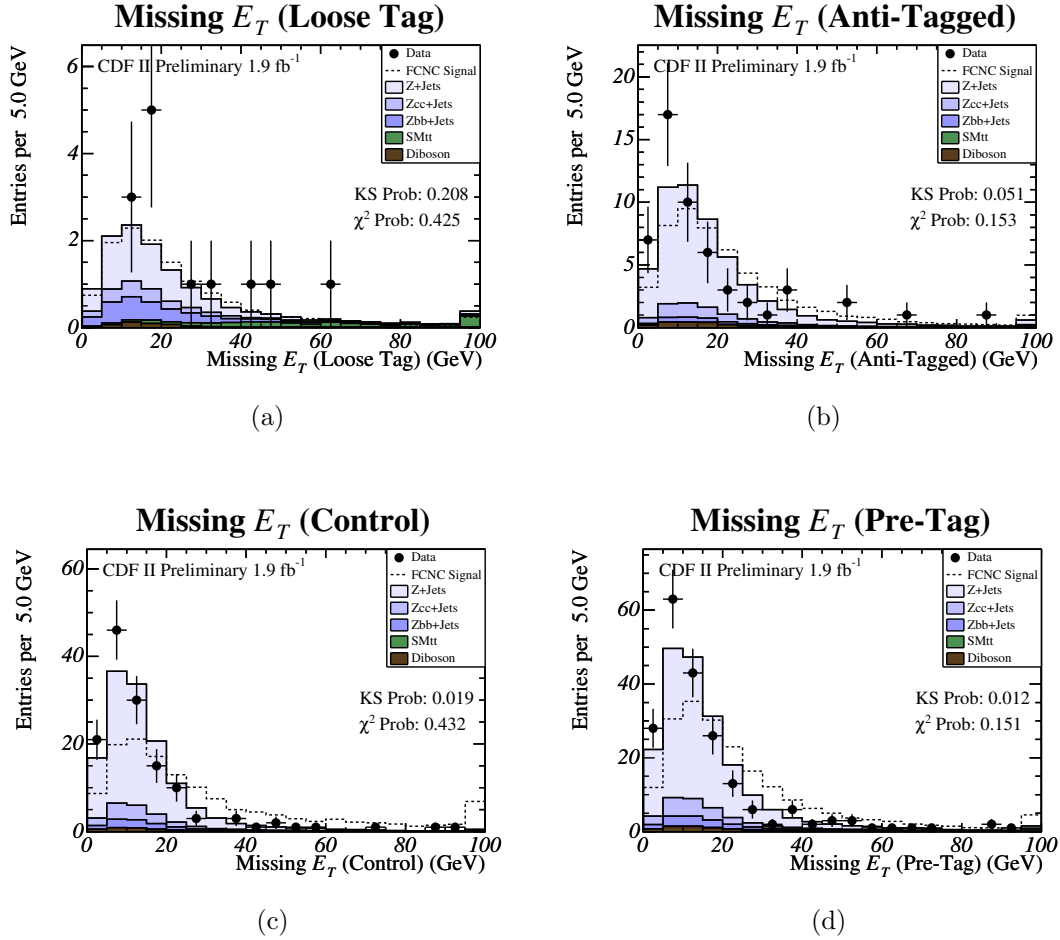


Figure A.12: The missing transverse energy distribution for the (a) tagged, (b) anti-tagged, (c) control, and (d) pre-tagged selections. Missing transverse energy is not used as a cut in this analysis. The expected backgrounds are normalized to the data event yield. The dashed line shows the shape expected from the main FCNC signal, also normalized to the data event yield.

A.3 Kinematic Distributions, JES shift -1σ

A.3.1 The Mass $\sqrt{\chi^2}$ Distribution, JES shift -1σ

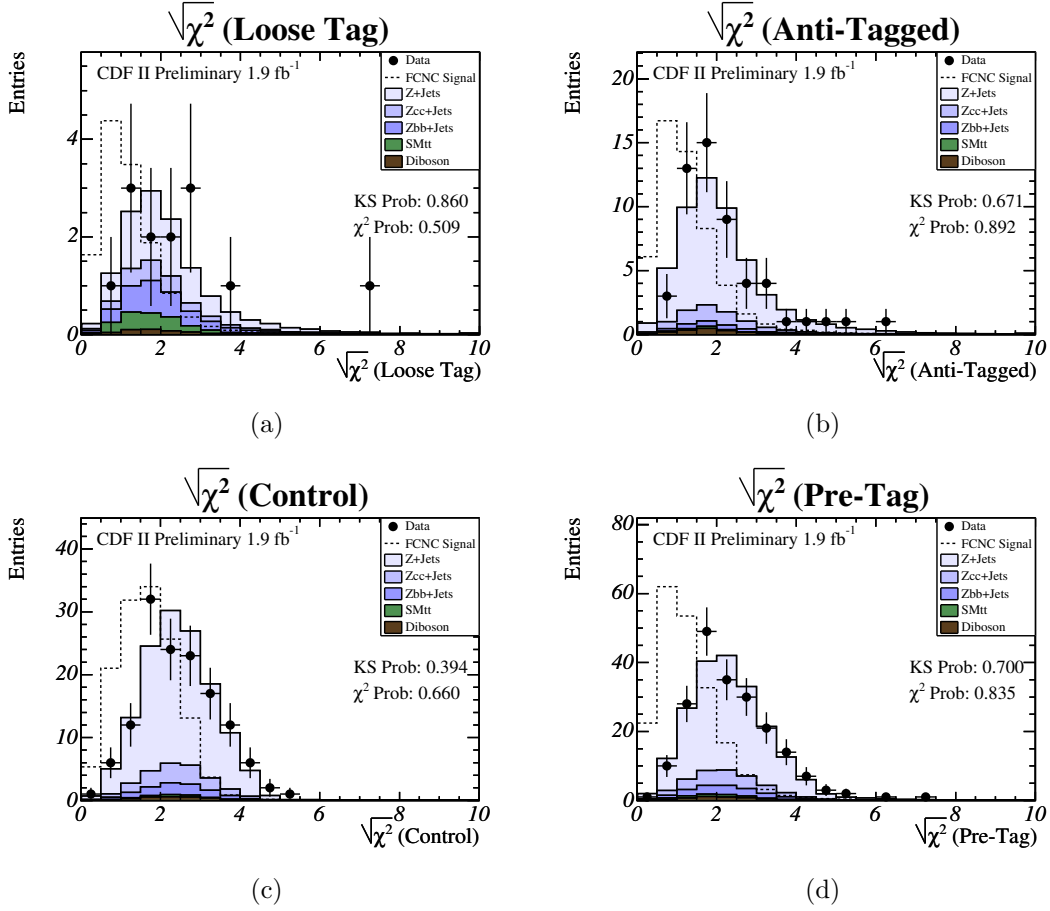


Figure A.13: The $\sqrt{\chi^2}$ distribution with shifted jet energy scale down 1σ for the (a) tagged, (b) anti-tagged, (c) control, and (d) pre-tagged selections. The expected backgrounds are normalized to the data event yield.

A.3.2 The Transverse Mass Distribution, JES shift -1σ

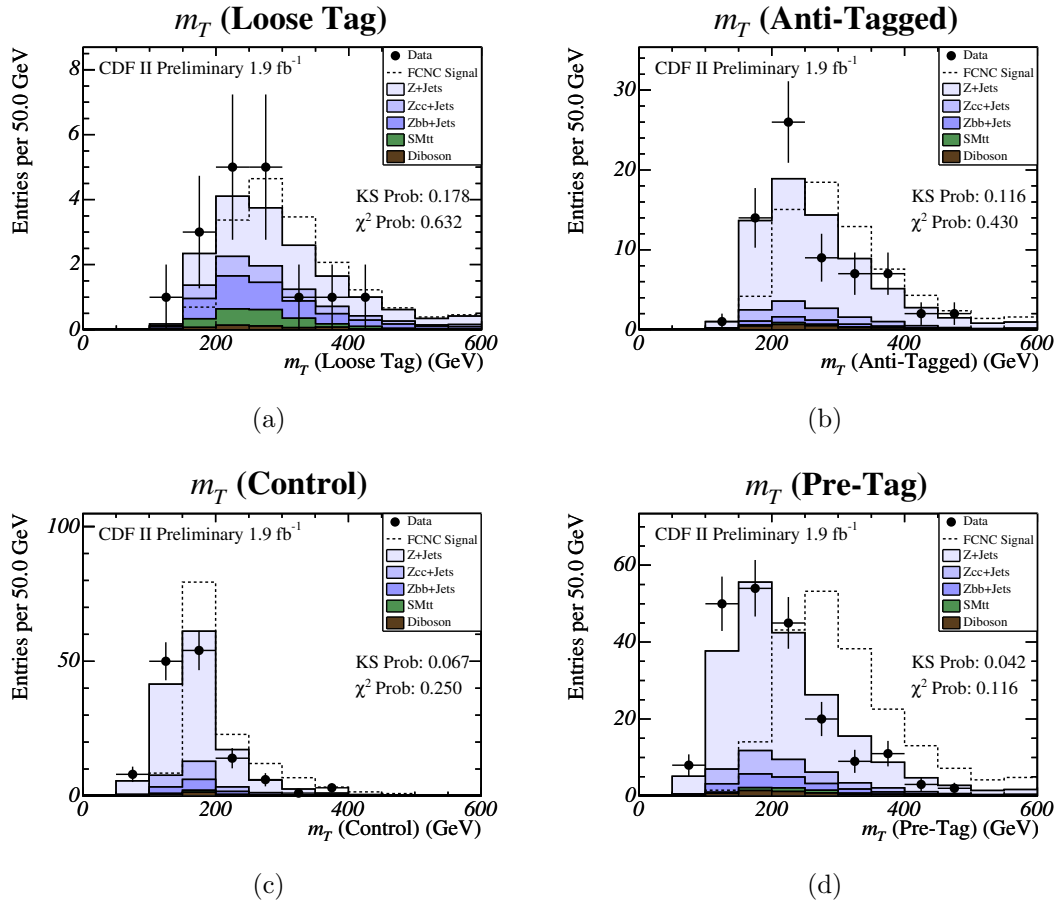


Figure A.14: The transverse mass distribution with shifted jet energy scale down 1σ for the (a) tagged, (b) anti-tagged, (c) control, and (d) pre-tagged selections. The expected backgrounds are normalized to the data event yield.

A.3.3 The Leading Jet E_T Distribution, JES shift -1σ

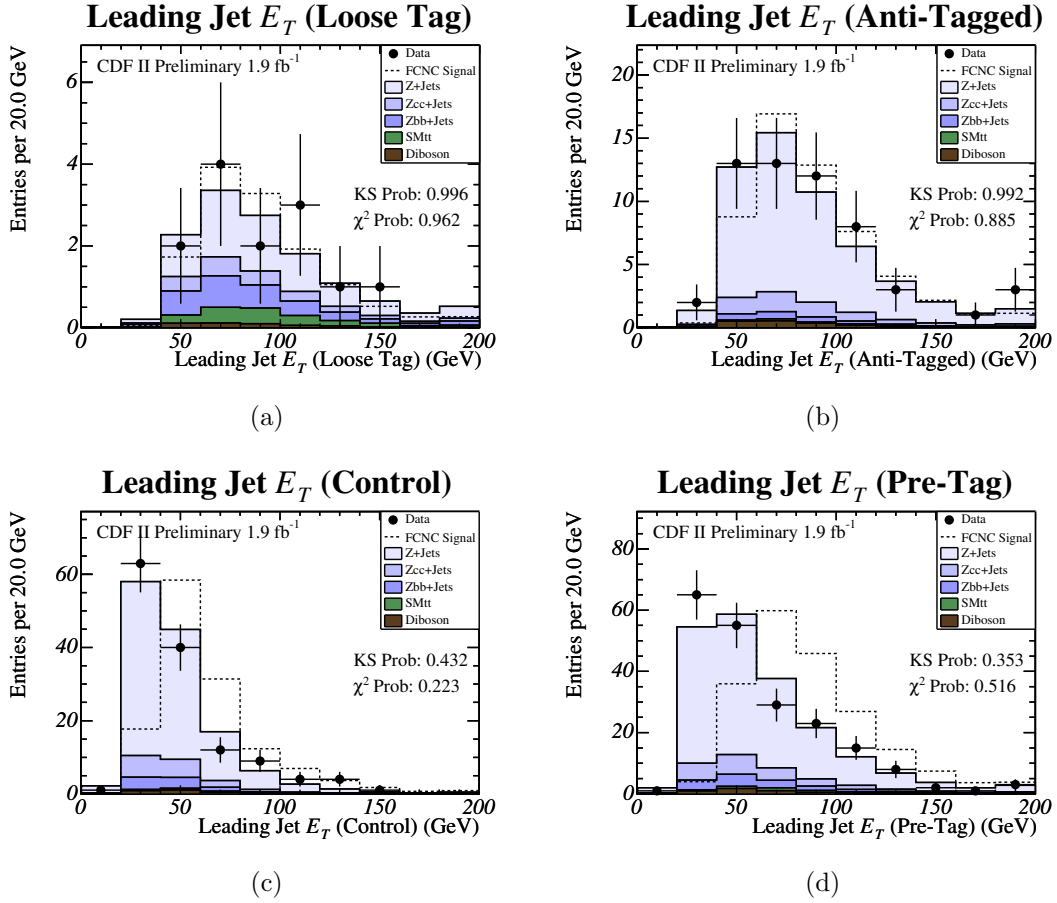


Figure A.15: The transverse energy distribution with shifted jet energy scale down 1σ of the leading jet for the (a) tagged, (b) anti-tagged, (c) control, and (d) pre-tagged selections. The expected backgrounds are normalized to the data event yield.

A.3.4 The Second Jet E_T Distribution, JES shift -1σ

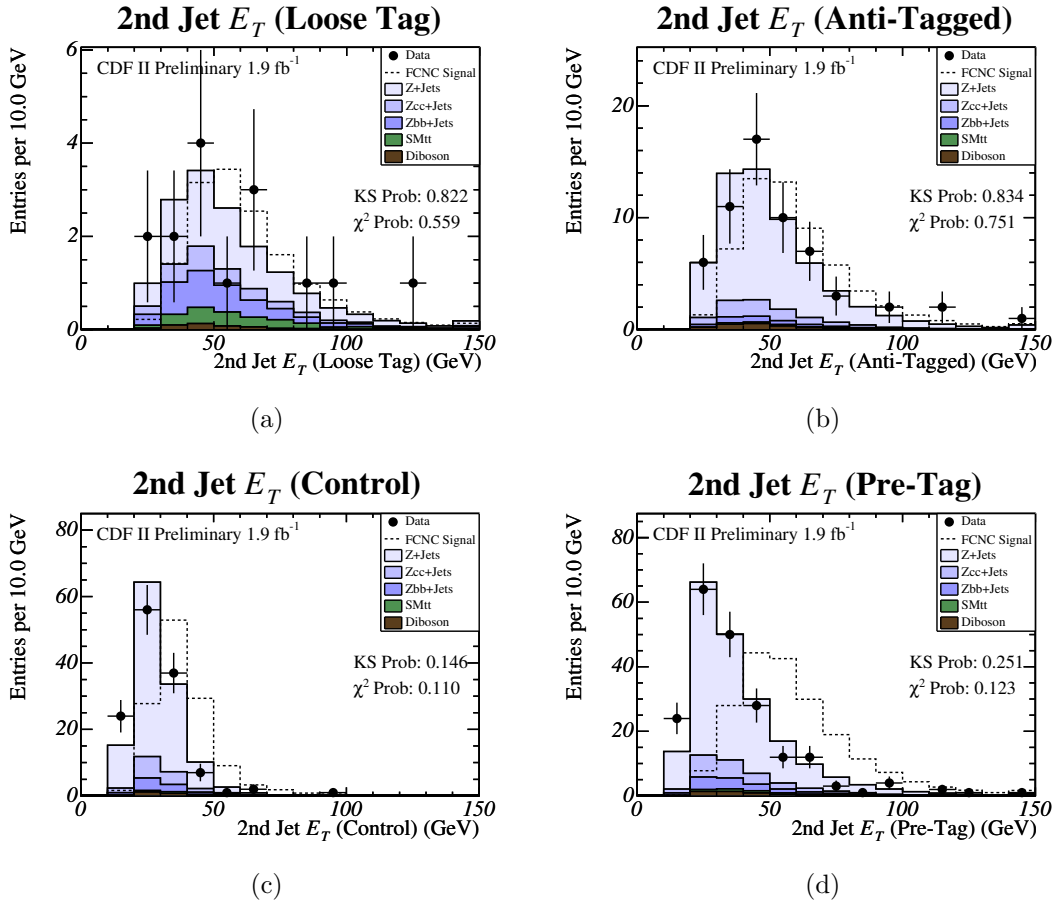


Figure A.16: The transverse energy distribution with shifted jet energy scale down 1σ of the second jet for the (a) tagged, (b) anti-tagged, (c) control, and (d) pre-tagged selections. The expected backgrounds are normalized to the data event yield.

A.3.5 The Third Jet E_T Distribution, JES shift -1σ

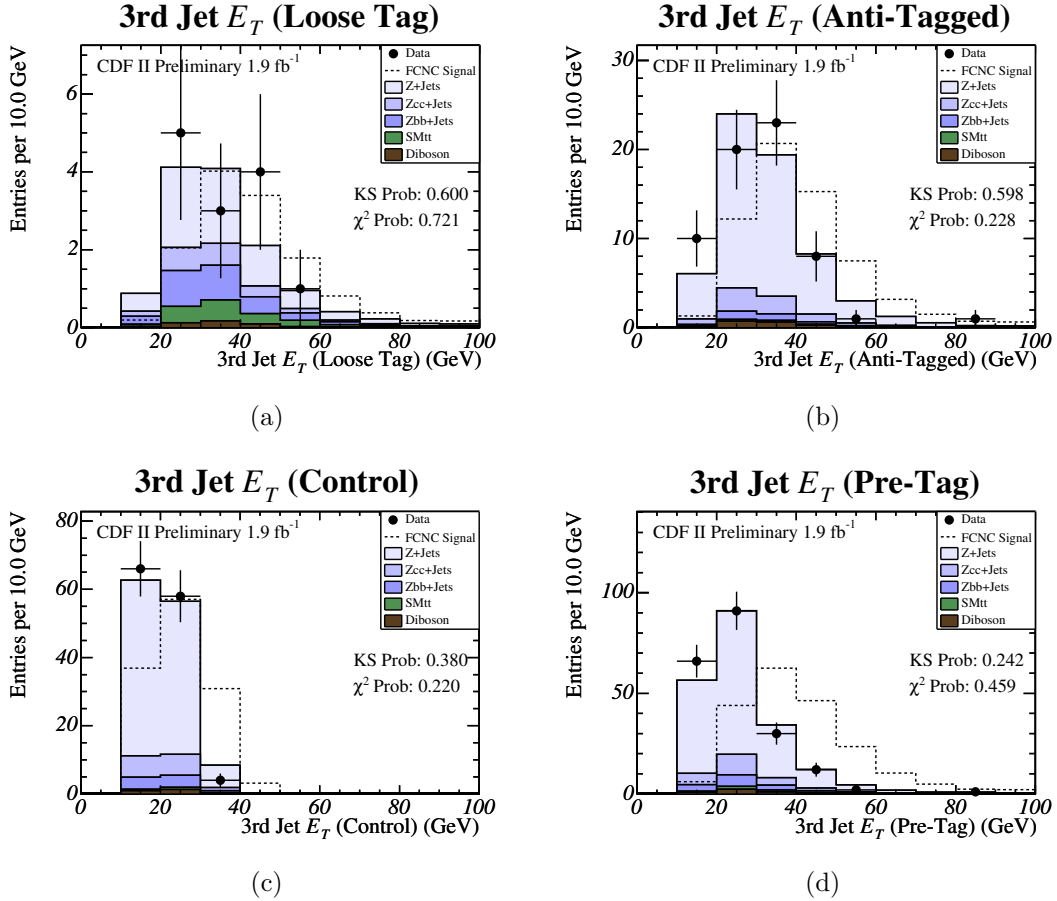


Figure A.17: The transverse energy distribution with shifted jet energy scale down 1σ of the third jet for the (a) tagged, (b) anti-tagged, (c) control, and (d) pre-tagged selections. The expected backgrounds are normalized to the data event yield.

A.3.6 The Fourth Jet E_T Distribution, JES shift -1σ

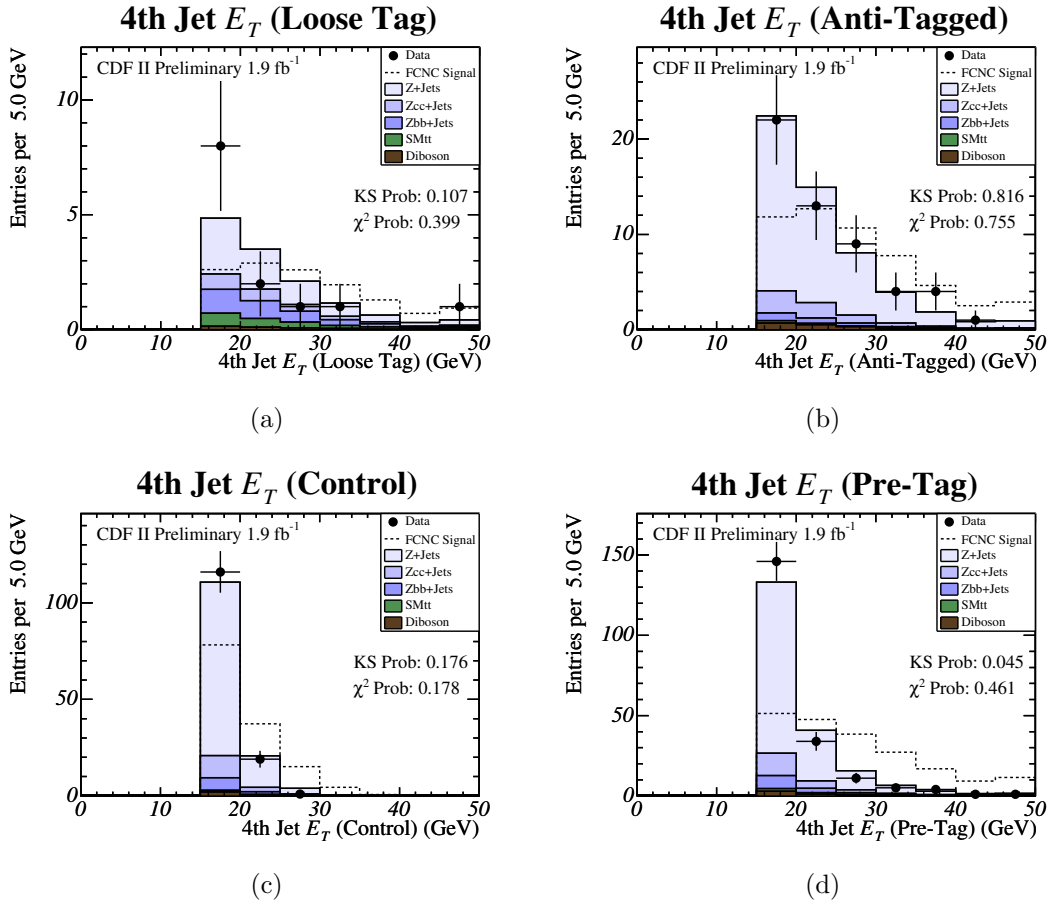


Figure A.18: The transverse energy distribution with shifted jet energy scale down 1σ of the fourth jet for the (a) tagged, (b) anti-tagged, (c) control, and (d) pre-tagged selections. The expected backgrounds are normalized to the data event yield.

A.3.7 The G_T Distribution, JES shift -1σ

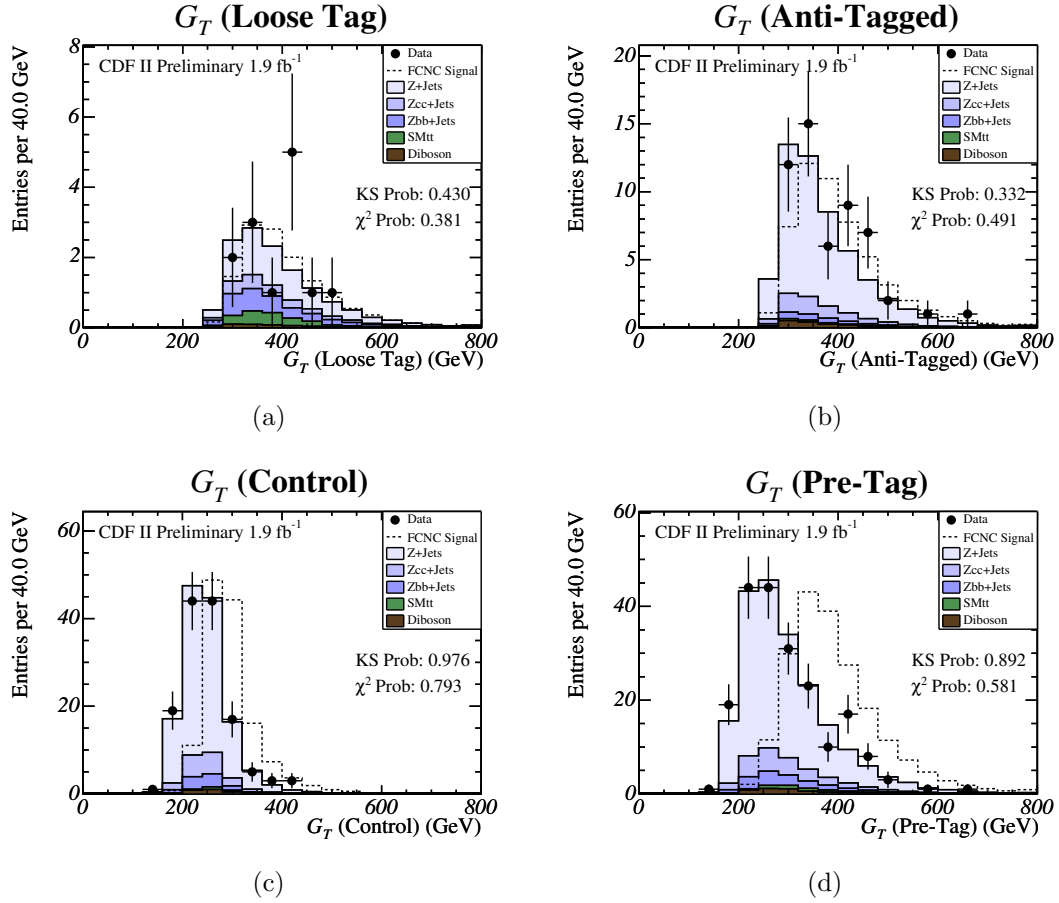


Figure A.19: The G_T distribution with shifted jet energy scale down 1σ for the (a) tagged, (b) anti-tagged, (c) control, and (d) pre-tagged selections. G_T is defined as the scalar sum of the lepton transverse momenta and the jet transverse energies. The expected backgrounds are normalized to the data event yield.

A.3.8 The Missing Transverse Energy Distribution, JES shift -1σ

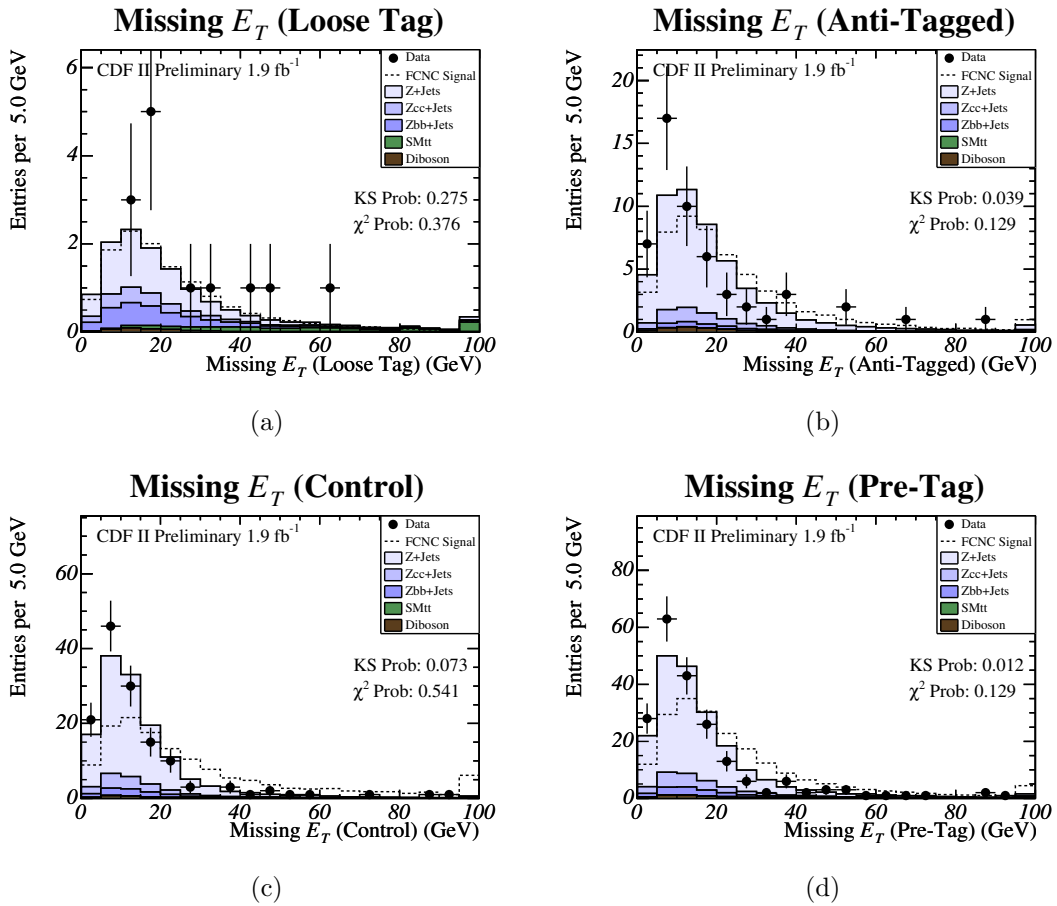


Figure A.20: The missing transverse energy distribution with shifted jet energy scale down 1σ for the (a) tagged, (b) anti-tagged, (c) control, and (d) pre-tagged selections. Missing transverse energy is not used as a cut in this analysis. The expected backgrounds are normalized to the data event yield.

A.3.9 The Z Mass Distribution, JES shift -1σ

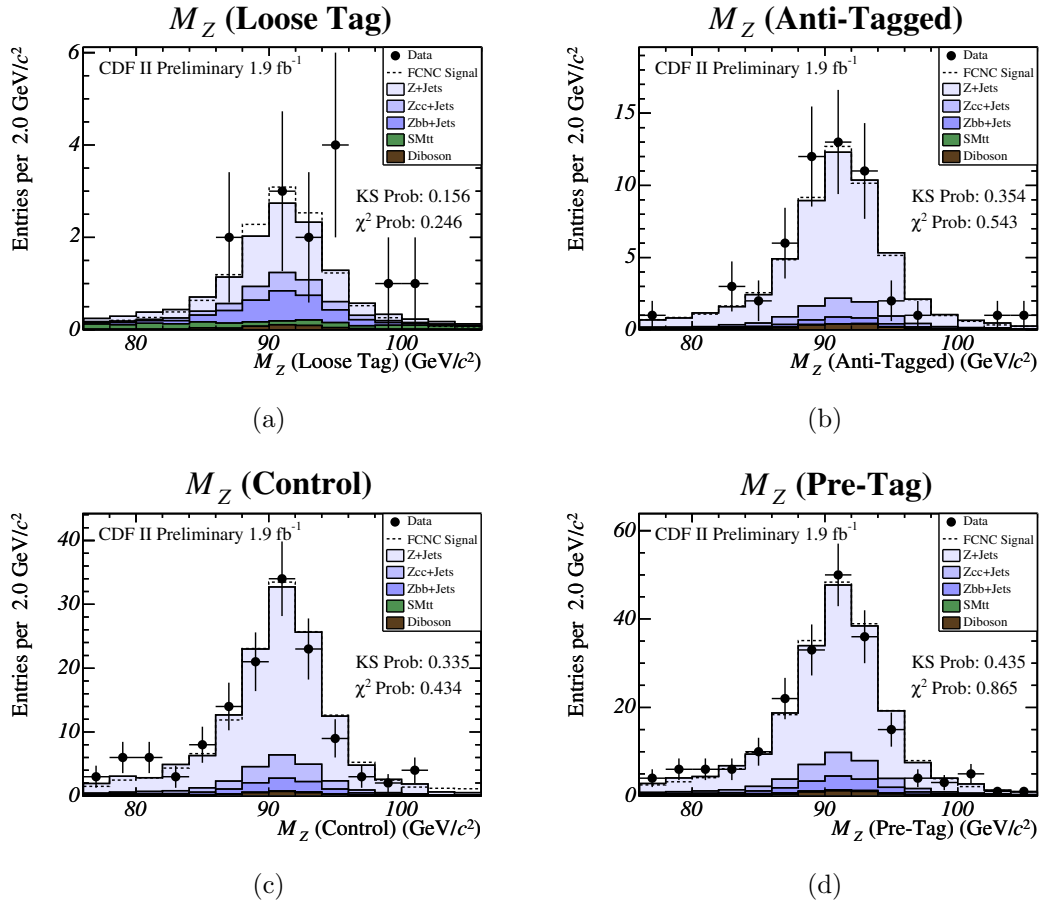


Figure A.21: The Z mass distribution with shifted jet energy scale down 1σ for the (a) tagged, (b) anti-tagged, (c) control and (d) pre-tagged selections. The expected backgrounds are normalized to the data event yield.

A.4 Kinematic Distributions, JES shift $+1\sigma$

A.4.1 The Mass $\sqrt{\chi^2}$ Distribution, JES shift $+1\sigma$

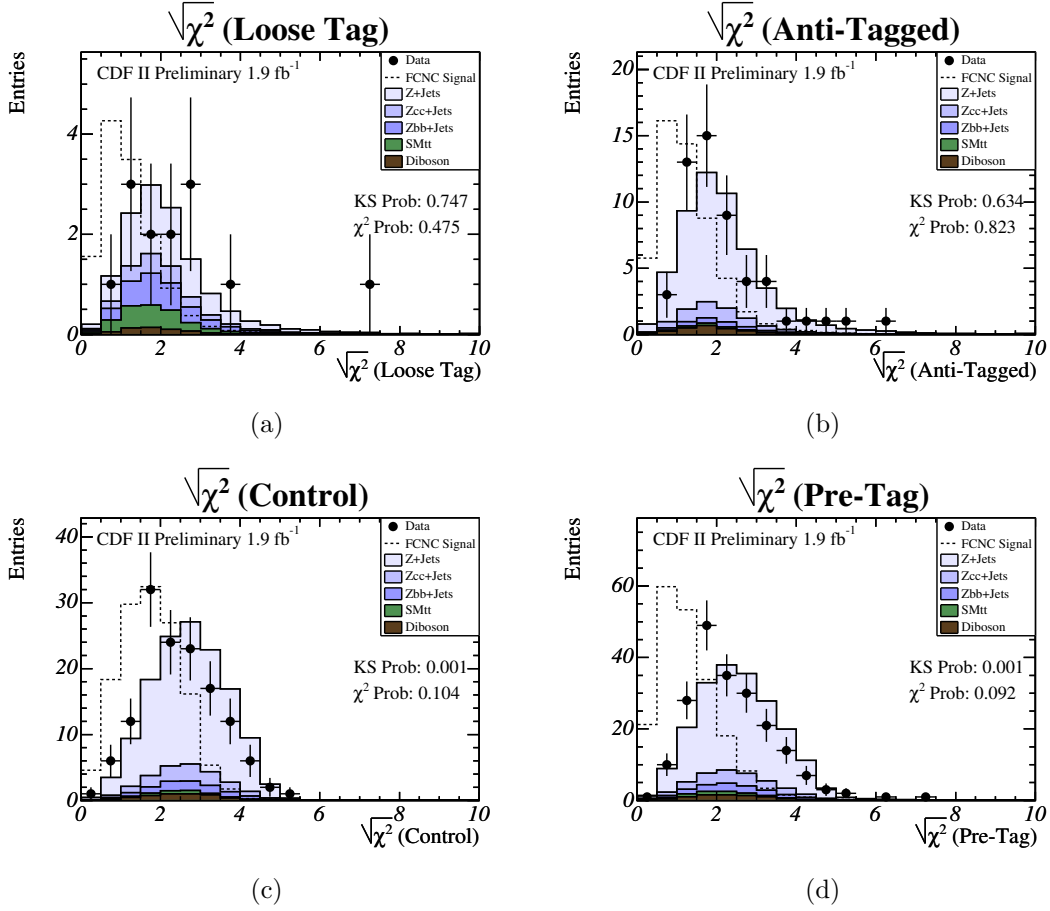


Figure A.22: The $\sqrt{\chi^2}$ distribution with shifted jet energy scale up 1σ for the (a) tagged, (b) anti-tagged, (c) control, and (d) pre-tagged selections. The expected backgrounds are normalized to the data event yield.

A.4.2 The Transverse Mass Distribution, JES shift $+1\sigma$

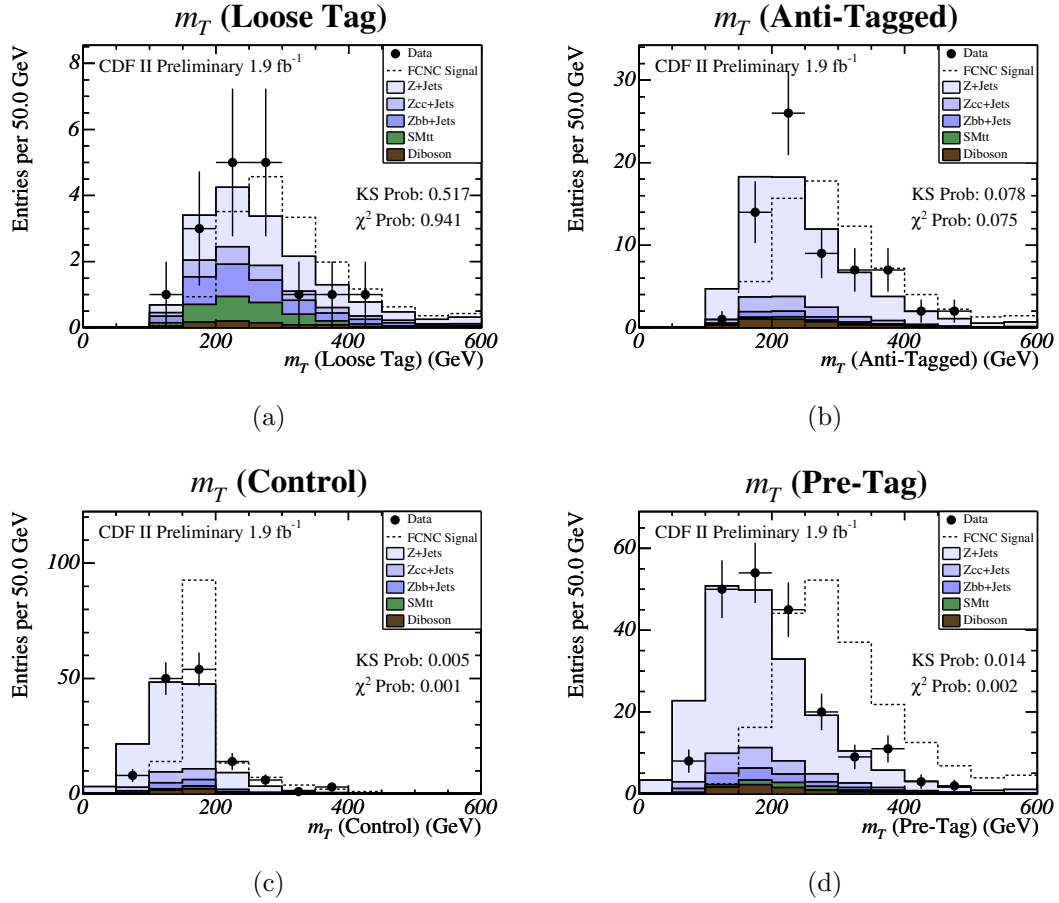


Figure A.23: The transverse mass distribution with shifted jet energy scale up 1σ for the (a) tagged, (b) anti-tagged, (c) control, and (d) pre-tagged selections. The expected backgrounds are normalized to the data event yield.

A.4.3 The Leading Jet E_T Distribution, JES shift $+1\sigma$

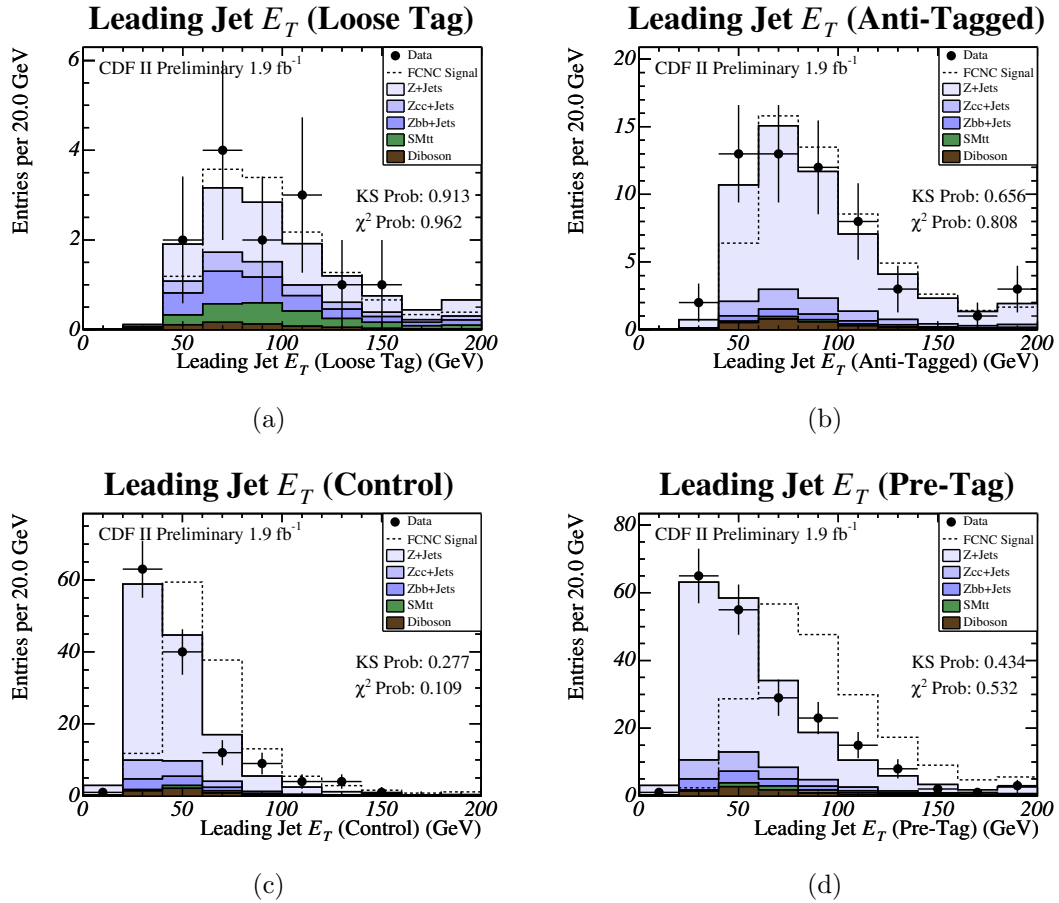


Figure A.24: The transverse energy distribution with shifted jet energy scale up 1σ of the leading jet for the (a) tagged, (b) anti-tagged, (c) control, and (d) pre-tagged selections. The expected backgrounds are normalized to the data event yield.

A.4.4 The Second Jet E_T Distribution, JES shift $+1\sigma$

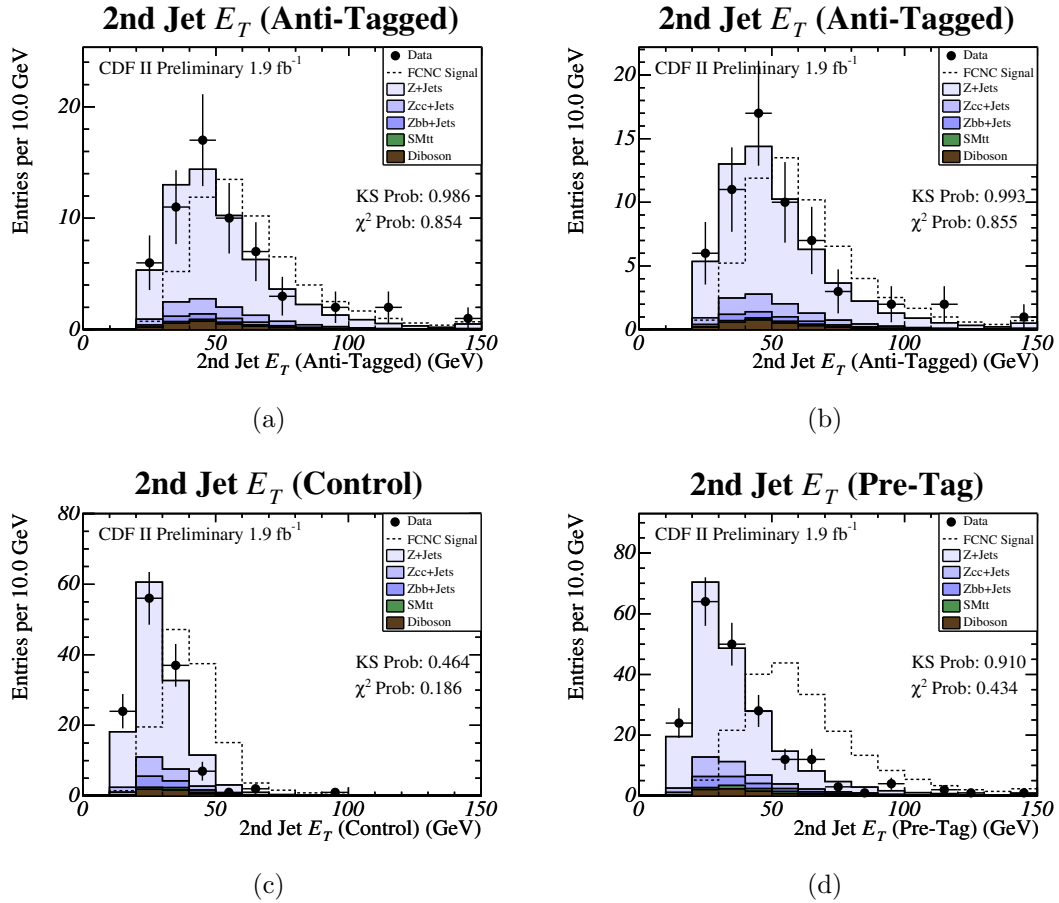


Figure A.25: The transverse energy distribution with shifted jet energy scale up 1σ of the second jet for the (a) tagged, (b) anti-tagged, (c) control, and (d) pre-tagged selections. The expected backgrounds are normalized to the data event yield.

A.4.5 The Third Jet E_T Distribution, JES shift $+1\sigma$

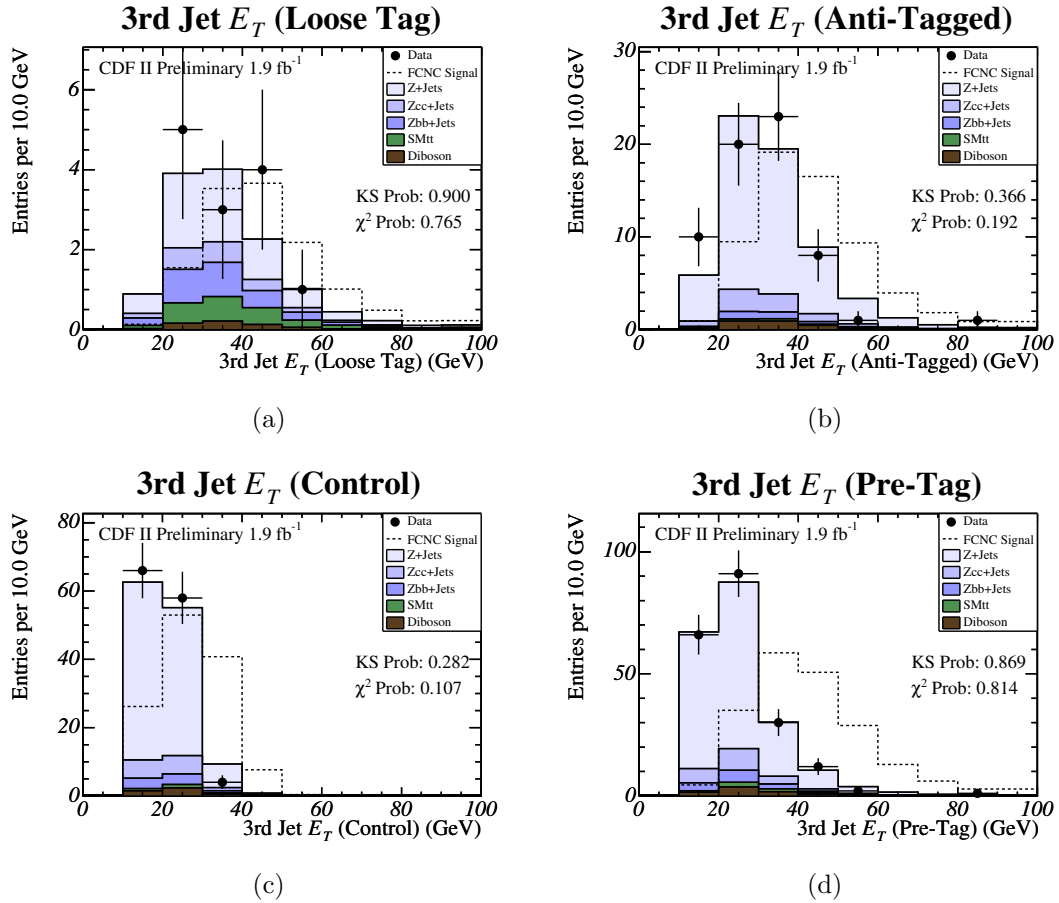


Figure A.26: The transverse energy distribution with shifted jet energy scale up 1σ of the third jet for the (a) tagged, (b) anti-tagged, (c) control, and (d) pre-tagged selections. The expected backgrounds are normalized to the data event yield.

A.4.6 The Fourth Jet E_T Distribution, JES shift $+1\sigma$

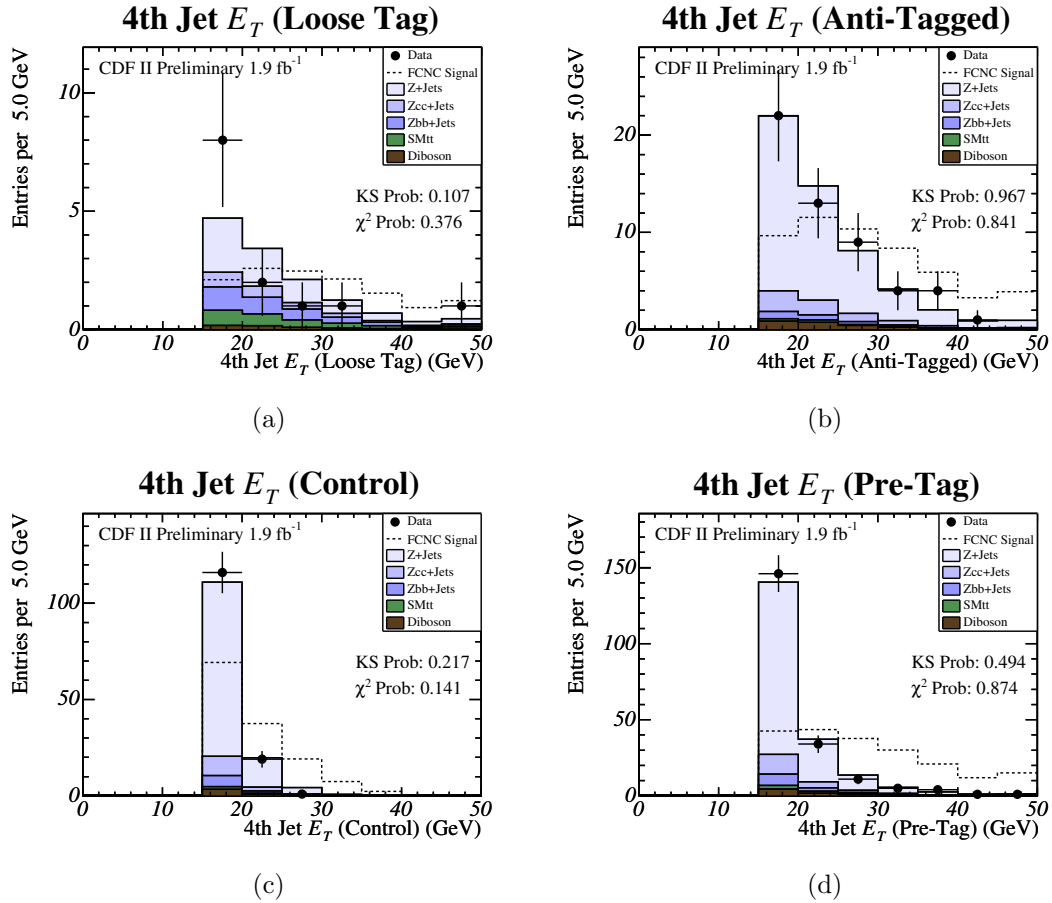


Figure A.27: The transverse energy distribution with shifted jet energy scale up 1σ of the fourth jet for the (a) tagged, (b) anti-tagged, (c) control, and (d) pre-tagged selections. The expected backgrounds are normalized to the data event yield.

A.4.7 The G_T Distribution, JES shift $+1\sigma$

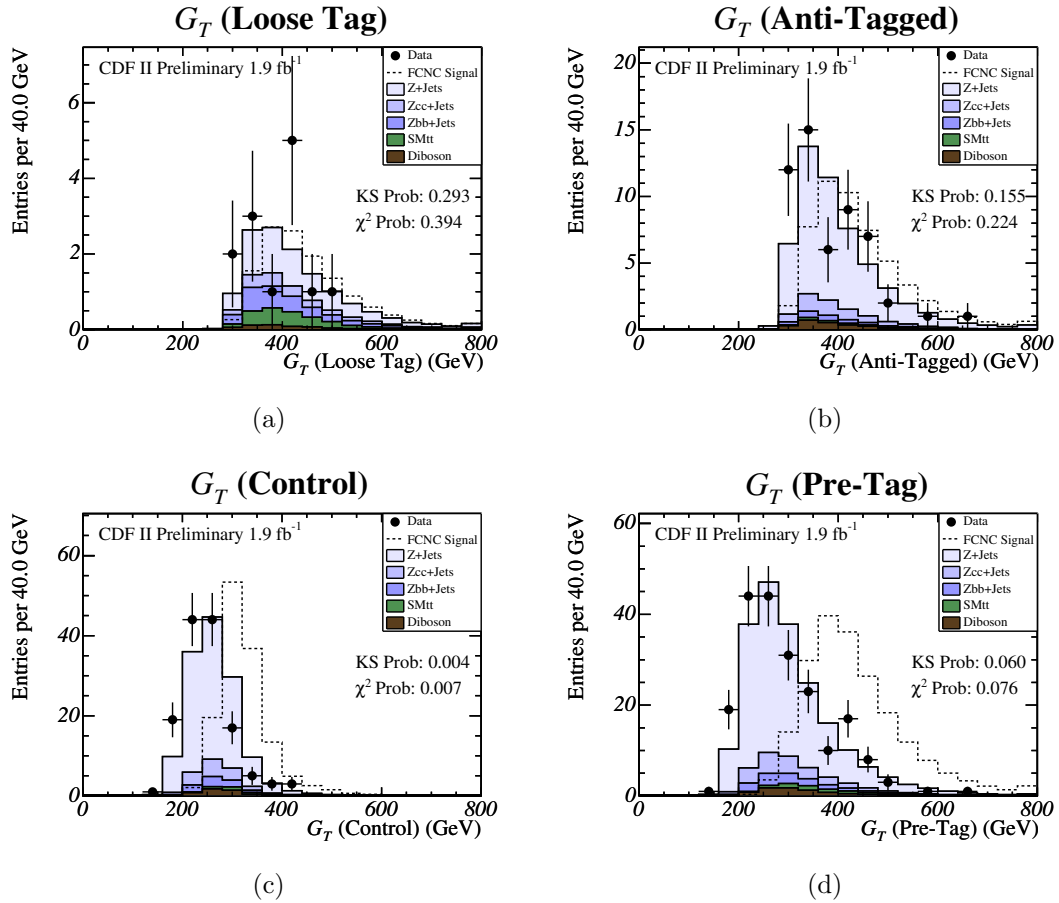


Figure A.28: The G_T distribution with shifted jet energy scale up 1σ for the (a) tagged, (b) anti-tagged, (c) control, and (d) pre-tagged selections. G_T is defined as the scalar sum of the lepton transverse momenta and the jet transverse energies. The expected backgrounds are normalized to the data event yield.

A.4.8 The Missing Transverse Energy Distribution, JES shift $+1\sigma$

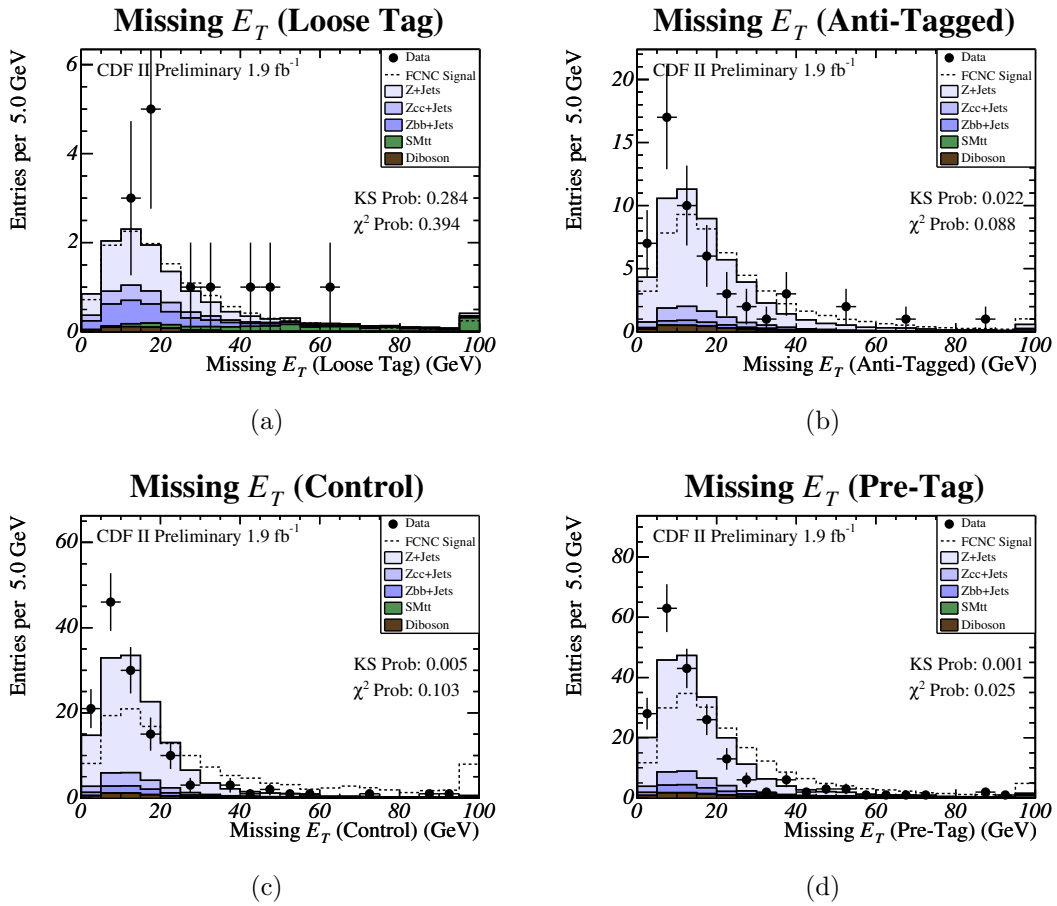


Figure A.29: The missing transverse energy distribution with shifted jet energy scale up 1σ for the (a) tagged, (b) anti-tagged, (c) control, and (d) pre-tagged selections. Missing transverse energy is not used as a cut in this analysis. The expected backgrounds are normalized to the data event yield.

A.4.9 The Z Mass Distribution, JES shift $+1\sigma$

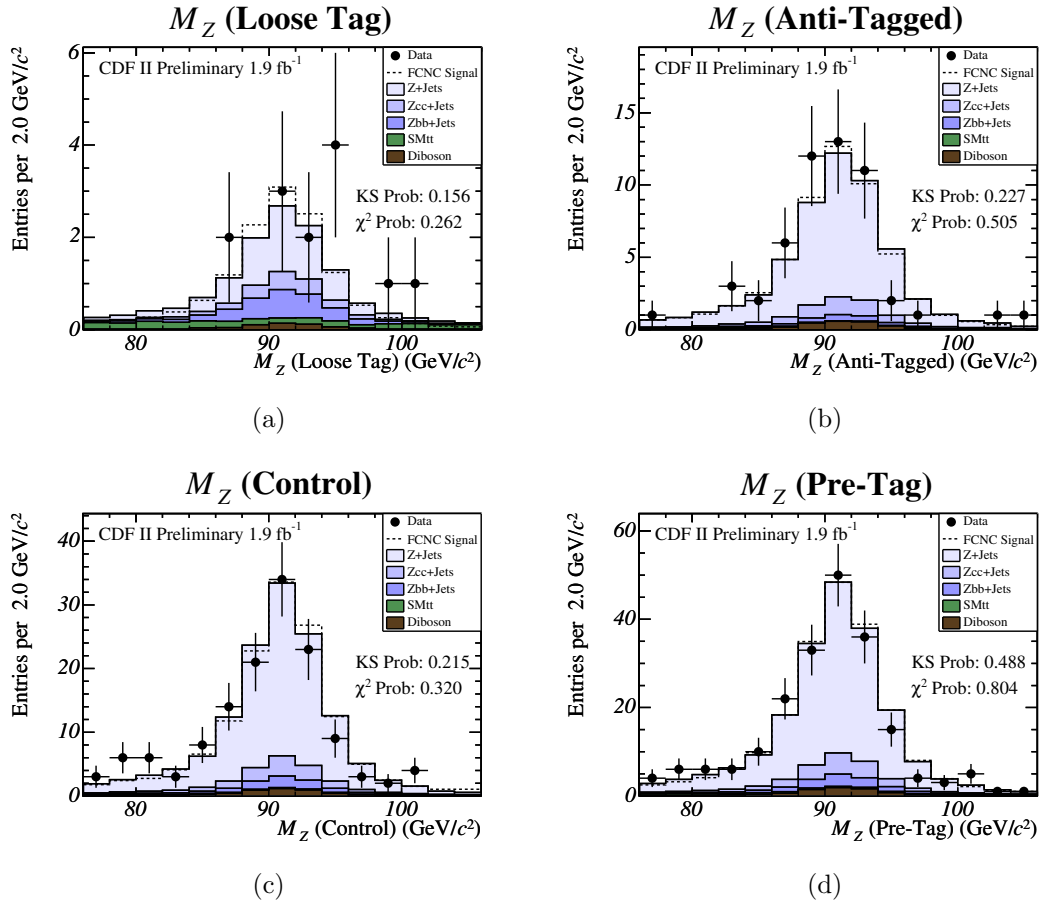


Figure A.30: The Z mass distribution with shifted jet energy scale up 1σ for the (a) tagged, (b) anti-tagged, (c) control and (d) pre-tagged selections. The expected backgrounds are normalized to the data event yield.

Appendix B

Effects of Luminosity Scaling

At the time of this thesis, no updated Monte Carlo samples were available to model the full 1.9 fb^{-1} dataset. Thus, the Monte Carlo samples were appropriately reweighted to account for the increased luminosity. To understand the implications of scaling up the Monte Carlo samples, as discussed in Section 5.2.1, the kinematic variables used in analysis were plotted and compared high versus low luminosities to ensure that there were no luminosity dependent effects. In addition, the Monte Carlo samples were examined at high and low numbers of overlaid interactions. This Appendix contains these studies.

B.1 Overlaid Interactions and Instantaneous Luminosity

The number of overlaid interactions, \mathcal{N}_{IA} is proportional to the instantaneous luminosity \mathcal{L} and the inelastic cross-section σ , and inversely proportional to the effective bunch crossing rate at the Tevatron, currently 1.715 MHz.

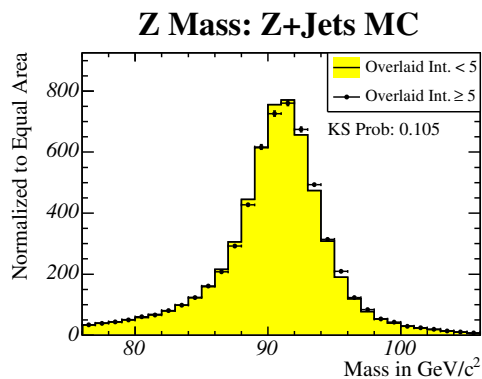
$$\mathcal{N}_{\text{IA}} = \frac{\mathcal{L} \cdot \sigma}{1.715 \text{ MHz}} \quad (\text{B.1})$$

The luminosity cut was chosen to be $150 \times 10^{30} \text{ cm}^{-2} \text{ s}^{-1}$, thus the corresponding division appropriate for the Monte Carlo is $\mathcal{N}_{\text{IA}} = 5.4$; the number of overlaid interactions used in this study is 5.

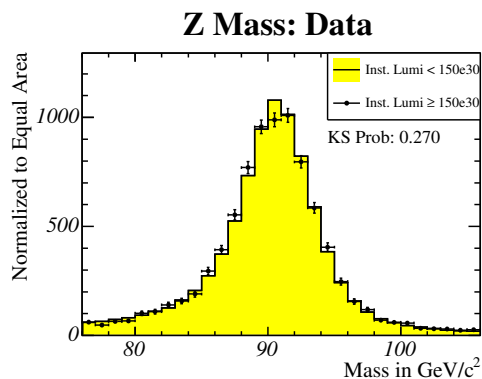
In the case of comparing the E_T of the leading and second more energetic jets in the event, events overlaid interactions fewer than 2 in Monte Carlo and events with instantaneous luminosity less than $50 \times 10^{30} \text{ cm}^{-2} \text{ s}^{-1}$ in data are omitted because of poor statistics.

B.2 Luminosity Study: Kinematic Variables

B.2.1 Z Mass



(a)



(b)

Figure B.1: (a) Comparisons for the Z invariant mass distribution in Monte Carlo simulation, showing events with fewer than 5 (histogram) and more than 5 (data points) overlaid interactions. No deviation in shape is seen. (b) Comparisons for the Z invariant mass distribution in 1.9 fb^{-1} of data, showing events with an instantaneous luminosity of less than $150 \times 10^{30} \text{ cm}^{-2} \text{ s}^{-1}$ (histogram) and more than $150 \times 10^{30} \text{ cm}^{-2} \text{ s}^{-1}$ (data points). No deviation in shape is seen.

B.2.2 The Z s Leptons

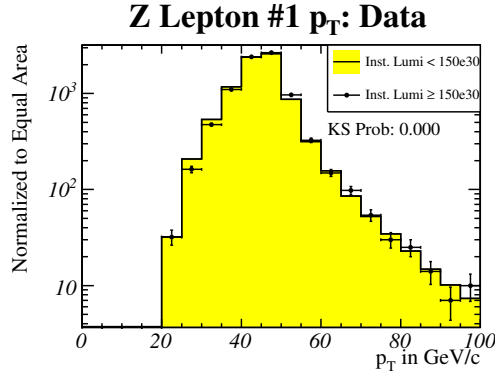
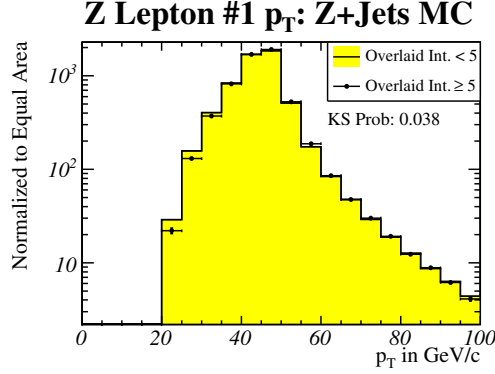


Figure B.2: (a) Comparisons for the p_T distribution for the lepton of the Z boson with the higher p_T in Monte Carlo simulation, showing events with fewer than 5 (histogram) and more than 5 (data points) overlaid interactions. No deviation in shape is seen. (b) Comparisons for the p_T distribution for the lepton of the Z boson with the higher p_T in 1.9 fb^{-1} of data, showing events with an instantaneous luminosity of less than $150 \times 10^{30} \text{ cm}^{-2} \text{ s}^{-1}$ (histogram) and more than $150 \times 10^{30} \text{ cm}^{-2} \text{ s}^{-1}$ (data points). No deviation in shape is seen.

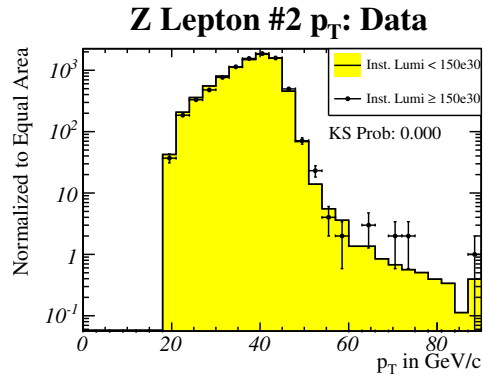
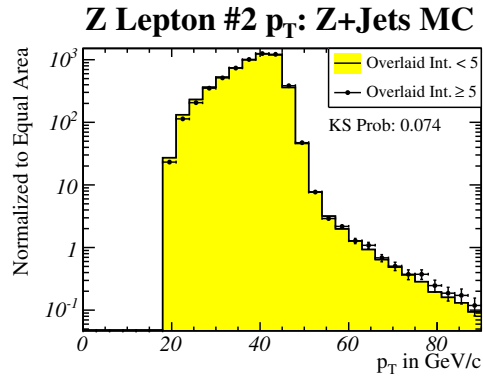


Figure B.3: (a) Comparisons for the p_T distribution for the lepton of the Z boson with the lesser p_T in Monte Carlo simulation, showing events with fewer than 5 (histogram) and more than 5 (data points) overlaid interactions. No deviation in shape is seen. (b) Comparisons for the p_T distribution for the lepton of the Z boson with the lesser p_T in 1.9 fb^{-1} of data, showing events with an instantaneous luminosity of less than $150 \times 10^{30} \text{ cm}^{-2} \text{ s}^{-1}$ (histogram) and more than $150 \times 10^{30} \text{ cm}^{-2} \text{ s}^{-1}$ (data points). No deviation in shape is seen.

B.2.3 The Leading Jet E_T

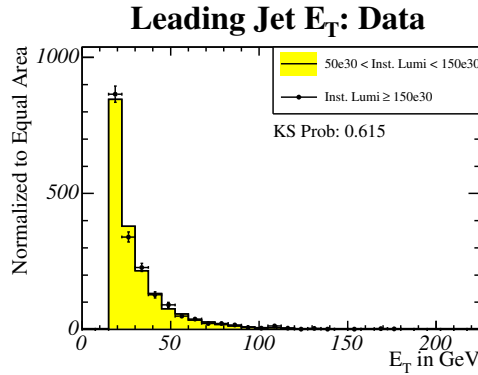
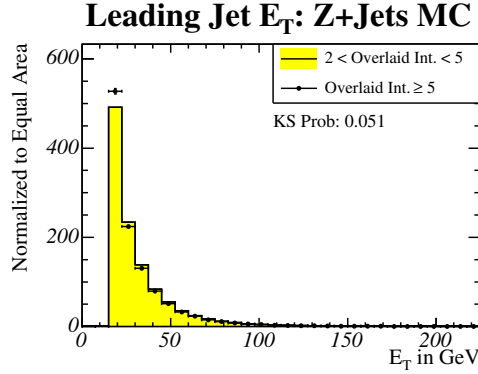


Figure B.4: (a) Comparisons for the E_T distribution of the leading jet in the event in Monte Carlo simulation, showing events with more than 2 but fewer than 5 (histogram) and more than 5 (data points) overlaid interactions. No deviation in shape is seen. (b) Comparisons for the E_T distribution of the leading jet in the event in 1.9 fb^{-1} of data, showing events with an instantaneous luminosity of more than $50 \times 10^{30} \text{ cm}^{-2} \text{ s}^{-1}$ but less than $150 \times 10^{30} \text{ cm}^{-2} \text{ s}^{-1}$ (histogram) and more than $150 \times 10^{30} \text{ cm}^{-2} \text{ s}^{-1}$ (data points). No deviation in shape is seen.

B.2.4 The Second Jet E_T

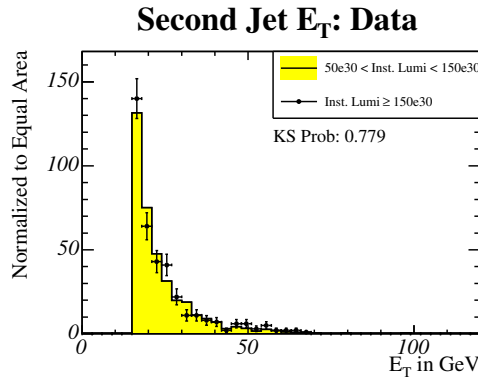
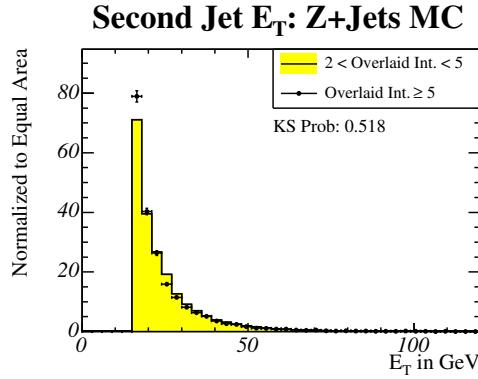


Figure B.5: (a) Comparisons for the E_T distribution of the second jet in the event in Monte Carlo simulation, showing events with more than 2 but fewer than 5 (histogram) and more than 5 (data points) overlaid interactions. No deviation in shape is seen. (b) Comparisons for the E_T distribution of the second jet in the event in 1.9 fb^{-1} of data, showing events with an instantaneous luminosity of more than $50 \times 10^{30} \text{ cm}^{-2} \text{ s}^{-1}$ but less than $150 \times 10^{30} \text{ cm}^{-2} \text{ s}^{-1}$ (histogram) and more than $150 \times 10^{30} \text{ cm}^{-2} \text{ s}^{-1}$ (data points). No deviation in shape is seen.

B.2.5 Transverse Mass, m_T

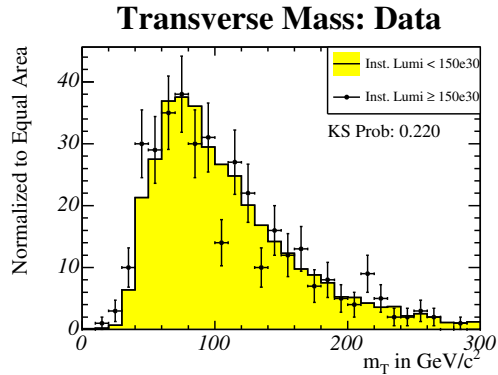
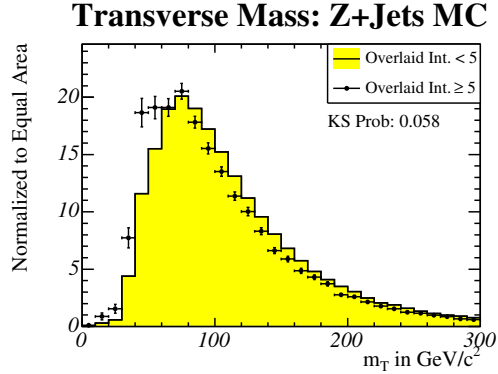


Figure B.6: Events in both the Monte Carlo and data plots are required to have at least one jet of $E_T > 15\text{GeV}$. (a) Comparisons for the transverse mass distribution, m_T , in Monte Carlo simulation, showing events with fewer than 5 (histogram) and more than 5 (data points) overlaid interactions. No deviation in shape is seen. (b) Comparisons for the transverse mass distribution, m_T , in 1.9fb^{-1} of data, showing events with an instantaneous luminosity of less than $150 \times 10^{30} \text{ cm}^{-2} \text{ s}^{-1}$ (histogram) and more than $150 \times 10^{30} \text{ cm}^{-2} \text{ s}^{-1}$ (data points). No deviation in shape is seen.

B.2.6 Scalar Energy Sum, G_T

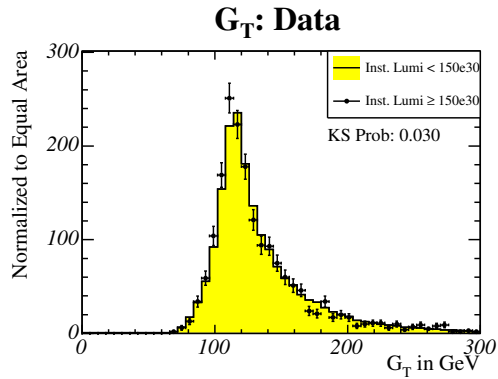
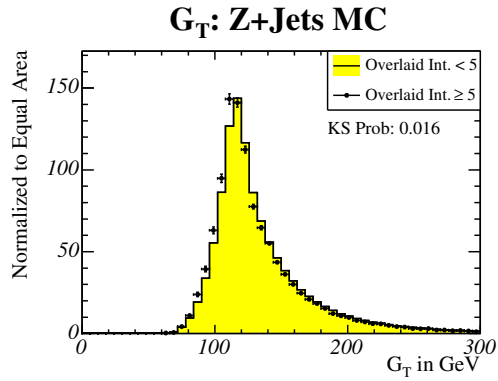


Figure B.7: G_T is defined as the scalar sum of the energies in the event, minus the missing E_T . (a) Comparisons for G_T in Monte Carlo simulation, showing events with fewer than 5 (histogram) and more than 5 (data points) overlaid interactions. No deviation in shape is seen. (b) Comparisons for G_T in 1.9 fb^{-1} of data, showing events with an instantaneous luminosity of less than $150 \times 10^{30} \text{ cm}^{-2} \text{ s}^{-1}$ (histogram) and more than $150 \times 10^{30} \text{ cm}^{-2} \text{ s}^{-1}$ (data points). No deviation in shape is seen.